This is to certify that the
dissertation entitled

Self-Assembly and Physical Properties of Atomic Aggregates

presented by

Savas Berber

has been accepted towards fulfillment
of the requirements for the

Ph.D. degree in Physics

David Tománek

Major Professor's Signature

May 3, 2004

Date

SELF-ASSEMBLY AND PHYSICAL PROPERTIES OF ATOMIC AGGREGATES

By

Savas Berber

A DISSERTATION

Submitted to
Michigan State University
in partial fulfillment of the requirements
for the degree of

DOCTOR OF PHILOSOPHY

Department of Physics and Astronomy

2004

ABSTRACT

SELF-ASSEMBLY AND PHYSICAL PROPERTIES OF ATOMIC AGGREGATES

By

Savas Berber

In this Thesis, I present a study of nanoscaled atomic aggregates such as fullerenes, nanotubes, diamondoids, and related materials. Nanotubes and fullerenes, which could be formed of any layered material, show unusual physical properties due to their lower dimensionality and nanometer size. I have investigated the microscopic self-assembly mechanisms and the physical properties of these nanoscale atomic aggregates through computer simulations primarily by using molecular dynamics simulations combined with structure optimization and total energy calculations.

First, I determined the stability, optimum geometry and electronic properties of nanometer-sized capped graphitic cones, called "nanohorns". My main result, simulated scanning tunneling microscopy images of the various structures at different bias voltages, indicate a net electron transfer towards the pentagon vertex sites.

Next, I investigated the absorption of fullerenes in a nanotube during a hierarchical self-assembly of "nanopeapods". I found the absorption through a defect to be significantly more efficient than the end-on absorption. I also investigated the energetics and detailed fusion mechanism of fullerenes inside a carbon nanotube. I found that fullerenes are pulled in by a "capillary" force, which yields an effective GPa pressure. Fusion of fullerenes continues along the minimum energy path as a sequence of Stone-Wales transformations.

I have further investigated the microscopic dislocation mechanism leading to structural transformations in nanostructures. In particular, I studied the relative stability and the conversion mechanism between multi-wall carbon nanotubes and graphitic scrolls. I postulated a zipper-like mechanism, which converts a scroll to the more sta-

ble multiwall nanotube. I also found this transformation to proceed very efficiently due to the unusually low associated activation barrier. A further study related to defects in nanoscale systems involves the response of defective nanotubes to thermal and electronic excitations, which are described using *ab initio* molecular dynamics calculations, based on the time-dependent density functional formalism. I found that defective nanotubes, exposed to electronic or thermal excitations, show an unexpected self-healing ability, which is intimately linked to their nanometer size.

I also explored the suitability of nanotube-based hooks for bonding in nanoscale electro-mechanical systems (NEMS). Arrays of nanohooks, which are permanently anchored in solid surfaces, are the nanoscale counterpart of velcro fasteners, forming tough bonds with a capability of self-repair. I also investigated the possibility of novel possible "super-hard" crystalline phases of covalently bonded C_{60} fullerenes and determined their structural, elastic, and electronic properties.

My studies further involved exploring the physical origin of the unexpected thermal contraction of carbon fullerenes and nanotubes. At low temperatures, these systems gain structural and vibrational entropy by exploring the configuration space at little energy cost, which translates into thermal contraction of these systems at moderate temperatures. I also predicted the thermal conductivity of carbon nanotubes. My results suggest an unusually high value $\lambda \approx 6,600$ W/m·K for an isolated $(10, 10)$ nanotube at room temperature, which exceeds the thermal conductivity of the best thermal conductor known, isotopically pure diamond.

Finally, I contributed to a study of magnetism in all-carbon nanostructures using *ab initio* spin density functional theory. The main conclusion of that study was that in this and other non-alternant aromatic systems with negative Gaussian curvature, unpaired spins can be introduced by sterically protected carbon radicals, so that particular systems, related to schwarzite, carry a net magnetic moment.

To my Family, Selda, Saadettin and Yunus.

ACKNOWLEDGMENTS

First of all, I thank my Thesis advisor, Professor David Tománek. I have enjoyed being in a moderate size research group, and being in close contact with my Thesis advisor Professor Tománek. Whenever I read an article about how a good Thesis advisor should be, I realize that he has done even more than what an excellent mentor does. He has always encouraged me to present my results by writing papers and giving talks in conferences. He almost had to carry me on his shoulder to Atlanta, my first March meeting. He introduced me to almost all the best people in my field in person. He did everything he could, to support my Ph. D. studies in all aspects. We had very stimulating discussions on physics, science, technology, science policies, cultures, religion. He has helped me to get experience on every stage of the academic life. I always believed he deserves better graduate students than I am. I would not be in this position without his continuous support and guidance.

I am grateful to the members of my Guidance Committee: Professors Jack Bass, S.D. Mahanti, Vladimir Zelevinsky, and Richard Enbody. I greatly appreciated their comments and suggestions.

I was privileged to collaborate with Young-Kyun Kwon, Mina Yoon, Dr. Yoshiyuki Miyamoto, Dr. Noejung Park, Seunghwu Han, Prof. Eiji Osawa, Prof. Angel Rubio Secades. Young-Kyun Kwon and Mina Yoon have a special place; I have always enjoyed group meetings and scientific discussions with them. I also would like to mention the hospitality of Seoul National University graduate students who made my visit to Korea an enjoyable and fruitful time. Thank you all!

During my Thesis work, I had the opportunity to discuss scientific issues with the experts in the field. I thank Sumio Iijima for fruitful discussions on carbon nanohorns and the synthesis of nanohook structures. I appreciated useful discussions with Ray Baughman, who drew our attention to thermal expansion properties of carbon nanos-

tructures, and with Alex Soldatov on the experimental aspects of thermal contraction. I acknowledge useful discussions with Professors Pao-Kuang Kuo and Ctirad Uher on thermal conductivity of carbon materials. I also feel lucky to happen to know the experimental work of Andrei Rode on magnetic carbon nanostructured materials before published. I thank David Luzzi for fruitful discussions on nanopeapods.

I also thank my friends who reminded me that I am supposed graduate some day by asking me every Friday when I will graduate. They helped me to realize the real reason why I was at MSU.

I acknowledge financial support from the National Education Ministry of Turkey, Korean Molecular Logic Devices program, Rosseter Holding Ltd. , Engelhard Corporation, and MSU Graduate School through Dissertation Completion Fellowship. I appreciated the efforts of Prof. David Tománek, Prof. S. D. Mahanti, and Ms. Debbie Simmons during the application for Dissertation Completion Fellowship.

I must also thank my wife Selda for putting up with my late hours, my spoiled weekends, my bad temper, but above all for putting up with me.

Table of Contents

List of Tables

List of Figures

Chapter 1

Introduction

Science and technology has seen tremendous development in the last century. Our understanding of the nature and the phenomena happening around us improved by a great amount. Scientists and engineers now not only understand the nature better, but have also developed new techniques allowing us to explore unknown phenomena in relatively little time. Most people agree that we would not be in this position in science without atomic scale probes, electron microscopes, and powerful computers to process all the data we collect. The increasing demand of humanity for faster, better, more reliable, and portable devices and products has pushed the limits of engineering to sub-micron scales. Micro-scale electromagnetic and mechanical devices have become the study subjects of mechanical engineers. We face further challenges when we go to still smaller scales in the emerging field of nanotechnology. The fuel of scientific development during the last part of the 20th century, including significant advances in the electronic and computer industry, now faces great challenges. The demand for higher speed forces us to use smaller building blocks in devices. Within the next decade, we expect that the electronic industry will reach the quantum limit for silicon-based device applications, where we can no longer control structural and functional aspects of future nanoscale devices.

Apart from dealing with small systems, it is a great challenge to manufacture these devices using conventional methods, such as lithography. One has to employ self-assembly or directed self-assembly methods to form nanometer-sized building blocks of future engineering marvels. Nevertheless, we do not have sufficient knowledge of the phenomena occurring at the nanoscale. Nanostructures constantly surprise with unexpected properties. Our basic science interest quickly shifts from understanding those structures to using them in our everyday applications.

In spite of advances in atomic scale probes, there are still many phenomena which could not be completely understood by using only only experimental techniques. In particular, it is very hard to interpret experimental results without theoretical or modeling studies. Computer modeling has proven to be very useful in describing and understanding phenomena occurring at the nanoscale. Computers also help us to design new materials, and to predict their physical properties. Recent developments in computer modeling, and advances in computer technology have made it possible to attack some of the most important problems we are facing in developing and understanding nanostructures. Not only physical sciences, but also biological sciences tend to follow the same direction in recent years. The solution of medical problems is now being searched at the DNA level, on the nanometer scale.

Some of the most promising building blocks of nanotechnology are based on carbon. Elemental carbon exhibits a wide range of properties, which reflects the different types of bonding between carbon atoms. Research in all-carbon nanostructures was initiated by the discovery of C_{60} molecule, which reminded the carbon community of apparently endless possibilities involving carbon nanostructures. Carbon-based nanotechnology was subsequently accelerated by the discovery of nanotubes. Nanotubes and fullerenes have proven to be promising candidates for future applications. Current commercial applications include battery applications, and improvements of mechanical properties in composites.

Nanotube-based transistors are believed to be superior to state of the art silicon transistors. Moreover, carbon nanotube transistors are easy to manufacture, and could be cheaper to produce in the future. Their superior mechanical properties, thanks to their strong graphitic bonds, make them viable materials for polymer reinforcement and nanomanipulation applications. Chemical functionalization makes nanotubes useful in sensor applications. Moreover, nanotubes appear to be ideal 1-dimensional model systems to study phenomena, such as quantum transport, Luttinger liquid behavior, and Coulomb blockade.

In the meantime, some related materials, such as nanohorns, and some hybrid structures, such as nanopeapods, have been synthesized.

The fact that these complex structures go beyond the Theorists' wildest dreams encouraged the scientific community to suggest new artificial materials and geometries based on sp^2 bonded carbon, which could be modeled on a computer. In my PhD Thesis work, I tried to perform calculations using a variety of techniques to further enhance general understanding of nanoscale phenomena. I was bold enough to predict selected physical properties of nanotubes and related nano-materials prior to experimental observation, including thermal conductivity and thermal contraction. My studies involved what I considered to be interesting systems or interesting properties. Scientists initially interested in purely electronic applications of nanotubes and related materials quickly realized that knowing only electronic properties was not enough to construct nanotube-based devices. I tried to fill the gap of knowledge regarding also non-electronic properties of nanotubes and nanostructured carbon materials. In particular, I focused on electronic, thermal, mechanical, and magnetic properties of carbon nanostructures.

Following the discovery of nanotubes, the general perception was that these nanostructures are atomically perfect. Only later on, scientists realized that defects were present in these structures which could never be absolutely eliminated. Since

there is no simple experimental way of determining the position and morphology of defects, it is very difficult to estimate how these defects may affect the physical properties of nanostructures. Computer modeling may be the most efficient way to determine the effect of defects in nanostructures. Since few atomic vacancies per nanostructure translate into effective defect densities that are currently considered unacceptable, industry leaders, such as IBM and NEC, were initially reluctant to invest in nanotube research before knowing how defective nanotubes would perform in devices. Since processes associated with device failure are very fast and irreproducible in most occurrences, little information could be extracted from experimental data. The most reliable way to determine the microscopic pathway of a failure thus involves computer simulations under extreme conditions. My simulations have suggested that presence of defects lowers the activation barriers for structural changes during a directed self-assembly of systems. Even more surprising was my finding that nanostructures heal themselves.

Recently, diamondoids joined the group of candidates for future nanoscale building blocks. Successful separation of diamondoid isomers from crude oil opened an opportunity to use these molecules in nanotechnology. We now expect a possible synthesis of complex nanostructures based on nanotubes and diamondoids instead of fullerenes, with potentially interesting applications.

The phenomena we encounter in nanotubes and related materials should not be limited to graphite-based systems only. Any layered material, including BN, WS_2, and others, should form similar nanostructures, which may exhibit similar phenomena. Even though carbon nanostructures should maintain a special place, I believe other materials may find even more important applications in the future.

Since this PhD Thesis covers not only different length scales, but also a wide range of phenomena, I had to use different techniques , which were specific to each study. I will not discuss the details of computational techniques, including molecular dynamics

simulations, as far as they have been covered in the literature. Each Chapter should be considered essentially self-contained, including an introduction, a brief description of methods, summary and conclusions.

In the following, I will briefly summarize the notation which is commonly used by scientists studying nanotubes and diamondoids. After this brief summary, I will outline the structure of my Thesis.

1.1 Nomenclature of carbon nanostructures

Most stable allotropes of carbon are sp^2 bonded graphite and sp^3 bonded diamond. These two bonding schemes are found also in carbon nanostructures. One of the most promising building blocks of future nanoscale devices are sp^2 bonded fullerenes and nanotubes. Another important building blocks of carbon nanostructures are diamondoids, which shows sp^3 bonding. In the following I will introduce common notation for carbon nanotubes, and the physical structure of diamondoids.

Carbon nanotubes are classified primarily into achiral and chiral nanotubes [1, 2]. An achiral nanotube exhibits a mirror symmetry with respect to a plane normal to the tube axis. Chiral nanotubes miss this symmetry, and exhibit a spiral symmetry instead. There are only two types of achiral nanotubes, namely "armchair" and "zigzag" nanotubes, discussed below. The structure of a nanotube is specified by the orientation of the hexagonal carbon rings on the graphene sheet wrapped to a tube with respect to the tube axis. This orientation is characterized by the chiral index (n, m) of the nanotube defined by the chiral vector $\mathbf{C}_h$

$$\mathbf{C}_h = n\mathbf{a}_1 + m\mathbf{a}_2, \tag{1.1}$$

where $\mathbf{a}_i (i = 1, 2)$ are real space unit vectors of the hexagonal lattice. This chiral vector, as shown in Figure 1.1, connects two equivalent sites O and A on a graphene

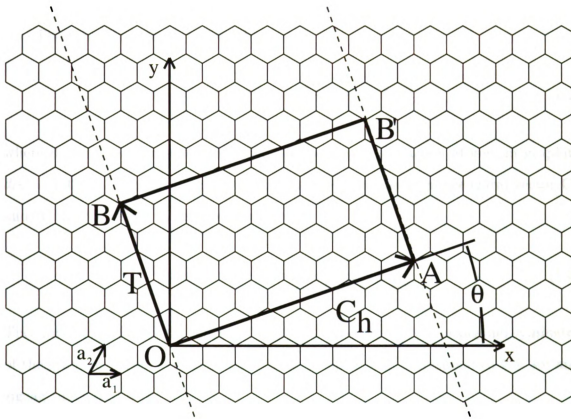

Figure 1.1: A nanotube can be constructed by connecting site O to site A and site B to site B'. This nanotube is $(6, 3)$ (see the text for the tube classification). The chiral vector $\mathbf{C}_h$ and the translational vector $\mathbf{T}$ of the nanotube are represented by arrow lines of OA and OB, respectively. The rectangle $OAB'B$ defines the unit cell of the nanotube.

sheet. Its magnitude C_h represents the circumferential length of the nanotube being characterized by $\mathbf{C}_h$. The direction perpendicular to $\mathbf{C}_h$ becomes the tube axis. Pairs of integers (n, m) in Eq. (1.1), specifying all possible chiral vectors, defines all different ways of rolling the graphene sheet to form a nanotube. Zigzag nanotubes, which have a zigzag shape of the cross-sectional ring are denoted by $(n, 0)$. Armchair nanotubes, which have an armchair shape of the cross-sectional ring, are denoted by (n, n).

The tube diameter d_t is given by

$$d_t = C_h/\pi = \sqrt{3} d_{CC}(n^2 + nm + m^2)^{1/2}/\pi, \tag{1.2}$$

where d_{CC} is the nearest-neighbor distance between two carbon atoms (in graphite $d_{CC} = 1.42$ Å). The chiral angle θ, defined as the angle between the chiral vector $\mathbf{C}_h$ and the lattice vector $\mathbf{a}_1$, is given by

$$\cos\theta = \frac{\mathbf{C}_h \cdot \mathbf{a}_1}{C_h a} = \frac{2n + m}{2\sqrt{n^2 + nm + m^2}}. \tag{1.3}$$

The chiral angle θ is in the range of $0 \leq |\theta| \leq 30°$ because of the hexagonal symmetry of the graphene sheet. Armchair nanotubes, in particular, correspond to $\theta = 30°$ and zigzag tubes to $\theta = 0°$.

The vector $\mathbf{T}$, called the translation vector, is parallel to the tube axis, i.e. perpendicular to the chiral vector $\mathbf{C}_h$. Using the relation of $\mathbf{C}_h \cdot \mathbf{T}$, the vector $\mathbf{T}$, which becomes the lattice vector of the 1D tube unit cell, can be expressed in terms of the basis vectors $\mathbf{a}_i$ as

$$\mathbf{T} = \frac{1}{d_R}[-(n + 2m)\mathbf{a}_1 + (2n + m)\mathbf{a}_2], \tag{1.4}$$

where d_R is the greatest common divisor of $(n + 2m)$ and $(2n + m)$. Furthermore, d_R can be expressed in term of the greatest common divisor d of n and m. If $(n - m)$

is a multiple of 3 so that $(n - m) = 3d$, then $d_R = 3d$, and otherwise $d_R = d$. Note that the bigger d_R, the smaller is the length of $\mathbf{T}$. For example, $\mathbf{T} = -\mathbf{a}_1 + \mathbf{a}_2$ for any (n, n) armchair nanotube ($d_R = 3d = 3n$) and $\mathbf{T} = -\mathbf{a}_1 + 2\mathbf{a}_2$ for any $(n, 0)$ zigzag nanotubes ($d_R = n$). A $(6, 3)$ nanotube ($d = d_R = 3$), shown in Figure 1.1, has $T = -4\ a_1 + 5\ a_2$.

Unlike nanotubes, diamondoids show sp^3 bonding between carbon atoms, and could be described as hydrogen terminated nanoscale diamond fragments. These nanoscale building blocks are very different from fullerenes and nanotubes, but compare well in stability and light weight with fullerenes and nanotubes. Being essentially hydrogen-terminated nanometer sized diamond fragments, they may occur in a large variety of shapes, as shown in Fig. 1.2. The smallest possible diamondoid is adamantane[3], consisting of ten carbon atoms arranged as a single diamond cage[4], surrounded by sixteen hydrogen atoms, as shown in Fig. 1.2(a). Larger diamondoids[5, 6, 7] are created by connecting more diamond cages and are categorized according to the number of diamond cages they contain. The diamondoids shown in Fig. 1.2 contain up to tens of carbon atoms and are only a few nanometers in diameter.

1.2 Outline of the dissertation

This dissertation contains 11 Chapters, including the introduction chapter. The computational method of choice throughout the dissertation involves molecular dynamics simulations employing an electronic Hamiltonian based on the linear combination of atomic orbitals (LCAO). Where appropriate, this electronic Hamiltonian was substituted by the computationally less demanding Tersoff bond-order potential. For electronic structure calculations I either used *ab initio* techniques or a parametrized LCAO formalism. Magnetic properties were investigated using spin resolved density

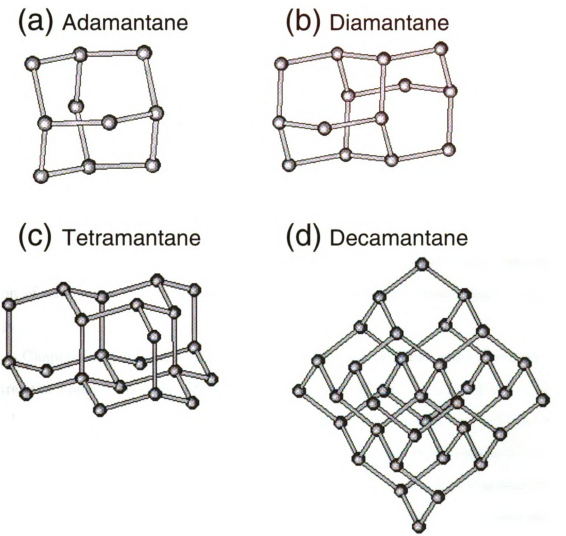

Figure 1.2: Relaxed structures of lower diamondoids. Hydrogen atoms, terminating the carbon skeleton, are omitted from the diagrams for clarity. (a) The smallest diamondoid, adamantane, consisting of a single diamond cage. (b) Diamantane with two diamond cages. (c) Tetramantane with four diamond cages. (d) Decamantane with ten diamond cages.

functional theory, and time dependent phenomena were explored by time-dependent density functional theory. The recursion technique for calculating energies and forces in molecular dynamics simulations has been described previously [8, 9].

The dissertation starts in Chapter 2. There, I use parameterized linear combination of atomic orbitals calculations to determine the stability, optimum geometry and electronic properties of nanometer-sized capped graphitic cones, called "nanohorns". Different nanohorn morphologies are considered, which differ in the relative location of the five terminating pentagons. Simulated scanning tunneling microscopy images of the various structures at different bias voltages reflect a net electron transfer towards the pentagon vertex sites. I find that the density of states at the tip, observable by scanning tunneling spectroscopy, can be used to discriminate between different tip structures. My molecular dynamics simulations indicate that disintegration of nanohorns at high temperatures starts in the highest-strain region near the tip.

Chapters 3 and 4 deals with a completely different, although related, nanostructure, the nanopeapod, consisting of fullerenes encapsulated in a nanotube. Using molecular dynamics calculations, I investigate the absorption of a C_{60} molecule in a $(10, 10)$ nanotube either through the open end or a large defect in the tube wall as possible scenarios for the hierarchical self-assembly of $(C_{60})_n@(10, 10)$ "nanopeapods". In view of the complex potential energy surface of this system, the encapsulation probability depends in a non-trivial manner on the local topology, as well as the launch angle and velocity of the fullerene. I find the absorption through a defect to be significantly more efficient than the end-on absorption. This process occurs most likely within a narrow launch velocity range for the fullerene, which agrees well with the observed optimum temperature window for peapod formation.

After shedding light on the microscopic formation mechanism of nanopeapods in Chapter 3, I investigate the equilibrium packing and detailed fusion mechanism

of fullerenes inside a carbon nanotube using total energy calculations in Chapter 4. Fullerenes are pulled in by a "capillary" force, which yields an effective GPa pressure and improves packing. The $(2 + 2)$ cycloaddition reaction, a necessary precursor for fusion, may be accelerated inside the nanotube template. Fusion continues along the minimum energy path as a sequence of Stone-Wales transformations. Based on my total energy calculations, I found that diamondoids should encapsulate in nanotubes through self-assembly, and later fuse into one dimensional diamond nanowires.

In Chapters 5 and 6, I switch gears, and deal with the adversity and advantages of defects in nanotubes. Chapter 5 describes a unique transformation mechanism, reminiscent of a zipper, which converts scrolls into nanotubes. Using total energy and structure optimization calculations, I investigate the relative stability and the conversion mechanism between multi-wall carbon nanotubes and graphitic scrolls. I suggest that axial segments of a nanotube and a scroll may coexist within the same tubular nanostructure, separated by a dislocation region. A scroll may convert to the more stable nanotube by concerted bond-rearrangement rather than bond breaking. I postulate the zipper-like conversion to proceed very efficiently due to the unusually low associated activation barrier.

Chapter 6 covers my computer simulations to study the defect tolerance of carbon nanotubes under extreme conditions. The response of the system to electronic excitations is investigated using *ab initio* molecular dynamics calculations, based on the time-dependent density functional. Nosé-Hoover molecular dynamics simulations are used to gain insight into the stability of defective nanotubes at high temperatures. I find that defective nanotubes, exposed to electronic or thermal excitations, show an unexpected self-healing ability, which is intimately linked to their nanometer size.

In Chapter 7, I explore the feasibility of a new scheme to permanently bond nanostructures. Combining total energy and molecular dynamics calculations, I explore the suitability of nanotube-based hooks for bonding. My results indicate that

a large force of 3.0 nN is required to disengage two hooks, which are formed by the insertion of pentagon-heptagon pairs in a $(7,0)$ carbon nanotube. Nanohooks based on various nanotubes are resilient and keep their structural integrity during the opening process. Arrays of hooks, which are permanently anchored in solid surfaces, are a nanoscale counterpart of velcro fasteners, forming tough bonds with a capability of self-repair.

Chapter 8 presents another unusual self-assembled system, 3D polymerized fullerenes, that shows unusual mechanical properties. Combining total energy and structure optimization calculations, I explored new possible crystalline phases of covalently bonded C_{60} fullerenes and determined their structural, elastic, and electronic properties. Motivated by reported observations that bulk structures of polymerized fullerenes may be stiffer than diamond, I have explored possible ways of fullerene polymerization and have identified 12 stable crystal structures as potential candidates for "super-hard" carbon. Even though all these phases are very stiff, none of them exceeds the bulk modulus of diamond. The electronic structure of 3D crystals of polymerized C_{60} depends mainly on the packing structure of the system, with only minor modifications due to the specific inter-fullerene bonding.

Chapter 9 is devoted to the thermal contraction of fullerenes and nanotubes. I perform molecular dynamics simulations to study shape changes of carbon fullerenes and nanotubes with increasing temperature. At low temperatures, these systems gain structural and vibrational entropy by exploring the configuration space at little energy cost. I find that the soft phonon modes, which couple most strongly to the shape, maintain the surface area of these hollow nanostructures. In nanotubes, the gain in entropy translates into a longitudinal contraction, which reaches a maximum at $T \approx 800$ K. Only at much higher temperatures do the anharmonicities in the vibration modes cause an overall expansion.

In Chapter 10, I report a quantitative calculation of the thermal conductivity of

carbon nanotubes, which was done before any reliable experimental data were available. Combining equilibrium and non-equilibrium molecular dynamics simulations with accurate carbon interaction potentials, I determine the thermal conductivity λ of carbon nanotubes and its dependence on temperature. My results suggest an unusually high value $\lambda \approx 6,600$ W/m·K for an isolated (10, 10) nanotube at room temperature, comparable to the thermal conductivity of a hypothetical isolated graphene monolayer, and exceeding that of isotopically pure diamond. I find that these high values of λ are associated with the large phonon mean free path in these systems; substantially lower values are predicted and observed for the basal plane of bulk graphite.

Finally, Chapter 11 deals with the occurrence of a permanent magnetic moment in carbon nanostructures. Magnetic behavior in selected all-carbon nanostructures is investigated by *ab initio* spin density functional theory. Calculational results indicate that particular systems, which are related to schwarzite and contain no undercoordinated carbon atoms, carry a net magnetic moment in the ground state. I postulate that in this and other non-alternant aromatic systems with negative Gaussian curvature, unpaired spins can be introduced by sterically protected carbon radicals.

Some of the figures presented in this dissertation were originally prepared in color. Only one of those color figures may lose some of the information when they are printed in greyscale. The figure that requires color reproduction is denoted in the first line of the caption as "(Color)". Other color figures should not lose any essential information when reproduced in greyscale.

Chapter 2

Electronic and Structural Properties of Carbon Nanohorns

The following discussion of the structural and electronic properties of carbon nanohorns follows that presented in Reference [10].

2.1 Introduction

Since their first discovery [11], carbon nanotubes have drawn the attention of both scientists and engineers due to the large number of interesting new phenomena they exhibit [1, 12, 13, 2], and due to their potential use in nanoscale devices: quantum wires [14], nonlinear electronic elements [15], transistors [16], molecular memory devices [17], and electron field emitters [18, 19, 20, 21]. Even though nanotubes have not yet found commercially viable applications, projections indicate that this should occur in the very near future, with the advent of molecular electronics and further miniaturization of micro-electromechanical devices (MEMS). Among the most unique features of nanotubes are their electronic properties. It has been predicted that single-wall carbon nanotubes [22, 23] can be either metallic or semiconducting, depending on their diameter and chirality [24, 25, 26]. Recently, the correlation between the chi-

rality and conducting behavior of nanotubes has been confirmed by high resolution scanning tunneling microscopy (STM) studies [27, 28].

Even though these studies have demonstrated that atomic resolution can be achieved [27, 28, 29], the precise determination of the *atomic configuration*, characterized by the chiral vector, diameter, distortion, and position of atomic defects, is still a very difficult task to achieve in nanotubes. Much of the difficulty arises from the fact that the electronic states at the Fermi level are only indirectly related to the atomic positions. Theoretical modeling of STM images has been found crucial to correctly interpret experimental data for graphite [30, 31], and has been recently applied to carbon nanotubes [32, 33, 34, 35]. As an alternative technique, scanning tunneling spectroscopy combined with modeling has been used to investigate the effect of the terminating cap on the electronic structure of nanotubes [36, 37].

2.2 Carbon nanohorns as a new class of carbon nanostructures

Among the more unusual systems that have been synthesized in the past few years are cone-shaped graphitic carbon structures [38, 39]. Whereas similar structures have been observed previously near the end of multi-wall nanotubes [40], it is only recently that an unusually high production rate of up to 10 g/h has been achieved for single-walled cone-shaped structures, called "nanohorns", using the CO_2 laser ablation technique at room temperature in absence of a metal catalyst [41]. These conical nanohorns have the unique opening angle of $\approx 20°$.

I consider a microscopic understanding of the electronic and structural properties of nanohorns a crucial prerequisite for understanding the role of terminating caps in the physical behavior of contacts between nanotube-based nano-devices. So far, neither nanohorns nor other cone-shaped structures have been investigated theoretically.

In the following, I study the structural stability of the various tip morphologies, and the inter-relationship between the atomic arrangement and the electronic structure at the terminating cap, as well as the disintegration behavior of nanohorns at high temperatures.

2.3 Electronic and structural properties

2.3.1 Structural properties

Cones can be formed by cutting a wedge from planar graphite and connecting the exposed edges in a seamless manner, as depicted in Figure 2.1. The opening angle of the wedge, called the disclination angle, is $n(\pi/3)$, with $0 \leq n \leq 6$. This disclination angle is related to the opening angle of the cone by $\theta = 2\sin^{-1}(1 - n/6)$. Two-dimensional planar structures (e.g. a graphene sheet) are associated with $n = 0$, and one-dimensional cylindrical structures, such as the nanotubes, are described by $n = 6$. All other possible graphitic cone structures with $0 < n < 6$ have been observed in a sample generated by pyrolysis of hydrocarbons [39]. According to Euler's rule, the terminating cap of a cone with the disclination angle $n(\pi/3)$ contains n pentagon(s) that substitute for the hexagonal rings of planar graphite.

The observed cone opening angle of $\approx 20°$, corresponding to a $5\pi/3$ disclination, implies that all nanohorns contain exactly five pentagons near the tip. I classify the structure of nanohorns by distinguishing the relative positions of the carbon pentagons at the apex which determine the morphology of the terminating cap. My study will focus on the influence of the relative position of these five pentagons on the properties of nanohorns.

The cap morphologies investigated in this study are presented in Figure 2.2. Nanohorns with all five pentagons at the "shoulder" of the cone, yielding a blunt tip, are shown in Figures 2.2(a)–(c). Nanohorns with a pentagon at the apex of the tip,

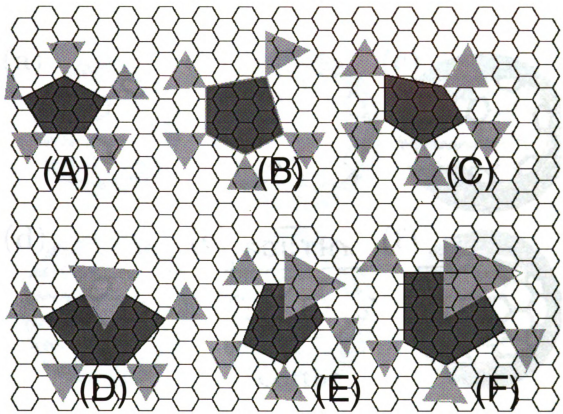

Figure 2.1: Relation between the morphology of a nanohorn and a graphene sheet. Nanohorns can be obtained by cutting off the green (light) parts, folding, and connecting the exposed edges in a seamless manner. The red (dark) area would form the tip of the carbon nanohorn. The labels show the carbon nanohorn types A-F, which are the all possible types taking into account the typical diameter of the nanohorns with the disclination angle $5\pi/3$.

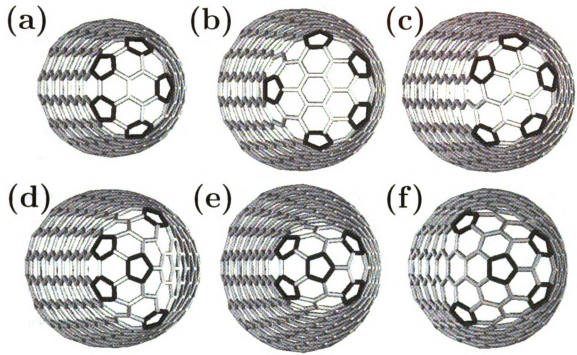

Figure 2.2: Optimized carbon nanohorn structures with a total disclination angle of $5(\pi/3)$, containing five isolated pentagons at the terminating cap. Structures (a) – (c) contain all pentagons at the conical "shoulder", whereas structures (d) – (f) contain a pentagon at the apex. The pentagons are highlighted by a darker color.

surrounded by the other four pentagons at the shoulder, are shown in Figures 2.2(d)–(f). Note that the cone angle of each nanohorn is $\approx 20°$, even though the size of the terminating cap varies with the relative position of the pentagons.

To determine the structural and electronic properties of carbon nanohorns, I used the parameterized linear combination of atomic orbitals (LCAO) technique with parameters determined by *ab initio* calculations for simpler structures [42]. This approach has been found useful to describe minute electronic structure and total energy differences for systems with too large unit cells to handle accurately by *ab initio* techniques[1]. Some of the problems tackled successfully by this technique are the electronic structure and superconducting properties of the doped C_{60} solid [43], the opening of pseudo-gaps near the Fermi level in a (10,10) nanotubes rope [44, 45] and a (5,5)@(10,10) double-wall nanotube [46], as well as fractional quantum conductance in nanotubes [47]. This technique, combined with the recursion technique to achieve an $O(N)$ scaling, can determine very efficiently the forces on individual atoms [8], and had previously been used with success to describe the disintegration dynamics of fullerenes [48], the growth of multi-wall nanotubes [49] and the dynamics of a "bucky-shuttle" [17].

To investigate the structural stability and electronic properties of carbon nanohorns, I first optimized the structures with various cap morphologies, shown in Figure 2.2. For the sake of an easier interpretation of my results, I distinguish the $N_{\rm cap} \approx 40 - 50$ atoms at the terminating cap from those within the cone-shaped mantle, that is terminated by $N_{\rm edge}$ atoms at the other end. I associate the tip region of a hypothetically infinite nanohorn with all the sites excluding the edge. Structural details and the results of my stability calculations are presented in Table 2.1. These

[1] During structure optimization, I keep all sites charge neutral by modifying the diagonal elements of the Hamiltonian, to suppress structural artifacts near the edge. Once the geometry is optimized, the on-site energies are kept at the unperturbed values. Due to the absence of a Hubbard term, this procedure tends to exaggerate the net charge transfer when compared to truly self-consistent calculations.

Quantity	(a)	(b)	(c)	(d)	(e)	(f)
N_{tot}	205	272	296	290	308	217
N_{tip}	172	233	257	251	270	180
N_{edge}	33	39	39	39	38	37
$< E_{coh,tot} >$ (eV)	−7.28	−7.29	−7.30	−7.30	−7.31	−7.28
$< E_{coh,tip} >$ (eV)	−7.36	−7.36	−7.37	−7.36	−7.37	−7.36
$< E_{coh,edge} >$ (eV)	−6.88	−6.88	−6.88	−6.88	−6.87	−6.89
$< E_{coh,pent} >$ (eV)	−7.28	−7.28	−7.28	−7.28	−7.28	−7.28

Table 2.1: Structural data and stability results for carbon nanohorn structures (a)–(f), presented in Figure 2.2. $N_{tot} = N_{tip} + N_{edge}$ is the total number of atoms, which are subdivided into tip and edge atoms. $< E_{coh,tot} >$ is the average binding energy, taken over the entire structure, and $< E_{coh,tip} >$ the corresponding value excluding the edge region. $< E_{coh,edge} >$ is the binding energy of the edge atoms, and $< E_{coh,pent} >$ is the average over the pentagon sites in each system.

results indicate that atoms in nanohorns are only ≈0.1 eV less stable than in graphite. The relative differences in $< E_{coh,tot} >$ reflect the strain energy changes induced by the different pentagon arrangements. To minimize the effect of under-coordinated atoms at the edge on the relative stabilities, I excluded the edge atoms from the average when calculating $< E_{coh,tip} >$. Since my results for $< E_{coh,tip} >$ and $< E_{coh,tot} >$ follow the same trends, I believe that the effect of edge atoms on the physical properties can be neglected for structures containing hundreds of atoms. Even though the total energy differences may appear minute on a per-atom basis, they translate into few electron-volts when related to the entire structure. My results suggest that the under-coordinated edge atoms are all less stable than the cone mantle atoms by ≈0.5 eV. Also atoms in pentagons are less stable than those in hexagons by ≈0.1 eV, resulting in an energy penalty of ≈0.5 eV to create a pentagon if the strain energy induced by bending the lattice could be ignored.

When comparing the stabilities of the tip regions, described by $< E_{coh,tip} >$, I found no large difference between blunt tips that have all the pentagons distributed along the cylinder mantle and pointed tips containing a pentagon at the apex. I found the structure shown in Figure 2.2(c) to be more stable than the other blunt structures

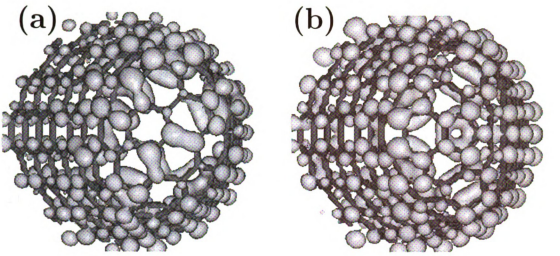

Figure 2.3: Simulated STM images in the tip region for (a) the nanohorn shown in Figure 2.2(c) and (b) the nanohorn shown in Figure 2.2(d). These results for the occupied electronic states near the Fermi level, corresponding to the bias voltage of $V_b = 0.2$ V, are suggestive of a net electron transfer from the hexagonal to the pentagonal sites. The charge density contour displayed corresponds to the value of $\rho = 1.35\times10^{-3}$ electrons/Å^3. Dark lines depict the atomic bonds to guide the eye.

with no pentagon at the apex. Similarly, the structure shown in Figure 2.2(e) is most stable among the pointed tips containing a pentagon at the apex. Equilibrium carbon-carbon bond lengths in the cap region are $d_{CC} = 1.43 - 1.44$ Å at the pentagonal sites and $d_{CC} = 1.39$ Å at the hexagonal sites, as compared to $d_{CC} = 1.41 - 1.42$ Å in the mantle. This implies that the "single bonds" found in pentagons should be weaker than the "double bonds" connecting hexagonal sites, thus confirming my results in Table 2.1 and the analogous behavior in the C_{60} molecule.

2.3.2 Electronic structure

Since pentagon sites are defects in an all-hexagon structure, they may carry a net charge [50, 51]. To characterize the nature of the defect states associated with these sites, I calculated the electronic structure at the tip of the nanohorns. The charge density associated with states near E_F, corresponding to the local density of states at that particular position and energy, is proportional to the current observed in STM

experiments. To compute the local charge density associated with a given eigenstate, I projected that state onto a local atomic basis. The projection coefficients were used in conjunction with real-space atomic wave functions from density functional calculations [31] to determine the charge density corresponding to a particular level or the total charge density. To mimic a large structure, I convoluted the discrete level spectrum by a Gaussian with a full-width at half-maximum of 0.3 eV. Using this convoluted spectrum, I also determined the charge density associated with particular energy intervals corresponding to STM data for a given bias voltage.

In Figure 2.3, I present such simulated STM images for the nanohorns represented in Figures 2.2(c) and 2.2(d). I show the charge density associated with occupied states within a narrow energy interval of 0.2 eV below the Fermi level[2] as three-dimensional charge density contours, for the density value of $\rho = 1.35 \times 10^{-3}$ electrons/Å^3. Very similar results to those presented in Figure 2.3 were obtained at a higher bias voltage of 0.4 eV. As seen in Figure 2.3, $pp\pi$ interactions dominate the spectrum near E_F. These images also show a net excess of electrons on the pentagonal sites as compared to the hexagonal sites. This extra negative charge at the apex should make pointed nanohorn structures with a pentagon at the apex better candidates for field emitters [18, 19, 20, 21] than structures with no pentagon at the apex and a relatively blunt tip.

It has been shown previously that theoretical modeling of STM images is essential for the correct interpretation of experimental data. Atomically resolved STM images, however, are very hard to obtain especially near the terminating caps of tubes [36, 37] and cones, due to the large surface curvature that can not be probed efficiently using current cone-shaped STM tips. A better way to identify the tip structure may

[2]The nanohorn structures considered in my calculation are clusters containing edge atoms. I found that due to the electron transfer towards the under-coordinated atoms at the edge, the "Fermi level" of these clusters may drop by as much as $\approx 1.0 - 1.2$ eV with respect to that of a graphene monolayer. To compensate for this artifact, I excluded the edge region from the calculated density of states and found the E_F value to lie very close to that of a graphene monolayer.

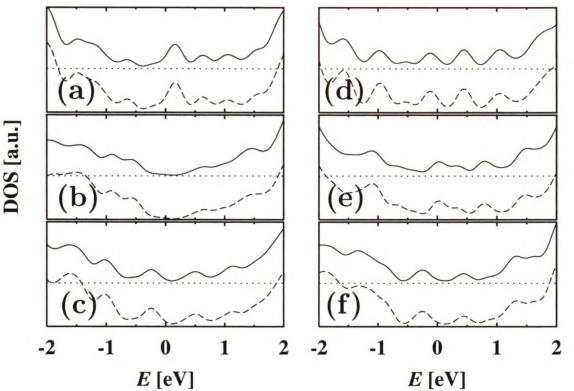

Figure 2.4: Electronic densities of states, normalized per atom and shown in consistent arbitrary units, for the terminating cap of the tip (solid line) and for the pentagon sites only (dashed line) of nanohorn structures shown in Figure 2.2. The similarity between the results for the entire cap and the pentagon sites necessitated a vertical offset of one set of data for an easy distinction, thus indicating that variations in the arrangement of pentagons affect the densities of states not only at the pentagonal sites, but within the entire cap region. The most marked differences are noted near the Fermi level, at $E \approx 0$ eV.

consist of scanning tunneling spectroscopy (STS) measurements in the vicinity of the tip. This approach is based on the fact that in STS experiments, the normalized conductance $(V/I)(dI/dV)$ is proportional to the density of states which, in turn, is structure sensitive. I have calculated the density of states at the terminating cap for the different nanohorn structures shown in Figure 2.2. My results are shown in Figure 2.4, convoluted using a Gaussian with a full-width at half-maximum of 0.3 eV.

To investigate the effect of pentagonal sites on the electronic structure at the tip, I first calculated the density of states only at the 25 atoms contained in the five terminating pentagons. The corresponding densities of states, shown by the dashed curve in Figure 2.4, are found to vary significantly from structure to structure near the Fermi level. Thus, a comparison between the densities of states at $E \approx E_F$ should offer a new way to discriminate between the various tip morphologies. For an easy comparison with experiments, I also calculated the density of states in the entire terminating cap, including all five pentagons and consisting of $N_{cap} \approx 40 - 50$ atoms, depending on the structure. The corresponding density of states, given by the solid line in Figure 2.4, is vertically displaced for easier comparison. My results show that the densities of states, both normalized per atom, are very similar. Thus, I conclude that the pentagonal sites determine all essential features of the electronic structure near the Fermi level at the tip. I note that a perturbation of the electronic structure far from defects has also been predicted in nanotubes [52].

2.4 Thermal stability

Next, I have studied the heat resilience [41] as well as the decay mechanism of nanohorns at extremely high temperatures using molecular dynamics simulations [53]. In my canonical molecular dynamics simulations, I keep the structure at a constant temperature using a Nosé-Hoover thermostat [54, 55], and use a fifth–order Runge–

Kutta interpolation scheme to integrate the equations of motion, with a time step of $\Delta t = 5 \times 10^{-16}$ s. I found the system to remain structurally intact within the temperature range from $T = 2,000 - 4,000$ K. Then, I heated up the system gradually from $T = 4,000$ K to 5,000 K within 4,000 time steps, corresponding to a time interval of 2 ps. My molecular simulations show that nanohorn structures are extremely heat resilient up to $T \approx 4,500$ K. At higher temperatures, I find these structures to disintegrate preferentially in the vicinity of the pentagon sites. A simultaneous disintegration of the nanohorn structures at the exposed edge, which also occurs in my simulations, is ignored as an artifact of finite-size systems. The preferential disintegration in the higher strain region near the pentagon sites, associated with a large local curvature, is one reason for the observation that nanohorn tips are opened easily at high temperatures, in presence of oxygen [41].

2.5 Summary

In summary, I used parameterized linear combination of atomic orbitals calculations to determine the stability, optimum geometry and electronic properties of nanometer-sized capped graphitic cones, called nanohorns. I considered different nanohorn morphologies that differ in the relative location of the five terminating pentagons. I found a net electron transfer to the pentagonal sites of the cap. This negative excess charge is seen in simulated scanning tunneling microscopy images of the various structures at different bias voltages. I found that the density of states at the tip, observable by scanning tunneling spectroscopy, can be used to discriminate between different tip structures. My molecular dynamics simulations indicate that disintegration of nanohorns at high temperatures starts in the highest-strain region near the tip.

Chapter 3

Microscopic Formation Mechanism of Carbon Nanopeapods

The following discussion of possible microscopic formation mechanisms of carbon nanopeapods follows that of Reference [56].

3.1 Carbon nanopeapods: A new type of hybrid carbon materials

A new type of self-assembled hybrid structures called "nanopeapods," consisting of fullerene arrays inside single-wall carbon nanotubes, have recently been reported [57, 58, 59, 60, 61, 62]. Potential uses of nanopeapods range from nanometer-sized containers for chemical reactions [60] to data storage [17], and possibly high-temperature superconductors [63]. Even though the encapsulation of fullerenes (such as C_{60}) in nanotubes is favorable on energetic grounds [17, 64, 65] and occurs rapidly by exposing nanotubes to sublimed fullerenes [57, 58, 59, 60, 61], virtually nothing is known about how the fullerenes enter the nanotubes when forming the nanopeapods.

3.2 Possible formation mechanisms of nanopeapods

A statistical mechanics approach, which considers only the initial and final state, describes only the equilibrium state after an infinite time [65]. It can say nothing about the likelihood of fullerene encapsulation in a finite time, as it ignores any activation barriers along the reaction path. Only trajectory calculations based on the complex potential energy surface of the system can provide detailed answers about the dynamics and intermediate steps involved in the formation of nanopeapods.

An important current controversy involves the question whether fullerenes enter through the open ends of perfect nanotubes or whether defects in the wall play an important role as entry channels. The extremely high filling ratio of up to 100% [61] appears hard to achieve even within few days if the only entry channels are the two open ends of each tube. In such a case, the fullerene kinetics is limited and even a single impurity may block an entry channel. On the other hand, only few openings in the tube walls have been observed in High-Resolution Transmission Electron Microscopy (HRTEM) images [66]. Another important question, which a statistical approach can not answer, is whether the encapsulation process, be it through an open end or through a defect, occurs directly from the gas phase, or involves a diffusive motion along the wall.

Here, I present a large-scale simulation for the entry of a C_{60} molecule into a $(10, 10)$ carbon nanotube via different scenarios, illustrated in Fig. 3.1. I consider the encapsulation through the open end of a free-standing nanotube [Fig. 3.1(a)] and through the open end of a nanotube bundle [Fig. 3.1(b)]. These scenarios are compared to the C_{60} entry through a defect, in my model a large opening in the nanotube wall [Fig. 3.1(c)]. I propose that what has been interpreted as harmless "amorphous overcoating" of perfect single-wall nanotubes in HRTEM images may

indeed represent defective nanotube segments with openings large enough to let a fullerene pass through. Formation of such large defects may occur, I believe, during the harsh purification process that is a necessary prerequisite for peapod formation [60]. By assuming that the C_{60} adsorbs on the wall prior to encapsulation, I take advantage of the enhanced probability of the fullerene to find an entry channel into a nanotube within the lower-dimensional phase space probed by the C_{60} diffusing along the wall, as compared to a fullerene in the gas phase. My calculations elucidate not only which of these processes is most likely, but also the optimum temperature window for the peapod formation.

I calculate the potential energy of the fullerene-nanotube system using an electronic Hamiltonian that had been used successfully to describe the formation of multi-wall nanotubes [49] and the dynamics of a "bucky-shuttle" device [17]. This approach describes accurately not only the covalent bonding within the graphitic substructures, but also the modification of the fullerene-nanotube interaction due to the inter-wall interaction and possibly the presence of unsaturated bonds at defect sites or tube edges. I find the use of an electronic Hamiltonian to be required in this system, as analytical bond-order potentials do not describe the rehybridization at defect sites and tube ends with a sufficient precision. Once the quantum nature of the interatomic interactions has been taken into account, the trajectories of the heavy carbon atoms are described reliably in classical manner.

In Fig. 3.1 I present schematic views of the encapsulation scenarios together with the calculated potential energy surfaces in the $x-y$ plane that contains the tube axes, the center of the C_{60} molecule and the defect. The tube structures underlying the potential energy surfaces have been globally optimized. They reflect the relaxation at the open end of the tube and the edges of a large defect in the tube wall, representing an extended vacancy formed during the harsh purification process. I consider a defect formed by removing 76 atoms from the wall, with a diameter of $\approx$13.6 Å, just large

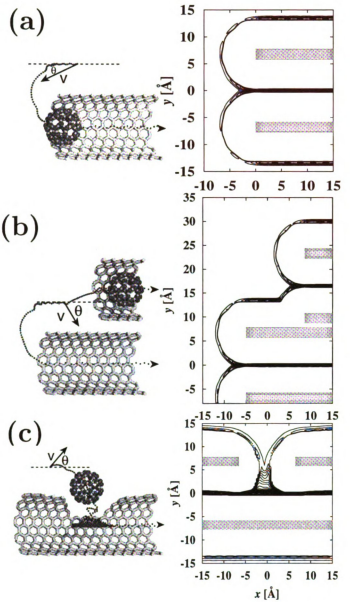

Figure 3.1: Perspective views (left panels) and potential energy surfaces (right panels) for the encapsulation of a C_{60} molecule in a $(10, 10)$ nanotube under different scenarios. Dotted lines indicate possible C_{60} trajectories, characterized by the launch velocity v and launch angle θ with respect to the tube axis. The potential energy surfaces are shown in the $x - y$ plane containing the center of the fullerene and the tube axis x. Adjacent energy contours are separated by 0.01 eV; the position of the tube walls is indicated by the solid gray areas. The scenarios involve C_{60} encapsulation through (a) the open end of an isolated $(10, 10)$ nanotube, (b) the open end of bundled $(10, 10)$ nanotubes, and (c) a large opening in the $(10, 10)$ nanotube wall, centered in the $x - y$ plane.

enough to permit an unhindered entry of a C_{60} molecule.

When following an "optimum" trajectory starting outside the tube, a C_{60} molecule may first physisorb on the outer wall, thus gaining $\approx$0.07 eV. My energy contour plots in Fig. 3.1 suggest that the fullerene diffuses virtually freely along the tube wall. Since the adsorption potential is relatively shallow, the fullerene's angular velocity along the perimeter is limited by requiring the centrifugal force not to exceed a critical value for radial detachment. Consequently, the fullerene should follow a near-axial helical trajectory within a narrow 1D channel in the $x-y$ plane during its diffusive motion along the tube surface. Due to the large inertia of the C_{60} molecule and the absence of corrugations along the potential energy surface, virtually no rotations are excited as the fullerene slides along the tube wall. Upon entering the nanotube, the C_{60} gains an additional 0.36 eV [67].

The absence of activation barriers for all fullerene encapsulation scenarios depicted in Fig. 3.1 is surprising for two reasons. First, it suggests that the strong attraction to the undercoordinated atoms at the tube or defect edges does not trap the fullerene, but only modifies the entry channel without hindering the encapsulation[1]. Second, it leaves the origin of the observed optimum temperature of $\approx$400°C for C_{60} encapsulation an open question.

The likelihood of C_{60} encapsulation depends on its initial conditions and the topology of the entire potential energy surface, as suggested by the sample trajectories in Fig. 3.1. In my molecular dynamics simulations, I initially placed the C_{60} molecule at equilibrium radial distance from the tube. I then calculated C_{60} trajectories in the $x-y$ plane using time steps of 5×10^{-16} s, by varying the launch speed v from $0-300$ m/s in 1 m/s increments and the launch angle θ with respect to the tube axis from $-90°$ to $+90°$ in 1° increments. The calculation of all 54,000 trajectories

[1]Due to their enhanced reactivity, unsaturated edges form a stronger bond with the fullerenes than edges saturated with hydrogen or other elements. It is conceivable that fullerenes could get trapped near vacancies that are smaller or comparable in size with the fullerene.

for each encapsulation pathway would not be computationally feasible without approximations. I described the fullerene-nanotube interaction by the potential energy surfaces presented in Fig. 3.1, thus implying that both the C_{60} and the nanotube are structurally rigid.

For each set of initial conditions, I found that the ultimate outcome of each trajectory regarding encapsulation is decided within less than 10^6 time steps. I also found that all physically interesting phenomena occur within a velocity range between $50 - 200$ m/s, the lower bound marking the onset of C_{60} mobility along the tube. The upper end of this range corresponds to high temperatures, at which fragmentation and tube fusion are to be expected. Consequently, I will discuss the encapsulation under the specific scenarios within this velocity range.

3.3 Role of defects in the formation pathway of nanopeapods

The outcome of the encapsulation process through the end of an isolated nanotube, depicted in Fig. 3.1(a), is shown in Fig. 3.2. The scatter diagram of Fig. 3.2(a) condenses the information of all trajectories regarding encapsulation. A black mark denotes a trajectory with a launch velocity and angle that leads to encapsulation, such as that shown in Fig. 3.2(b). Similarly, a white field marks failed encapsulation, such as depicted in the trajectory of Fig. 3.2(c). Consequently, the fraction of the dark area is proportional to the probability of encapsulation. The scatter diagram, dominated by white color, suggests that encapsulation through the open end of an isolated nanotube should be very rare. The main reason is the relatively narrow and shallow channel in the potential energy surface of Fig. 3.1(a), which the fullerene must follow to reach the inside of the tube. At very low velocities, the fullerene gets trapped in one of the shallow potential energy wells outside the tube wall. At too

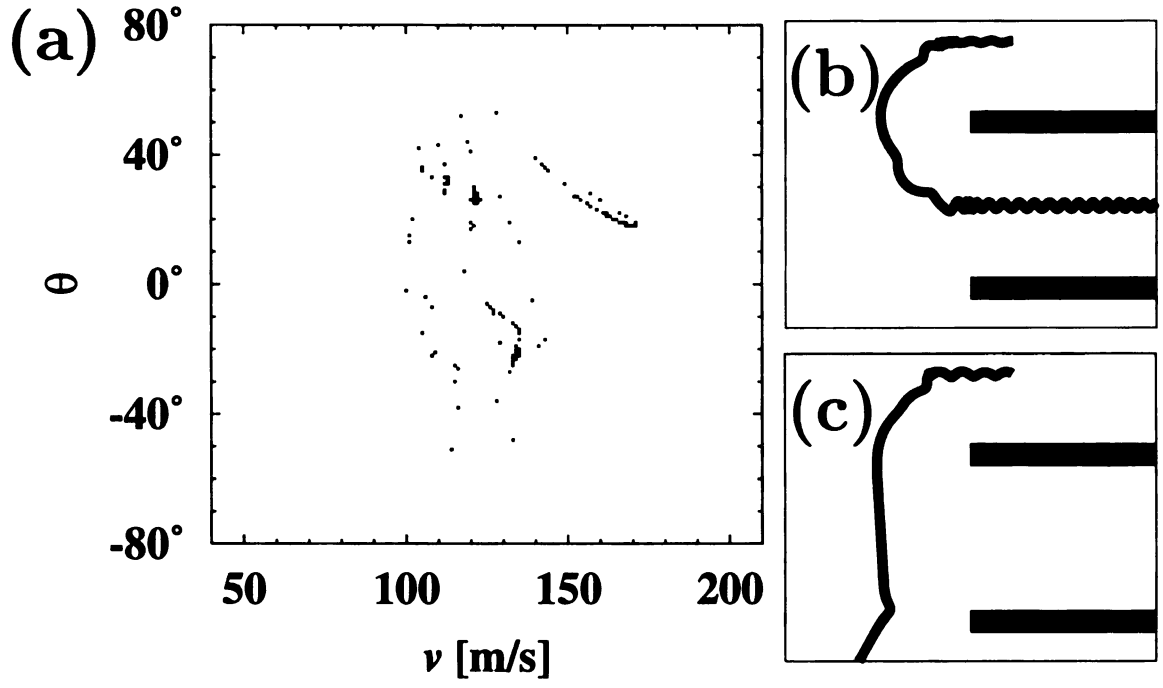

Figure 3.2: (a) Scatter diagram showing the probable outcome of a C_{60} encapsulation through the open end of an isolated $(10, 10)$ nanotube, as a function of the fullerene launch velocity v and launch angle θ. Initial conditions leading to a successful encapsulation are marked in black, those which do not lead to encapsulation are marked in white in the scatter diagram. A sample successful encapsulation trajectory is depicted in (b), an unsuccessful trajectory in (c).

high velocities, on the other hand, the C_{60} is incapable of following the tight "U-turn" in the potential energy surface, as illustrated in Fig. 3.2(c).

In view of the low estimated probability of encapsulation through the end of an isolated tube, I considered next the analogous process at the end of a nanotube bundle, consisting of $(10, 10)$ tubes with an inter-wall separation of 3.4 Å, depicted in Fig. 3.1(b). As suggested by the two successful trajectories in the left panel of Fig. 3.1(b), the more complex potential energy surface for this system increases the number of entry channels, thus enhancing the probability of encapsulation. The results of my trajectory calculations, summarized in the scatter diagram of Fig. 3.3(a), indeed show a somewhat higher encapsulation probability as compared to the single-

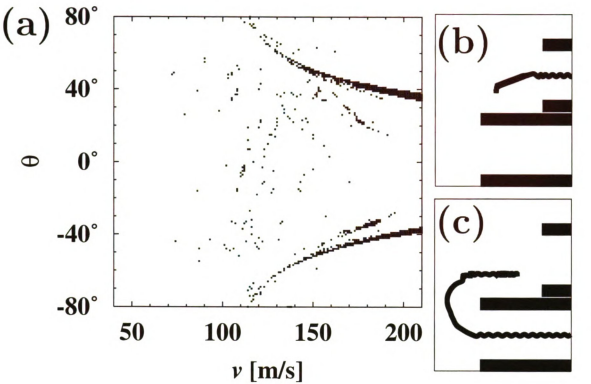

Figure 3.3: (a) Scatter diagram showing the probable outcome of a C_{60} encapsulation through the open end of bundled (10, 10) nanotubes, as a function of the fullerene launch velocity v and launch angle θ . Initial conditions leading to a successful encapsulation are marked in black, those which do not lead to encapsulation are marked in white in the scatter diagram. Sample trajectories, describing successful encapsulation in two different tubes, are depicted in (b) and (c).

tube scenario. In comparison to Fig. 3.2(a), I observe two solid dark regions for velocities beyond $\approx$150 m/s and $\theta \approx \pm 40°$. These regions correspond to trajectories that first follow the wall of one tube and continue inside the neighboring tube, as shown in Fig. 3.2(b). This new channel is relatively narrow due to the "S"-shape of the tube-fullerene interaction potential well, shown in the right-hand panel of Fig. 3.1(b). As in the case of an isolated tube, trajectories involving a "U-turn", depicted in Fig. 3.3(c), form an additional entry channel, responsible for the rare encapsulation events in the remaining region of the scatter diagram. I conclude that even in the case of a bundle, the probability of encapsulation through the end is rather low.

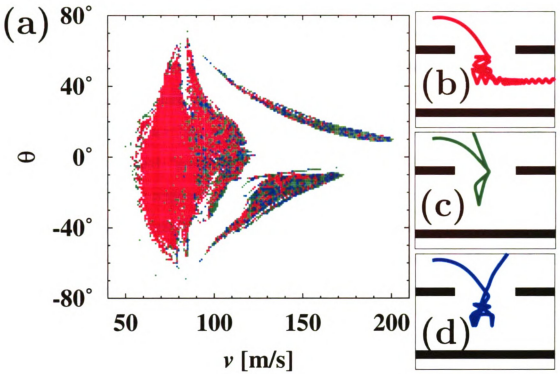

Figure 3.4: (Color) (a) Scatter diagram showing the probable outcome of a C_{60} encapsulation through a large opening in the wall of a $(10, 10)$ nanotube, as a function of the fullerene launch velocity v and launch angle θ. Events are color coded according to the final state. Conditions that do not lead to encapsulation are marked in white. Conditions leading to encapsulation, with a sample trajectory shown in (b), are marked in red. Initial conditions and corresponding trajectories involving a temporary entry of the fullerene into the tube, followed by an escape after multiple scattering events, are shown in green if the final velocity has a negative x-component (c) and in blue if the final velocity has a positive x-component (d).

The outcome of the encapsulation process through a large opening in the side wall of the $(10, 10)$ nanotube, depicted in Fig. 3.1(c), is shown as a scatter diagram in Fig. 3.4(a). In comparison to Figs. 3.2(a) and 3.3(a), the dark area in the scatter diagram of Fig. 3.4(a) is substantially larger, yielding a 30-fold increase of the cross-section for the C_{60} entry. In the following, I focus on the encapsulation through the large wall opening as the most likely process leading to peapod formation.

The scatter diagram of Fig. 3.4(a) shows a complex pattern consisting of large areas corresponding to the C_{60} entering the tube. Among these events, I have marked

those trajectories leading to a definitive encapsulation, as depicted in Fig. 3.4(b), in red. The "green" and "blue" trajectories, shown in Figs. 3.4(c) and (d), involve a temporary entry of the C_{60} molecule into the tube. In that case, after multiple scattering events, the fullerene may eventually escape in the backward ("green event") or the forward direction ("blue event"). Since such multiple scattering processes are chaotic, the "blue" and "green" events are homogeneously intermixed rather than separated into specific regions in Fig. 3.4(a).

To interpret the complex pattern in the scatter diagram of Fig. 3.4(a), I took a closer look at the individual trajectories. For launch velocities below 50 m/s, the C_{60} becomes trapped in one of the local minima and never reaches the defect. The highest probability of a successful encapsulation with an axial launch ($\theta = 0°$) is achieved at velocities ranging from 50 m/s$\leq v \geq$120 m/s. Axial launches with velocities exceeding $\approx$120 m/s overshoot the hole. C_{60} encapsulation is still possible for fast launches, but requires large launch angles and involves one or several radial reflections off the wall, as shown schematically in Fig. 3.1(c). For a given nonzero launch angle, the largest launch velocity allowing the fullerene to enter the tube involves a straight trajectory with no radial reflections. This is the case for the trajectories depicted in Figs. 3.4(b)-(d), for launch angles $\theta \approx 10°$ and $v \leq 200$ m/s. At lower launch velocities, a radial reflection from the tube wall causes the fullerene to overshoot the hole. As the velocity is reduced further, the point of first radial reflection is shifted closer to the launch site, allowing the fullerene to successfully enter the nanotube again. At a constant launch angle such as $\theta = 40°$, I can distinguish up to seven alternating regions associated with "successful" and "unsuccessful" trajectories. Each of these contiguous regions in Fig. 3.4(a) can be characterized by the number of radial reflections between the launch site and the hole edge.

Maybe my most important result is the finding that, in absence of inelastic scattering, the probability of successful encapsulation ("red" events) is largest in the

velocity range between $80 - 120$ m/s and almost independent of the launch angle θ. This suggests that not the launch direction, but rather the kinetic energy of the C_{60} molecule decides the outcome. In view of the restricted motion of the C_{60} molecule along the tube surface, which reduces the number of degrees of freedom, I find that this velocity window translates into a kinetic temperature of the C_{60} close to 400°C.

It is remarkable that the optimum temperature for peapod formation, as predicted by my calculation, falls into the observed temperature range from $350 - 450$°C [60]. Previous explanations of this optimum temperature window were only based on plausibility arguments suggesting a low C_{60} mobility at low temperatures and a closure of the wall defects or fullerene fusion [68] under annealing conditions. I believe that the quantitative agreement between theory and observation also provides an indirect evidence that the microscopic encapsulation mechanism involves defects in the tube wall.

My calculations discussed so far have been based on the assumption that the microscopic degrees of freedom are decoupled from the macroscopic motion of the C_{60} molecule. Effectively, the possibility of energy transfer between the macroscopic and microscopic degrees of freedom introduces a damping mechanism. This new inelastic channel could convert some of the "green" and "blue" trajectories, depicted in Fig. 3.4, into successful encapsulation events, thus further increasing the cross-section for C_{60} encapsulation.

To investigate additional phenomena that may occur when none of the microscopic degrees of freedom are frozen, I performed a molecular dynamics simulation of the fullerene-tube interaction in a canonical simulation at synthesis temperature. Considering the motion of all the atoms carries a large computational overhead, since calculating the electronic structure self-consistently at each time step slows down the simulation by five orders of magnitude. An important structural change I observed at elevated temperatures was the occurrence of quadrupolar tube deformations near

the hole due to the reduced structural rigidity at that site. This, together with a strong tube bending mode that reduces the size of the entry channel, decreases the probability of C_{60} capture.

3.4 Summary

In summary, I investigated the microscopic mechanism of $(C_{60})_n@(10,10)$ peapod formation by considering the entry of the fullerene into the tube either through an extended vacancy in the wall or the open end. My total energy calculations indicate that presence of dangling bonds at the unsaturated edge of the uncapped end or of a large enough vacancy increases the fullerene-nanotube interaction, thus promoting – rather than hindering – the fullerene entry into the tube. Using these potential energy surfaces, the likelihood of a C_{60} encapsulation was investigated for scenarios involving end-on encapsulation in isolated and bundled tubes, and for encapsulation through large defects in the wall. Extensive molecular dynamics simulations, performed under these scenarios as a function of the C_{60} launch velocity and angle with respect to the tube axis, indicate that the most efficient peapod formation mechanism involves diffusive motion along the wall and encapsulation through a large opening in tube wall. The C_{60} encapsulation occurs most likely within a narrow range of launch velocities that agrees well with the experimentally observed temperature window. The efficiency of the filling process through openings in the tube wall is expected to improve with increasing concentration of defects up to the point where, due to a significant fraction of atoms missing or displaced, the tubes lose their structural integrity.

Chapter 4

Energetics of Encapsulation and Fusion of Fullerenes in Nanopeapods

The following discussion of the encapsulation and fusion of fullerenes inside carbon nanotubes, namely fusion of fullerenes inside carbon nanopeapods, follows that presented in References [69, 70]. In analogy to fullerene fusion, I also comment on the possibility of diamondoid fusion inside nanotubes based on *ab initio* total energy calculations reported in Reference [71].

4.1 Unusual properties of carbon nanopeapods

The first observation of the hierarchical self-assembly of C_{60} molecules and single-wall carbon nanotubes (SWNTs) to peapods by high-resolution transmission electron microscopy (HRTEM) [57] was followed by reports of encapsulating other fullerenes and metallofullerenes in single-walled carbon nanotubes [72, 61, 73, 74, 75, 76, 77].

Several intriguing observations regarding peapods await explanation. For one, high-resolution transmission electron microscopy images [61, 73, 74, 75, 76, 78], elec-

tron diffraction [77] and Raman spectra [79] suggest the observed equilibrium spacing between fullerenes in peapods to be smaller by $3-4\%$ than in three-dimensional crystals, but larger than in polymerized solids. Also, in contrast to 2-D and 3-D crystals [80, 81], where polymerization of fullerenes does not easily occur even under high pressures and temperatures, fullerenes fuse rather readily to long capsules when encapsulated in nanotubes [57, 68, 60]. For fusion to be enabled at 1100°C, significantly below the decomposition temperature of fullerenes [48] close to $4,000$°C, the enclosing nanotube must play a crucial role. Here I investigate the packing of fullerenes in various nanotubes and determine the optimum energy path for thermal fusion of fullerenes, including the identification of activation barriers and transition-state geometries.

4.2 Energetics of fullerenes in nanopeapods

Figure 4.1 (a) shows schematically the static force associated with the energy gain during the encapsulation of a fullerene in a nanotube. To decide which fullerene may enter into which nanotube, in Figure 4.1 (b) I plot the encapsulation energy of C_{60} and C_{84} in single-wall nanotubes with radii R_{NT} in the range $0.6\text{ nm} \leq R_{NT} \leq 0.8\text{ nm}$. As expected, encapsulation is favored only in nanotubes that are sufficiently wide. On the other hand, the encapsulation energy in very wide tubes should be smaller and comparable to the adsorption energy on graphite. These results are in general agreement with reported results based on an alternative potential [65, 82, 83]. My results suggest that each fullerene of radius R_F shows a preference for nanotubes with $R_{NT} \approx R_F + 0.3\text{ nm}$. For this snug fit, encapsulation results in an energy gain of ≈ 0.4 eV for $C_{60}@(10,10)$ and $C_{84}@(11,11)$ due to the attractive interaction between the tube wall and the fullerene. This value agrees with *ab initio* calculations [67], but is lower than empirical fits to experimental data [65, 82, 83, 84]. I found that

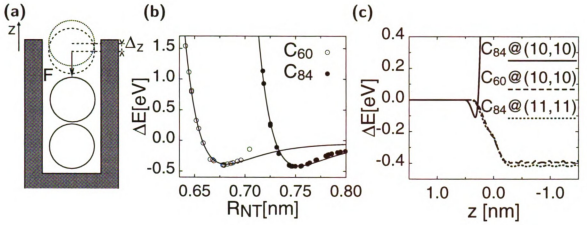

Figure 4.1: Energetics of fullerene encapsulation. (a) During the insertion into a nanotube, a fullerene is pulled in by a "capillary" force F, which is linked to the energy gain upon axial displacement Δz. (b) The encapsulation energy ΔE of C_{60} (○) and C_{84} (●) in single-wall carbon nanotubes with radii R_{NT} ranging from 0.6 nm$\leq R_{NT} \leq$0.8 nm. Best fitting fullerene/nanotube pairs show an encapsulation energy of ≈0.4 eV. (c) Energy change during the fullerene insertion process along the tube axis z, with $z = 0$ at the tube end. C_{60} and C_{84} are pulled into the best fitting $(10, 10)$ and $(11, 11)$ nanotubes by $F \approx 0.1$ nN, reflected in a constant constant slope of $\Delta E/\Delta z$ near the tube end. The high energy cost prevents the entry of the C_{84} fullerene into the narrow $(10, 10)$ nanotube.

the encapsulation energy of fullerenes is represented well in a continuum approximation [85], shown by the solid lines in Figure 4.1 (b), by modeling fullerenes as spheres inside atomically smooth nanotubes. No special preference regarding tube chirality was observed, suggesting the possibility to use peapod formation as a tool to separate tubes by diameter.

In Figure 4.1 (c), I display the energy associated with the insertion of C_{60} and C_{84} in the $(10, 10)$ and $(11, 11)$ nanotubes. For the energetically most favorable pairs, open-end insertion is associated with a "capillary" force $F = \Delta E/\Delta z \approx 0.1$ nN near the tube end at z=0. As shown in Figure 4.1 (c), insertion of the large C_{84} fullerene in the narrower $(10, 10)$ nanotube is energetically unfavorable.

The static capillary force $F \approx 0.1$ nN, when divided by the cross-section area of the enclosing nanotube, yields a static pressure in the sub-GPa range. At nonzero temperature, fullerenes packed inside a peapod are also subject to a dynamical pres-

sure, resulting from collisions with neighboring fullerenes. In the temperature range close to 1,000 K, when fusion occurs [68], collisions between thermally equilibrated fullerenes lead to forces close to 1 nN, representing accordingly higher nominal pressures in the GPa range. This nominal pressure is found to be a very important factor in determining the equilibrium structure of nanopeapods [70], and could account for the distance reduction between fullerenes when they form one dimensional crystals inside nanotubes [61, 77].

4.3 Chemical reactions inside carbon nanotubes

The postulated high nominal pressure inside nanotubes suggests a possible use of nanotubes as nanoscale autoclaves to promote chemical reactions. For example, HRTEM observations indicate that under electron irradiation [57] or at elevated temperatures [68, 60], fullerenes fuse more readily inside a nanotube than in 2 D and 3 D crystals [80, 81]. In addition to fullerenes, carbon nanotubes could also encapsulate other species such as diamondoid molecules [5] to form one dimensional diamond wires inside carbon nanotubes by taking advantage of the physical confinement provided by nanotube template, and a high nominal pressure [71]. *Ab initio* calculations indicate that diamondoids gain energy after encapsulation inside a nanotube. Similar to fullerenes, each diamondoid molecule has a preferred diameter range for efficient encapsulation. I found that doped diamondoid molecules should fuse into one dimensional nanometer sized diamond whiskers more easily inside a nanotube than in free space.

4.3.1 Fusion of fullerenes in carbon nanopeapods

Large-scale structural changes, including fusion, can be achieved by a finite sequence of generalized Stone-Wales transformations, which involve only bond rotations

and avoid bond breaking. Using a graphical search program, I determine the optimum reaction pathway for thermal fusion of fullerenes. Search of the phase space by the 'string method' provides detailed information about the optimum pathway, including the identification of activation barriers and transition-state geometries. I find the fusion process to be exothermic. The fusion dynamics is fast in spite of the formidable total activation barrier close to 5 eV, associated with each Stone-Wales transformation, since bond rotations turn out to be multi-step processes with lower individual activation barriers.

The fusion of two C_{60} molecules to a C_{120} capsule, which has been observed in peapods [60, 68], is driven by the energy gain associated with reducing the local curvature in the system. Still, this reaction involves a large-scale morphological change and will only occur if the required activation barrier is small.

It appears that the most likely fusion path may involve a sequence of bond rotations, called generalized Stone-Wales (GSW) transformations. GSW transformations are known to require much lower activation energies than processes involving bond breaking, and have been studied extensively in sp^2 bonded carbon structures [86]. Optimum pathway for the $2C_{60} \rightarrow C_{120}$ fusion reaction, involving the smallest number of generalized Stone-Wales bond rotations is depicted in Fig. 4.2.

Close inspection of the reaction energy along the contiguous optimum fusion path in Fig. 4.3 indicates a sequence of 23 activated processes connecting the 24 metastable states. I find the activation energy barriers $\Delta E_{GSW} \approx 5$ eV of these GSW transformations to be significantly lower than in graphite, as expected for Stone-Wales processes in non-planar structures due to the deviation from sp^2-bonding. In presence of extra carbon atoms, the activation barriers for GSW transformations may be lowered further to below 4 eV by autocatalytic reactions [87, 88]. Also, under electron irradiation, this process can proceed relatively fast in view of the high rate of sub-threshold energy transfer to the structure [89]. In extended fullerene systems,

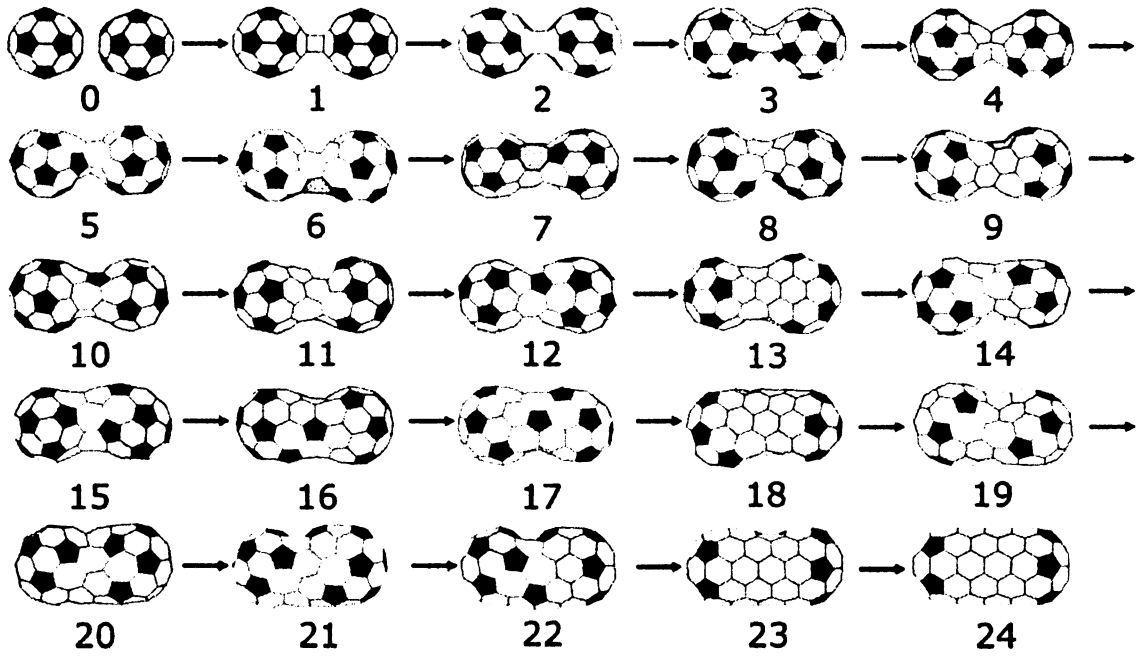

Figure 4.2: Optimum pathway for the $2C_{60} \rightarrow C_{120}$ fusion reaction, involving the smallest number of generalized Stone-Wales bond rotations, determined by a graphical search of all possible bond rotation sequences. Polygons other than hexagons are emphasized by color and shading.

moreover, the energy release during the fusion process should heat up the structure locally, thus further promoting activated processes in the local vicinity.

In spite of its lower activation barrier in comparison to the GSW steps, the initial (2 + 2) cycloaddition reaction between the structures "0" and "1" may play an important role, and possibly even limit the rate of the fusion process. Fusion can only be initiated in the optimum geometry, where two double bonds in adjacent fullerenes face each other at the contact point. The probability of this configuration will multiply the attempt frequency ν of the $0 \rightarrow 1$ reaction in the Arrhenius formula[1] and thus reduce the reaction rate, since the low activation barrier of $\approx$0.7 eV, only applies to attempts with the optimum fullerene orientation.

To estimate the probability of the configuration required for the $(2+2)$ cycloaddition to occur, I first consider the phase space describing the motion of two rigid

[1]The Arrhenius formula determines the reaction rate as $\nu \exp(-\Delta E/k_B T)$, where ν is the attempt frequency, ΔE the activation barrier, k_B the Boltzmann constant, and T the temperature.

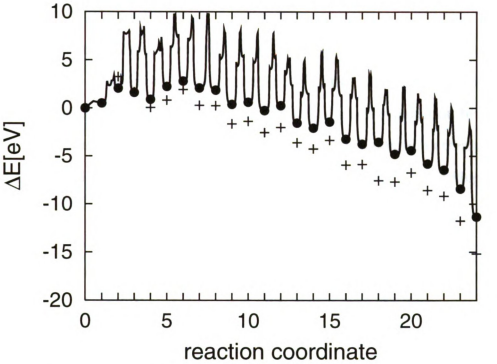

Figure 4.3: Energetics of the fullerene fusion in peapods. (a) Energy change along the optimum reaction path, given by the solid line. Energy results for the 25 intermediate structures, shown in Fig. 4.2, based on my total energy functional (•), are compared to *ab initio* Density Functional results (+). The contiguous minimum energy path in configurational space was identified using a 'string' technique.

fullerenes at constant equilibrium distance (structure "0" in Fig. 4.2), which are freely rotating in space. The 8-dimensional configurational space, spanned by the three Euler angles defining the orientation of each fullerene and the two-dimensional vector defining the orientation of the inter-fullerene connection, is explored uniformly by the rotating fullerenes. Next, I assume that the difference between a "correct" and an "incorrect" fullerene alignment corresponds to a misorientation exceeding $\Delta\varphi \gtrsim 1°$ in any dimension, which naturally introduces a grain size for the discretized configurational space.

In view of the fact that each fullerene has thirty double bonds, each of which can have two orientations, 3,600 out of 3×10^{19} cells in this space represent favorable configurations. Assuming that the configurational space exploration by the freely rotating fullerenes occurs at random in-between two cycloaddition attempts, separated by the period of the inter-fullerene vibration, the probability of finding an optimum configuration is $\approx 10^{-14}$. Using $\nu = 7\times10^{12}$ Hz for the inter-fullerene vibration frequency [85], the $(2+2)$ cycloaddition step with an activation barrier $\Delta E = 0.725$ eV should occur on the time scale of one week at $1,100°$C, significantly longer than the time frame of a GSW transformation. Thus, this step should be rate limiting in a close-packed three-dimensional C_{60} system, which – while molten at this temperature – could be prevented from evaporation by external pressure.

Restricting the configurational space to one dimension, which occurs when chains of fullerenes are packed in peapods, increases the fusion probability substantially. The crucial role played by the enclosing nanotube is to keep adjacent fullerenes in place long enough for them to probe the configurational space at close range. Since the vector connecting adjacent fullerenes coincides with the nanotube axis, the possibility of non-central collisions is eliminated, the dimensionality of the configurational space is reduced to six, and the number of discrete cells to only 5×10^{14}. This increases the probability of the optimum fullerene orientation by five orders of magnitude, and

reduces the reaction time of the $(2+2)$ cycloaddition step to only 7 s at $1,100°C$. I conclude that fusion should occur more easily, when fullerenes are packed in peapods, than in three-dimensional bulk C_{60}.

In a three-dimensional C_{60} system, the fusion rate should further be reduced due to the fact that more than one GSW transformation involving the same fullerene may occur simultaneously. Each C_{60} molecule has initially the ability to form at least four initial connections with neighboring fullerenes by the $(2+2)$ cycloaddition reaction [81]. Considering the finite size of the C_{60} molecule, GSW transformations associated with one fusion reaction are likely to interfere with transformation necessary for a separate fusion reaction, occurring concurrently. Due to resulting frustration, the activation barriers of individual GSW transformations could increase significantly, possibly even stopping the fusion. Since this effect is less severe in lower dimensions, the reduction of the overall fusion rate associated with concurring binary fusion reactions should be much less important in one-dimensional peapods than in bulk C_{60}.

4.4 Summary

In summary, I studied the energetics and the fusion mechanism of fullerenes encapsulated in nanotubes. I found that insertion of a fullerene inside an optimum nanotube host is associated with an energy gain of $\approx$0.4 eV. The "capillary" force produced by the entering fullerene gives rise to a static pressure inside the nanotube. This pressure is expected to increase due to collisions between fullerenes and reach GPa magnitude under experimental conditions. I investigated the energetically most favorable pathway for fusion of two isolated C_{60} molecules inside a $(10,10)$ nanotube. Using a graphical search program, I identified the shortest fusion pathway as a sequence of only 23 generalized Stone-Wales transformations, which can be viewed as

bond-rotations, involving relatively low activation barriers.

Chapter 5

Defective Structures and Defect-Induced Structural Transformations

The following discussion of defective carbon nanostructures and defect-induced transformations follows that presented in References [90, 91, 92, 93].

5.1 Introduction

When structurally perfect, carbon nanostructures are very stable even under extreme conditions. Specific structural defects offer an unusual, energetically accessible path to an inter-conversion between different isomers. More complex systems follow a hierarchical self-assembly formation process.

In recent years, following the discovery of the C_{60} "buckyball" [94], a plethora of nanostructures attracted the attention of carbon scientists. Examples of these intriguing systems are other fullerenes, onions [95], nanotubes [11], and hybrid structures such as peapods [57]. Whereas most of these sp^2 bonded structures are known to grow from carbon vapor under extreme conditions, systems like multi-wall nanocap-

sules may form by activated bond rearrangement from ultra-disperse diamond [17]. All fullerene-based nanostructures show an amazing mechanical strength, chemical inertness, and often an unusually low content of atomic defects.

What appears to be common to all these structures are synthesis conditions that involve extremely high temperatures of close to (or beyond) 1,000°C. While showing no signs of spontaneous decay at room temperature, all fullerene-derived structures are less stable than bulk graphite. Small variations in synthesis conditions, such as change of temperature or partial pressure of the cooling inert gas, appear to have an unusually large effect on the morphology of the product. Obviously, all these structures are formed under non-equilibrium conditions, which are characterized by a competition between the gain in free energy (which contains a significant amount of vibrational entropy) and the fast synthesis kinetics. Due to the fast dynamics of bond formation and fragmentation under the extreme synthesis conditions, only limited information can be extracted experimentally about the nature of the microscopic processes which occur while these structures are formed. Simulations and theoretical modeling of the self-assembly process may play a key role not only in the understanding of nanostructure formation, but also in optimizing synthesis conditions to form particular nanostructures.

This Chapter addresses the physical properties of some of these nanostructures, in particular their stability. It will be shown how macroscopic concepts from elasticity theory translate down to the nanometer scale, where they provide quantitative predictions for the relative stability of nanotubes, scrolls, fullerenes, and peapods. With the help of *ab initio* total energy and molecular dynamics calculations, it is now possible to study the formation and inter-conversion mechanism of unusual systems, such as carbon foam [91] or peapods [56].

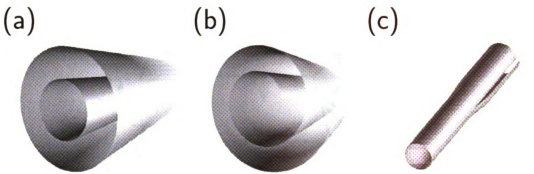

Figure 5.1: Schematic view of (a) a nested multi-wall nanotube, (b) a scroll , and (c) a defect separating the two morphologies within one tube.

5.2 Defect engineering in nanostructures

In fullerenes, the Stone-Wales transformation has been shown to assist efficiently in the ejection of C_2 molecules, thus shrink-wrapping the fullerenes. In nanotubes, Stone-Wales defects are associated with deformations. As described in the following, still other defects may be involved in transforming defective nanotubes, which may contain scroll segments, into defect-free nanostructures. It is conceivable that insertion of particular defects may even be used in the deterministic construction process of carbon nanostructures, such as nanotubes with a particular chirality. A particular type of defect, illustrated in Figure 5.1(c), may be involved in transforming a scroll [Figure 5.1(b)] into a more stable multi-wall system of nested cylinders [Figure 5.1(a)] by a "zipper-like" bond rearrangement transformation, which will be discussed later in this Chapter.

5.3 Carbon nanofoam

A three-dimensional periodic arrangement of the type of defects depicted in Figure 5.1(c) may result in a new crystalline structure, which has been discussed extensively in Reference [91]. Initially a hybrid connecting sp^2 and sp^3 carbon atoms, the

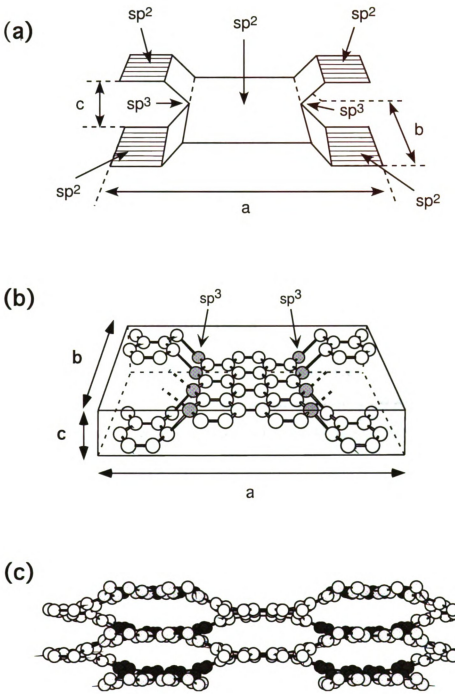

Figure 5.2: Structural description of carbon foam. (a) Schematic illustrating the structural relationship between carbon foam and layered graphite. (b) Conventional orthorhombic unit cell of carbon foam, holding 64 atoms. Unit cell variations are possible by changing the number of carbon atoms along the a and b axes. Initially fourfold coordinated "sp^3" atoms are grey shaded, and the initial bond direction to their fourth neighbors is indicated by the dashed lines. (c) Perspective view of the 3D foam lattice structure, based on the above unit cell.

unusual "foam" structure shown in Figure 5.2 combines a large active surface area, associated with graphite layers, with the structural rigidity of the diamond lattice. The "origami-style" folding process, depicted in Figure 5.2(a), illustrates the close relationship between this structure and graphite. Quite intriguing is the fact that by changing the terrace size a, the foam covers the phase space between layered graphite and cubic diamond, the most stable carbon allotropes. While changing the size of the pores, the system maintains a metallic character [91].

5.4 Hybrid structures of coexisting scrolls and multi-wall nanotubes

Visual inspection of a large number of high-resolution electron microscopy transmission (HRTEM) images of multi-wall carbon nanotubes (MWCNTs)clearly illustrates that these materials have an unexpected intriguing internal structure fraught with numerous defects. [90] It is believed that the chaotic environment associated with evaporation of graphite electrodes in an arc leads to these complex structures. Here I discuss the structure of a hybrid MWCNT composed of scrolled and nested segments, with the respective features typically separated from each other by defects such as edge dislocations, depicted in Figure 5.3. Within the nested tubes, helicity changes little from layer to layer and depends only on layer diameter. Experimental findings [90] suggest the formation of MWCNTs that involves the formation of a scroll of a given helicity which converts, assisted by defects, into the thermodynamically more stable multi-wall structure composed of nested cylinders.

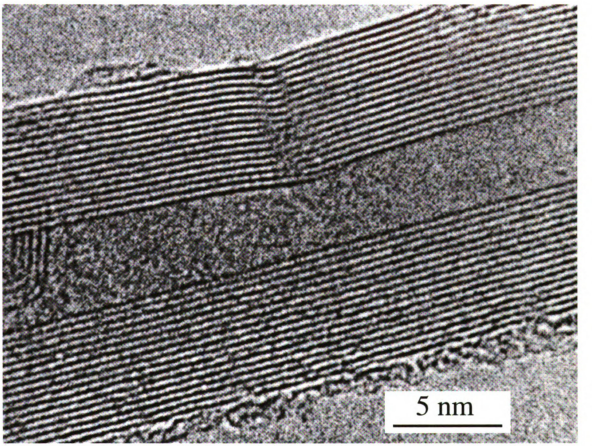

Figure 5.3: High-Resolution Transmission Electron Micrograph of a multi wall carbon nanotube with a slip-plane defect and irregular layer spacing. (from Reference [90])

5.5 Stability differences and conversion mechanism between nanotubes and scrolls

Combining atomic-scale perfection with a nanometer-size diameter and millimeter-size length, carbon nanotubes [11, 1] are considered important pioneers of nanotechnology. These narrow graphitic cylinders with tunable electronic properties[24, 25, 26] are being considered as functional building blocks of nanoscale devices. An important challenge in nanotechnology will be to connect these substructures to more complex systems by directed hierarchical self-assembly, using bond rearrangements as an atomic-scale counterpart of welding.

When observed in the High Resolution Transmission Electron Microscopy (HRTEM) images of carbon arc-discharge deposits [11], the symmetric, evenly spaced line patterns have been interpreted as images of coaxial, nested graphitic tubules. Alternatively, the same images have been attributed to graphitic scroll structures [96]. Since a distinction between the two appears to be impossible based on electron micrographs alone [97], the scroll-tube controversy needs to be settled by different means. The unusual high stability and oxidation resistance of nanotubes seems to exclude scrolls as candidate structures due to their long exposed edge [11]. Presence of scrolls, on the other hand, was conjectured from the unusually large thermal expansion in the radial direction [98] and the relative ease to intercalate metals in these multi-walled structures[99, 100, 101]. Both scrolls and tubes have been observed in HRTEM images of the much larger tubules of vanadium oxide [102], which show a layered structure similar to graphite. Also, dark-field transmission electron diffraction contrast images [103, 104, 105] and x-ray diffraction data [106] of tubular graphitic structures have been taken as indications for scrolls radially embedded within nested cylinders. More recent HRTEM observations even suggest the coexistence of axial scroll and multi-wall segments within the same tubular structure [90]. This observa-

tion introduces two intriguing problems, namely the detailed morphology within the coexistence region, and the possibility of a scroll-to-tube conversion.

Here I present the first study of the relative stability and the microscopic interconversion mechanism between nested graphitic cylinders and scrolls. I show that scroll segments, consisting of rolled-up graphene sheets, may coexist with nested tube segments within a contiguous tubular nanostructure. I propose a concerted bond rearrangement mechanism that avoids bond breaking and results in an axial zipper-like motion of the scroll/tube dislocation. The energy cost associated with creating this dislocation is low enough to form scroll/nanotube junctions at temperatures occurring during nanotube synthesis. The activation barrier for the subsequent scroll-to-nanotube transformation is sufficiently low to enable conversion even at room temperature.

Available experimental data suggest that nested tubes and scrolls only coexist in structures with very many walls [90]. Due to their large size and lack of periodicity, these systems pose an awesome computational challenge. The most suitable formalism to describe accurately the relative energies of large, defect-free tube or scroll segments is based on continuum elasticity theory [107, 108, 109]. This approach proved to be accurate in comparison to *ab initio* total energy calculations for selected single-wall nanotubes [108, 109], and also offers intuitive insight into the origin of structural changes. The major limitation of the continuum approach is its inability to deal with atomic defects. For accurate structural and energy information about defective structures, including coexisting scrolls and tubes, I combine the continuum approach with atomistic calculations.

5.6 Continuum energy functional for sp^2 bonded carbon systems

It has been shown that deformation energies of sp^2 bonded carbon nanostructures are described more accurately by Continuum Elasticity Theory, which ignores discrete atomic positions, than by parametrized bond-order potentials.[107, 108] The continuum energy functional, which describes defect-free single- and multi-wall tubes as well as scrolls, contains the strain energy ΔE_s, the interwall interaction ΔE_{iw}, and an energy term ΔE_e associated with the creation of an exposed edge in scrolls. In order to avoid energy terms associated with tube ends, I only consider infinitely long structures. I only compare structures with the same total area $A = WL$, where W is the nominal width and L the length of a rectangular graphene layer taken as a reference. This reference system has no unsaturated edges and the same number of atoms as the sp^2 bonded tubular structures.

The strain energy, caused by deforming a graphene monolayer into a cylinder of local radius R, depicted in Figure 5.4(a), is given by $\Delta E_s = \epsilon_{cyl} L/R$, where L is the length of the tubular structure. *Ab initio* calculations for single-wall tubes suggest a value of $\epsilon_{cyl} = 4.43$ eV, related to the flexural rigidity of a graphene monolayer [108]. Since strain energy favors geometries with minimum curvature, it must be compensated by other energy terms to stabilize tubular structures. In multi-walled systems, this compensating energy is provided by the attractive inter-layer interaction $\Delta E_{iw} = \epsilon_i A_c$, where A_c is the contact area between sp^2 bonded layers[1]. Since the inter-wall separation of $\Delta R = 0.34$ nm is common to multi-wall tubes, scrolls and graphite, I use $\epsilon_i = 2.48$ eV/nm^2, based on the interlayer interaction in bulk graphite. In scrolls, I also need to consider the energy penalty associated with creating an

[1] I note that the contact area $A_c = A - \pi(R_{in} + R_{out})L$ is smaller than the total area A, since the innermost and outermost walls with the respective radii R_{in} and R_{out} have only one neighboring layer.

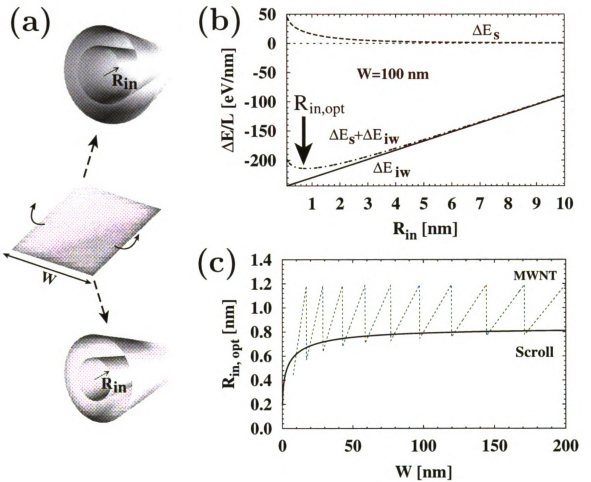

Figure 5.4: (a) Schematic of the transformation from a planar graphene strip of width W to a scroll and a multi-wall nanotube. (b) Dependence of the strain energy ΔE_s and the inter-wall interaction energy ΔE_{iw} on the interior radius R_{in} of a scroll, formed from a $W = 100$ nm wide reference strip. The optimum value of $R_{in,opt}$ results from a compromise between reducing strain and maximizing the inter-layer attraction. The dashed zero line indicates the energy of the reference structure. (c) Dependence of the optimum interior radius of a scroll (solid line) and a multi-wall nanotube (dashed line) on W. Abrupt changes of $R_{in,opt}$ occur in multi-wall structures, when the optimum number of walls changes.

exposed edge, given by $\Delta E_e = \epsilon_e L$. I use $\epsilon_e = 21$ eV/nm as an average value for graphite [110], thus ignoring the small difference between a zigzag and an armchair edge.

In tubular systems, all these energy terms are proportional to the tube length L. For a multi-wall nanotube, the energy per unit length is given by

$$\frac{E_{tube}}{L} = \epsilon_{cyl} \sum_n \left(\frac{1}{R_{in} + (n-1)\Delta R} \right) - \epsilon_i [W - \pi(R_{in} + R_{out})] \,, \tag{5.1}$$

with the summation extending over the nested walls.

The corresponding expression for a scroll is obtained by replacing the summation by an integral over the deformed layer, augmented by the energy penalty associated with the exposed edge. I use the angle θ in cylindrical coordinates as a convenient integration variable, yielding

$$\frac{\Delta E_s}{L} = \frac{\epsilon_{cyl}}{2\pi} \int_0^{\theta_{max}} \frac{1}{R(\theta)} d\theta \,, \tag{5.2}$$

where $R(\theta) = R_{in} + \theta \Delta R / 2\pi$ is the local radius of curvature, and θ_{max} is determined by the initial width W of the reference layer. Combining this strain energy with the other remaining terms leads to a scroll energy per unit length of

$$\frac{E_{scroll}}{L} = \frac{\epsilon_{cyl}}{\Delta R} \ln \left(\frac{R_{out}}{R_{in}} \right) - \epsilon_i [W - \pi(R_{in} + R_{out})] + 2\epsilon_e \,. \tag{5.3}$$

The last term is the exposed edge penalty, which does not depend on the width W of the reference layer and becomes negligibly small in comparison to the other terms in multi-wall systems. I note that providing W and R_{in} defines uniquely the structure of the system, including the number of walls.

Since the edge energy does not depend on R_{in}, I only need to consider the strain and the inter-wall energy when optimizing the scroll structure. The dependence of

$\Delta E_s/L$ and $\Delta E_{iw}/L$ on the interior radius is shown in Figure 5.4(b) for a fixed width $W = 100$ nm of the reference layer. I find that the strain energy ΔE_s decreases with increasing interior radius and asymptotically approaches the zero value of the planar reference layer. Increasing R_{in} for a fixed value of W, on the other hand, reduces the number of walls and the attractive inter-wall interaction ΔE_{iw}. The sum of these energies, given by the dash-dotted line in Figure 5.4(b), shows a shallow minimum at the optimum value $R_{in,opt}$ of the interior radius. This fact suggests that small deviations from the equilibrium structure cost very little energy and are within the reach of thermal processes.

5.7 Optimum geometries and energies of sp^2 carbon nanostructures

In Figure 5.4(c), I display the dependence of the optimum interior radius on the reference layer width. In scrolls, represented by the solid line, I find that R_{in} increases monotonically with increasing W. The optimum value of R_{in} tends to minimize strain while maximizing the inter-wall attraction, and slowly approaches $R_{in,opt} \approx 0.9$ nm. The saturation behavior of $R_{in,opt}(W)$, seen in Figure 5.4(c), results from the fact that an increase of R_{in} beyond a certain value should have little effect on the strain energy, but would significantly reduce the inter-wall attraction. Thus, an important confirmation of my picture is the observation that most multiwall structures have large interior diameters close to 1.8 nm. Multi-wall tubes follow a similar general trend as scrolls with the exception that the optimum number of walls changes abruptly. Such changes occur whenever the width exceeds certain threshold values W_n, where the strain energy sacrifice associated with more walls of smaller radius is compensated by the increased interwall attraction.

My energy results for optimized multi-wall tubes and scrolls are summarized

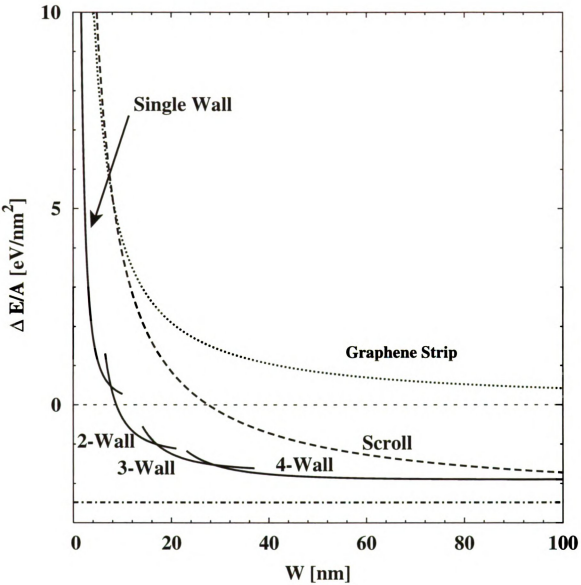

Figure 5.5: Total energy of multi-wall tubes and scrolls with respect to a reference graphene strip of the same length and the width W. For sufficiently large values of W, tubular structures are preferred to the planar graphene strip and approach the energy of bulk graphite. The higher stability of multi-wall tubes over scrolls results from the absence of exposed edges.

in Figure 5.5. All energies are given per area and referred to an infinite graphene layer, shown as the dashed line at $\Delta E/A = 0$. Bulk graphite, the most stable carbon allotrope, is stabilized by the inter-layer interaction with respect to the monolayer and represented by the horizontal dash-dotted line. The energy of a graphene strip, given by the dotted line, is dominated by the exposed edge penalty, when the width W is small. At very small values of W, cylindrical deformation of the strip is energetically prohibitive. Only for wide enough strips, the inter-wall attraction may outweigh the strain energy, stabilizing the scroll with respect to a planar structure. According to Figure 5.5, the narrowest scroll may form when $W \approx 8.4$ nm. For $W \geq 28$ nm, the stabilizing inter-wall interaction outweighs even the exposed edge energy and the scroll becomes more stable than the infinite reference layer.

Due to the absence of the exposed edge energy penalty, I always can find tubes with one or multiple walls that are more stable than a scroll, as seen in Figure 5.5. Since the relative importance of the exposed edge decreases with increasing W, I find the energy difference between multi-wall tubes and scrolls to decrease rapidly with increasing number of walls. In very large multi-wall structures, I postulate that scroll and nanotube segments may even coexist. I also identify a stepwise conversion mechanism of scroll segments into more stable multi-wall nanotube segments.

5.8 Scroll/tube dislocation

A possible way to connect a scroll with a nanotube within a contiguous structure is shown schematically in Figure 5.6(a). In this origami-style counterpart of the system, the tube segment is separated from the scroll by a dislocation region, formed by axially cutting and reconnecting adjacent layers. Obviously, the local morphology, depicted in Figure 5.6(b), can be extended to any number of walls. By axially displacing the dislocation in the direction of the arrow in Figure 5.6(b), a scroll can be

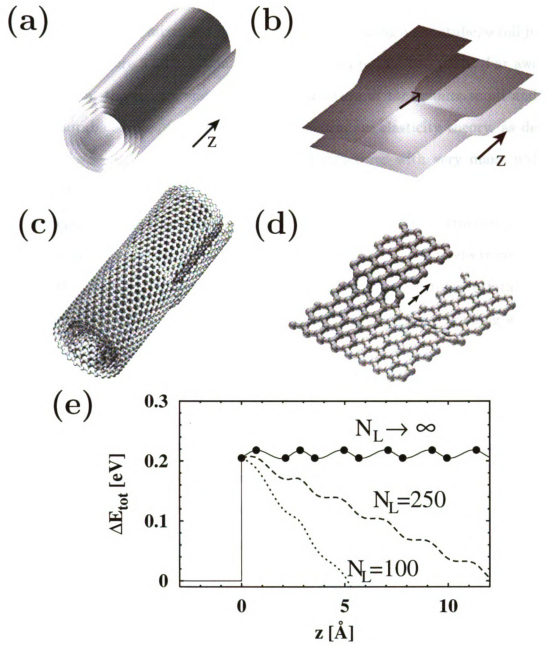

Figure 5.6: (a) A hybrid multi-wall structure with scroll and multi-wall tube segments, shown from the tube end. (b) The detailed structure of two adjacent layers close to the dislocation core near the nanotube/scroll junction. The axial dislocation motion is indicated by the arrow. (c) Equilibrium structure of three innermost walls within an optimized multi-wall system. (d) Atomic structure within the unit cell of an infinite periodic stack of dislocations. The zipper-like propagation of the dislocation along the tube axis z is indicated by the arrow. (e) Total energy change ΔE_{tot} per graphitic layer during the zipper-like scroll-to-tube conversion within the hybrid structure. $z > 0$ denotes the axial position of the dislocation, and $z < 0$ corresponds to a dislocation-free structure.

gradually converted to a multi-wall nanotube.

To globally optimize the infinite structure containing a nanotube/scroll junction, depicted in Figure 5.6(c), I separate the total energy into two parts. Far away from the junction, the energy and equilibrium structure of the infinite scroll and multi-wall nanotube segments is determined by continuum elasticity theory, as described above. As seen in Figure 5.4(c), optimized structures with very many walls have nearly identical innermost and outermost radii and can be joined smoothly with the exception of the dislocation region. To optimize the atomic structure in the finite region near the junction, shown in Figure 5.6(d), I make use of an electronic structure calculation, based on the parametrized linear combination of atomic orbitals (LCAO) formalism [42], which has been used successfully to describe rebonding and growth at the edge of multi-wall nanotubes [49].

Junctions of multi-wall nanotubes with scrolls, depicted in Figures 5.6(a) and (c), contain the type of dislocations, represented in Figures 5.6(b) and (d), in each layer. The total strain is minimized when the dislocation line is shortest, corresponding to radially stacked dislocations in a tubular structure. In systems with very many walls, where scroll/nanotube coexistence has been observed [90], the average local curvature is small. The optimum geometry and strain energy in a radial stack of tube dislocations is represented well by a periodic stack of defects connecting graphitic layers, illustrated in Figure 5.6(b), with the atomic structure of the unit cell depicted in Figure 5.6(d). Such an infinite periodic stack of dislocations is formed by rigidly connecting layers without introducing dangling bonds, in analogy to graphitic 'foam' [91]. Prior to relaxation, each layer in the defect region contains two fourfold coordinated, sp^3 bonded atoms. My results suggest that formation of this defect requires an energy investment of only $\approx$0.2 eV per layer in a structure consisting of infinitely many infinitely large layers[2]. Thus, nanotube/scroll hybrids may form under synthesis

[2]To avoid edge effects, my calculation has been performed using periodic boundary conditions and finite unit cells. Constraints, imposed by the boundary conditions, increase the value of the

conditions, which typically involve high temperatures close to 1000 K.

5.9 Proposed zipper-like scroll-to-tube transformation

The zipper-like scroll-to-nanotube transformation is achieved by displacing the dislocation region in the direction of the arrows in Figs. 5.6(b) and (d). Displacing the dislocation core by one unit cell of the sp^2 structure yields a morphologically identical system with the same energy, provided the structure is periodic in all directions. Only when the number of layers N_L is finite and the energy of the exposed edges in the scroll segment can not be neglected, does the total energy per layer change by $\partial(E_{tot}(z)/N_L)/\partial z = 2\epsilon_e/N_L = (42\ \text{eV/nm})/N_L$ due to the axial dislocation motion. The associated energy gain is the driving force for the scroll-to-nanotube conversion.

In order to determine possible activation barriers that would hinder the zipper motion, I calculated the energy associated with the concerted bond rearrangement, involving an sp^2/sp^3 rehybridization, using the atomistic approach. The total energy per layer in an infinite stack of graphitic layers is displayed in Fig. 5.6(e) as a function of the axial position z of the dislocation, where $z < 0$ corresponds to a defect-free graphitic structure. In structures with a finite number of layers, the z dependence of $\partial E_{tot}/N_L$ at $z > 0$ acquires an additional gradient due to the average energy gain per layer associated with the elimination of exposed edges.

My results in Fig. 5.6(e) indicate that the activation barrier associated with axially displacing the dislocation region by one unit cell is surprisingly small, namely only $\lesssim$0.02 eV. In scrolls with N_L layers and exposed edges, this activation barrier is

apparent dislocation energy for small unit cell sizes. In my calculations, I enlarged the unit cell size beyond that depicted in Fig. 5.6(d), until reaching convergence for the structure within the dislocation region and the value of the dislocation energy. I found my results to agree with *ab initio* results for moderate unit cell sizes, which are accessible to first-principles calculations.

further reduced due to the gradient of $\partial(E_{tot}(z)/N_L)/\partial z$. In systems with less than hundred walls, the gradient is sufficiently large to make the scroll-to-tube conversion activation free. Since the activation barrier is so small in any multi-wall system, I expect the zipper-like scroll-to-tube transformation to occur efficiently even at room temperature. Only much higher activation barriers, possibly associated with defects or impurities, could stop the scroll-to-tube conversion in a transition state [90].

5.10 Summary

In summary, using total energy calculations, I investigated the relative stability of various sp^2 bonded structures, including graphitic scrolls and multi-wall nanotubes. My structure optimization studies have shown that a tubular shape with many walls is favored for very large systems. Such structures should share a similar interior diameter approaching 1.8 nm, in agreement with electron microscopy observations. I found that segments of nested multi-wall nanotubes may coexist with scrolls within the same tubular nanostructure, separated by a dislocation region. The low energy cost to create this defect suggests that hybrid multi-wall structures should likely form under common synthesis conditions. I proposed a concerted bond-rearrangement mechanism that would displace the dislocation axially, like a zipper, thus converting the less stable scroll into a multi-wall nanotube. Due to the low energy cost of the bond rearrangement, I find that the scroll-to-nanotube conversion may proceed even at room temperature.

Chapter 6

Self Healing in Nanostructured Materials

The following discussion of the defect tolerance of carbon nanotubes under extreme thermal and electronic excitations follows that presented in References [111, 112].

6.1 Introduction

The continuing trend towards miniaturization, rapidly approaching the atomic scale [113], raises serious concerns about the required degree of perfection and defect tolerance of nanoscale devices. Carbon nanotubes [11], considered as functional building blocks [114] of such devices, can sustain very large current densities [114, 115] of 10^9 A/cm^2, and show an unusually high thermal and mechanical stability [1]. Nanotube-based transistors out-perform state-of-the-art silicon-based elements in terms of speed, on/off ratio, and the maximum current [115, 116].

However, substantial defect densities in currently available nanotubes raise a concern about the performance and reliability of nanotube-based devices. Theoretical studies showed that even individual vacancies change transport properties of these

quasi one-dimensional systems significantly [117, 118]. At particular bias voltages, drastic conductance reduction in nanotubes results from perturbing the π electron system and from the presence of dangling bonds [118]. Another point of concern is, whether defects may trigger failure earlier in nanoscale-devices than in current Si-based devices. This concern is based on the fact that a 'ten-nine' purity requirement is currently being placed on silicon wafers in order to avoid device failure, which appears to be initiated by processes occurring at defect sites [119, 120]. So far, little is known about possible microscopic processes that could lead to failure of defective nanotubes.

Here I study the defect tolerance of nanotube components by monitoring the behavior of carbon nanotubes with atomic vacancies under electronic excitations and at elevated temperatures. Since nanostructures appear to be more susceptible to defects than bulk systems, I intuitively expect them to fail earlier. The major result of my theoretical study attests to the contrary. Rather than showing signs of premature failure, I find that nanotubes exhibit a unique self-healing mechanism, associated with a new bond formation near the vacancy. Such a self-healing process does not occur in submicron-scale Si-based devices, and is intimately linked to the nanometer size of my system.

The atomic-scale processes associated with failure, which occur in the vicinity of defects on the sub-picosecond to picosecond time scale, are very hard to track experimentally. As a viable alternative, I performed molecular dynamics (MD) simulations of defective carbon nanotubes subject to extreme thermal and electronic excitations.

6.2 Method

To investigate the processes occurring at elevated temperatures, I coupled the defective nanotube to a Nosé-Hoover thermostat [54, 55] and determined the atomic

trajectories using the Linear Combination of Atomic Orbitals (LCAO) total energy functional [42], with parameters based on *ab initio* calculations. This approach has been used successfully to describe bond breaking and forming during the melting process in fullerenes [48].

Describing the response of defective nanotubes to electronic excitations turned out to be particularly challenging, since the study precludes the solution of the time-dependent Schrödinger equation for the time evolution of the electronic wave functions in presence of the ionic motion, caused by the changing charge distribution. This computer intensive calculation has been performed using the time-dependent density functional theory coupled to molecular dynamics (TDDFT-MD) [121, 122].

Since I suspect intrinsically strained narrow nanotubes to be most susceptible to failure, I focus in my study on the $(3, 3)$ nanotube with a monovacancy as a test case. With only 0.4 nm in diameter, this nanotube is one of the narrowest observed [123, 124]. To distinguish nanotube-specific intrinsic behavior from effects caused by the nanotube environment in the experimental situation [124], I focus on an isolated nanotube in vacuum. I use periodic boundary conditions throughout my simulations, also implying a periodic arrangement of vacancies with an axial separation of four to six primitive unit cell sizes of the defect-free nanotube. Consequently, the unit cells used in my calculation hold between 47 and 71 atoms.

6.3 Thermal self-healing

In the first study, addressing a possible device failure due to overheating, I monitor atomic-level processes at elevated temperatures. In my molecular dynamics simulations, I used time steps of 0.5 fs to guarantee energy conservation. I used the relaxed monovacancy structure, depicted in the left panel of Figure 6.1(c), as the starting point. The temperature of the Nosé-Hoover thermostat coupled to the $(3, 3)$

nanotube was increased at 0.75 ps intervals in discrete steps of 400 K. The results of my simulations are discussed in Figure 6.1.

Figure 6.1(a) displays the average total energy per atom as a function of temperature, imposed by the thermostat. To verify the reliability of Nosé-Hoover molecular dynamics results, presented by the data points marked by (•), I compared these data to those obtained using microcanonical molecular dynamics, shown by the data points marked by (×) in Figure 6.1(a). The blue dotted line connecting the data points, provided to guide the untrained eye, suggests the occurrence of a phase transition at a temperature T_M just above 4,000 K, close to the melting temperature of graphite [125] or fullerenes [48]. This relatively high value of T_M comes as surprise, since this narrow nanotube was intuitively expected to melt prematurely, starting at the vacancy site. The slope of the E(T) curve in Figure 6.1(a), representing the specific heat c, has the classical value of $3k_B$ below T_M, indicative of a single phase. Above 4,000 K, I observe a distinct step in E(T), suggesting a phase transition. The transition appears to be gradual in my simulation, which is a consequence of using finite-size unit cells. At temperatures beyond T_M, the specific heat appears to recover its classical value $c = 3k_B$.

In order to understand the microscopic origin of the transition at T_M and the absence of pre-melting near the defect site, I have monitored the distance between the edge atoms adjacent to the vacancy during my simulation. The temperature dependence of the three corresponding interatomic bond lengths d_i is shown in Figure 6.1(b). At selected temperatures, I display the bond length fluctuations by the standard deviations of d_i. Contrary to my anticipation, I observed significant structural changes and re-bonding at the vacancy site, as illustrated in Figure 6.1(c). The final structure, achieved at 4,800 K and depicted in the last panel of Figure 6.1(c), contained two new bonds, emphasized by color and shading. These new bonds formed a bridge across the initial gap and saturated all dangling bonds at the vacancy site,

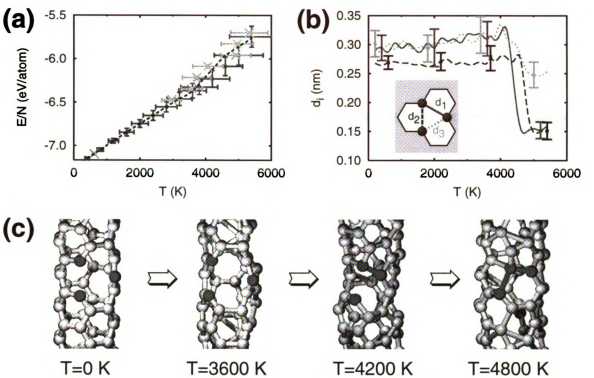

Figure 6.1: Thermal self-healing of a carbon nanotube. (a) Total energy per atom during a molecular dynamics (MD) simulation of the narrow $(3,3)$ nanotube with a single vacancy as a function of temperature. Results based on Nosé-Hoover MD are shown by ($\bullet$) in red, those based on microcanonical molecular dynamics by ($\times$) in green. The blue dashed line, a guide to the eye, indicates a phase transition near $4,000$ K. The standard deviations of energy and temperature of the system are shown by error bars for selected data points. (b) Interatomic distances d_i near the vacancy site as a function of temperature, as defined in the inset. d_1 is shown by the red solid line, d_2 by the blue dashed line, and d_3 by the green dotted line. (c) Snapshots of structures encountered during Nosé-Hoover MD simulations, as the heat bath temperature increases. The three atoms adjacent to the vacancy and the newly forming C-C bonds are emphasized in the figure.

restoring part of the initial structural rigidity. Even more important, this reconstruction is expected to remove the earlier mentioned reduction in the conductance, associated with dangling bonds [118]. My total energy calculations suggested that this transition requires an initial energy investment of 0.3 eV, followed by a net energy gain of up to 1.76 eV per vacancy. Consequently, this reconstruction can be viewed as a thermally activated self-healing process.

6.3.1 Energetics of monatomic vacancies in narrow nanotubes

To understand this energy gain in a broader context, I performed structure optimization on monovacancies in wider $(5,5)$, $(7,7)$, and $(10,10)$ nanotubes. I found the energy gain due to re-bonding near the vacancy to be the largest in the $(3,3)$ nanotube and to decrease with increasing tube diameter. In the more flexible narrow nanotubes, the strain induced by the reconstruction could be accommodated locally at little energy cost. With increasing nanotube diameter, the strain extended over an increasing region, making this reconstruction energetically less favorable. Ultimately, in a graphene monolayer, the energy gain due to the formation of new bonds was not sufficient to compensate for the associated large strain energy due to re-bonding. Thus, the thermally activated self-healing process was found to be intimately linked to the larger flexibility of nanostructures.

6.4 Self-healing by photo-excitations

As mentioned earlier, structural changes may be achieved also by electronic excitations, with no need for thermal activation. I studied the atomic-scale processes following a photo-excitation near a monovacancy in a $(3,3)$ carbon nanotube using *ab initio* TDDFT-MD calculations, based on the local density approximation (LDA) to

the density functional theory (DFT) [126, 127]. Valence electron states were described using Troullier-Martins type pseudopotentials [128] and a plane wave basis with the kinetic energy cutoff of 40 Ry. Due to the large size of the unit cell representing the defective tube, I limited my sampling of the momentum space to the Γ point.

Among the many possible excitations, I selected the particle-hole state with the highest likelihood to destroy the nanotube, by comparing the outward components of Hellmann-Feynman forces near the vacancy. I found this to be the case by promoting an electron from the highest occupied state to the second lowest unoccupied state. The energy of 0.9 eV, associated with this excitation, was determined from the total energy difference between the excited and the ground state in a $(3,3)$ nanotube with a 47-atom unit cell. The subsequent time evolution of the electronic and atomic structure in this Franck-Condon like process was computed within the TDDFT-MD formalism, by maintaining self-consistency between the wave function and potential, which both evolve in time [121, 122].

In the beginning of the simulation, I froze all the atoms in the relaxed ground state geometry and obtained the static solution of the electronically excited state. The ion dynamics induced by this excitation is depicted as a time sequence of geometries in Figure 6.2(a). I found that the vacancy initially started to open in the direction of the Hellmann-Feynman forces. 200 fs after the excitation, two of the three atoms adjacent to the vacancy approached each other sufficiently close to form a new bond. I interpret this new bond formation as a self-healing process, in analogy to the previously discussed behavior at elevated temperatures. The difference with respect to thermal self-healing is the absence of an activation barrier and the extremely short time scale of the photo- induced process. The time evolution of the electronic states during the ionic motion is presented in Figure 6.2(b) as a series of contour maps depicting the norm of the excited electron wavefunction. As time progresses, I find the excited electron distribution to change from an anti-bonding to a dangling bond

characteristics.

I should emphasize that in contrast to conventional *ab initio* MD simulations, I monitor the time evolution of each populated and empty single-electron state during the ionic motion. This approach provides information not only about the charge distribution, but also the lifetime of electronic excitations in presence of ionic motion. An important indication for the onset of a non-adiabatic decay is a sudden increase in the off-diagonal matrix elements of the Kohn-Sham Hamiltonian in the basis of the time-evolving eigenstates. Following a non-adiabatic decay, rapid Rabi oscillations appear in the electronic levels, even if the atomic motion is smooth.

With the charge distribution determined by the time-evolving populated states, forces acting on atoms are determined using the Hellmann-Feynman theorem [121, 122]. This approach offers a significant advantage over the conventional *ab initio* MD simulations, where forces acting on atoms are calculated from static solutions of the Kohn-Sham equations at each time step, presuming the population of each Kohn-Sham state is known. Predicting the correct sequence of populated levels is a challenging undertaking especially in case of level alternation, which occurs in the single-electron spectrum following the photo-excitation of my system, as shown in Figure 6.3. In my system, I found the character of the hole wave function to differ significantly from the valence band character, and the character of the excited electron to also differ from the conduction band states. Thus, the level alternation seen in Figure 6.3 did not cause a non-adiabatic decay of the excitation, and the system remained on the adiabatic potential energy surface during my simulation.

Unlike in bulk systems, where electron-hole excitations typically decay on a femtosecond time scale, I did not find any indication for such a non-adiabatic decay of the excitation in the defective nanotube during my MD simulation, extending over 200 fs. Due to the apparent long lifetime of the electronic excitation, a significant fraction of the ion dynamics occurs on the excited state potential energy surface, which is very

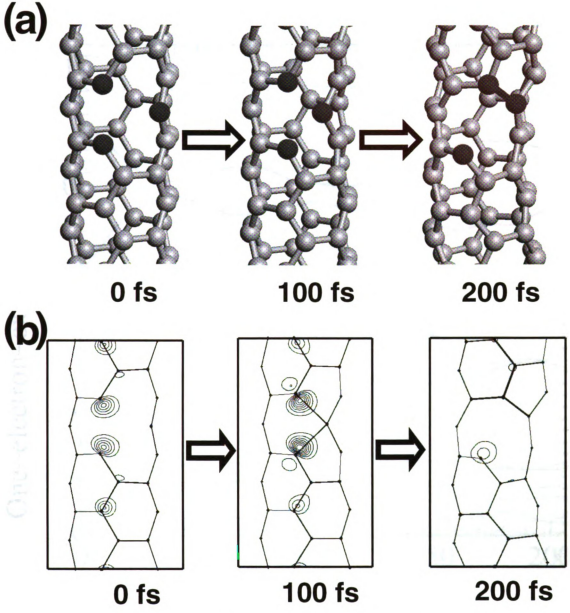

Figure 6.2: Self-healing process within a $(3,3)$ nanotube with a single vacancy, induced by illumination. (a) Time evolution of the geometry. The three atoms adjacent to the vacancy and the new C-C bond, which forms 200 fs after the photo-excitation, are emphasized by color and shading. (b) Time evolution of the excited electron state. The lowest contour lines are common to the three panels.

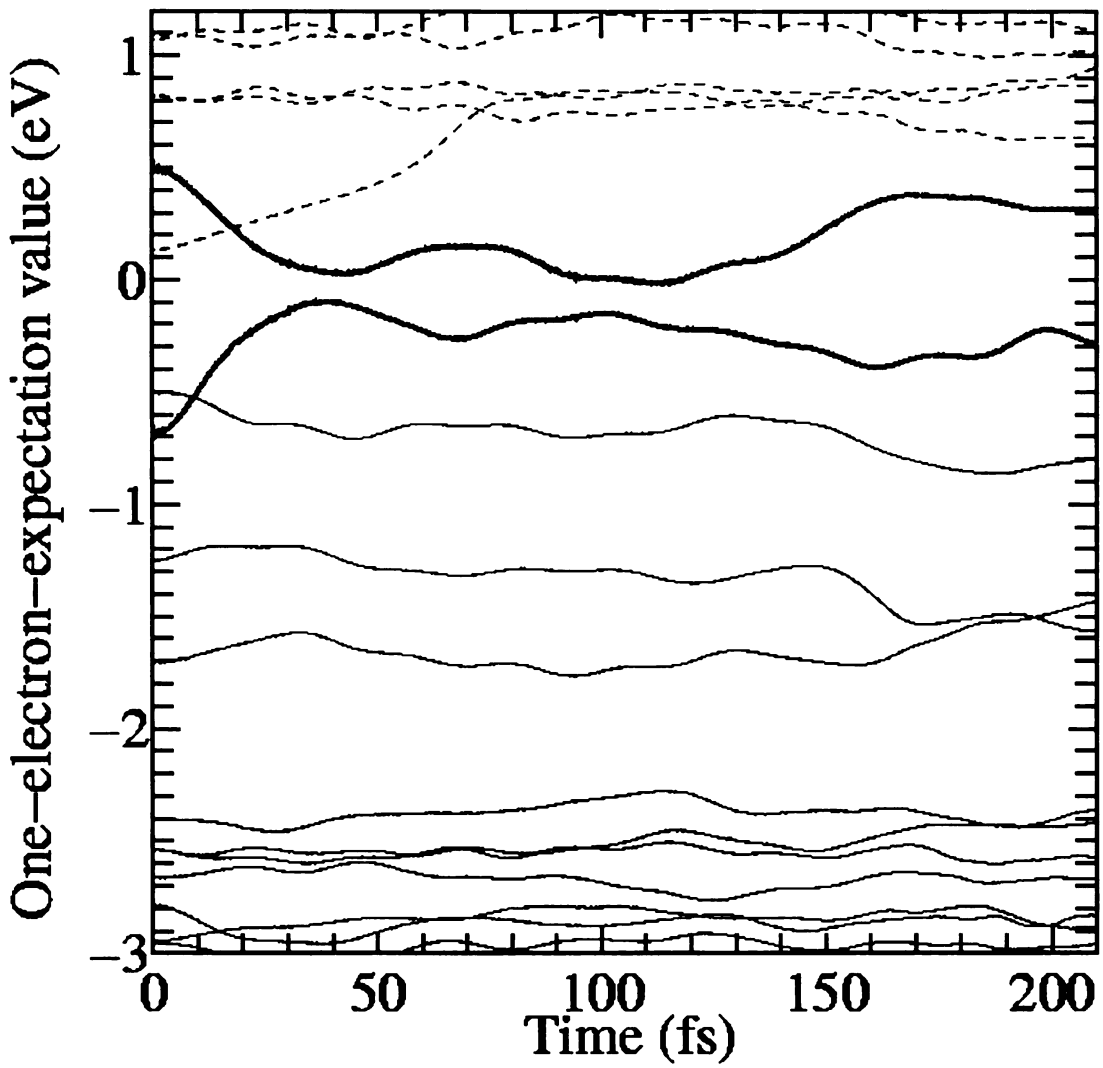

Figure 6.3: Time evolution of the energy spectrum during the atomic motion following the initial photo-excitation. Fully occupied states are denoted by solid black lines, completely empty states by dashed black lines. Time evolution of the electron-hole pair, created by the photo-excitation, is shown by the heavier red solid lines.

different from the ground state potential energy surface. One such difference concerns the activation barrier, which is absent in the photo-excited state, but has a value of 0.3 eV in the electronic ground state. In contrast to the slow, thermally activated self-healing process, occurring in the electronic ground state, I find the photo-induced self-healing process to occur very fast even at low temperatures due to the absence of the activation barrier in the excited state.

6.5 Conclusions

In summary, I performed molecular dynamics simulations of defective nanotubes subject to elevated temperatures and electronic excitations. I have identified a self-healing process of defects, which is intimately linked to the nanometer size of these systems and absent in their bulk counterparts, and bears promise for future nanotube applications. I found that the stability and conductivity of narrow nanotubes with monatomic vacancies should improve following the formation of new bonds among the atoms at the vacancy edge. Self-healing was observed under both thermal and electronic excitations. This process was energetically favorable due to the extra flexibility of nanostructures in response to strain.

I should point out that my simulations correspond to vacuum conditions and that defect-gas interactions cannot be ignored in more realistic situations. I also explored the possibility of healing other imperfections, such as oxygen contamination or Stone-Wales type defects, which may exist in nanotubes. My preliminary results suggest that electronic excitations do not eliminate Stone-Wales defects, but rather induce localized vibrations in their vicinity.

Another type of common defects in carbon nanotubes are Stone-Wales (SW) defects. SW defects in nanotubes can be healed through electromagnetic excitations. A specific wavelength of the electromagnetic spectrum seems to excite resonance

vibrations at SW defect sites. This could be used to determine if there are any SW defects in a sample. Alternatively, it should be possible to determine defect densities simply by doing vibration spectroscopy after exciting the sample with a specific wavelength. This could be a useful alternative to STM imaging in search of SW defects.

Chapter 7

Bonding and Energy Dissipation in a Nanohook Assembly

The following discussion of the nanovelcro assembly of nanoscale hooks based on carbon nanotubes follows that presented in Reference [129].

7.1 Theoretical concept of nanovelcro

Carbon nanotubes [11], consisting of graphite layers rolled up to seamless, nanometer-wide cylinders, are now considered important building blocks for nanotechnology [2]. Their extraordinary mechanical properties, including high stiffness [130, 131, 132] and axial strength [133, 134], are related to the unparalleled tensile strength of graphite [135]. In single-wall nanotubes [22, 23], substitution of hexagons by pentagon-heptagon pairs is known to cause a permanent bend in the tube and to change its chirality [136]. The morphology of a nanotube deformed to a hook is illustrated schematically in Figure 7.1(a). A High-Resolution Transmission Electron Micrograph (HRTEM) of this system [137] is reproduced in Figure 7.1(b), and a Scanning Electron Micrograph (SEM) of nanohooks [138] is shown in Figure 7.1(c). So far, studies of nanotubes containing pentagon-heptagon pairs have concentrated on

their intriguing electronic properties [139, 140].

Here I explore the suitability of nanotubes, permanently deformed to hooks or other non-cylindrical structures, to effectuate bonding between solid surfaces,[1] as a nanometer-scale counterpart of velcro. I study the physical properties, including mechanical strength and resilience, of a micro-fastening system consisting of solid surfaces covered with nano-hooks, illustrated in Figure 7.2(a) and Figure 7.1(c), which is called 'nanovelcro'. By studying the atomic-scale processes during closure and opening, I show that a nanovelcro junction should be ductile rather than brittle, and exhibit large toughness. I find that nanovelcro offers significant advantages over conventional adhesives and welding, including thermal stability to 4,000 K, and a self-repair mechanism under local shear. With a large density of hooks per area, strong bonding can be achieved in parallel to mechanically decoupling the connected parts.

7.2 Theoretical approach

To determine the physical behavior of the nanovelcro micro-fastening system, I combine total energy and structure optimization calculations with molecular dynamics simulations. In order to describe realistically a possible $sp^2 \rightarrow sp^3$ rehybridization during the opening and closing of nanovelcro bonds, I use an electronic Hamiltonian that had been applied successfully to describe the formation of peapods [56], multi-wall nanotubes [49], the dynamics of the "bucky-shuttle" [17], and the melting of fullerenes [48]. Total energies and forces are compared to those based on the Tersoff potential [141] for strained structures that maintain sp^2 bonding. When modeling the dynamical processes during opening and closure of the hook assembly in Figure 7.2(a), I subject the grey-shaded rigid anchor sections to either a constant force or a constant velocity in the desired direction.

[1] *"Micro-Fastening System and Method of Manufacture"*. U.S. Patent Application of D. Tománek, Richard J. Enbody, and Young-Kyun Kwon, filed February 12, 1998.

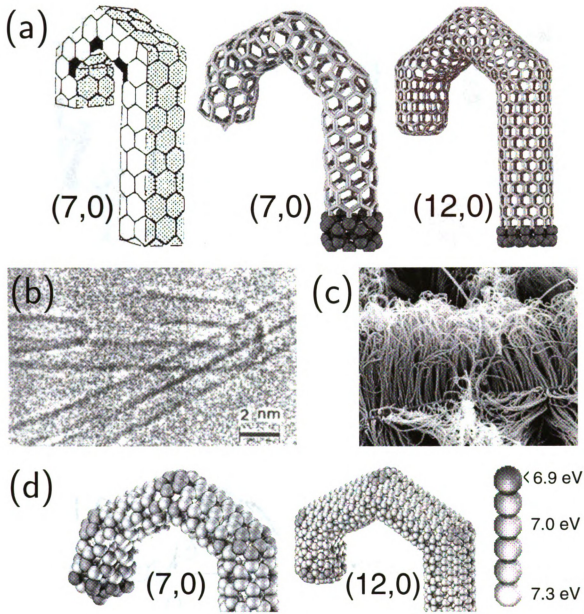

Figure 7.1: Structure of a nanotube-based hook. (a) Schematic view of a hook, formed by inserting pentagon-heptagon pairs in an all-hexagon tubular structure, and the equilibrium structure of hooks based on a (7,0) and a (12,0) nanotube. (b) Transmission Electron Micrograph of a nanotube-based hook, published in Ref. [137]. (c) Scanning Electron Micrograph of an array of nanohooks grown on a surface [138]. (d) Atomic binding energies in (7,0) and (12,0) nanohooks. The grey scale coding reflects the energy scale on the right.

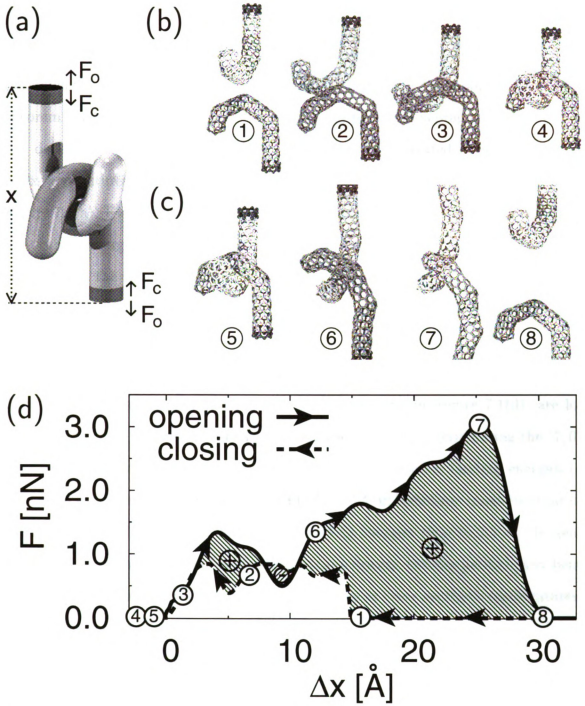

Figure 7.2: (a) Schematic drawing of a two-hook assembly, defining the anchor distance x, the direction of the opening force F_o and the closing force F_c. Snap shots of the $(7,0)$ nanohooks during (b) closure and (c) opening of the nanohook assembly. (d) Force acting on the nanohooks during the opening and closure of the assembly as a function of the relative anchor displacement Δx. The labels correspond to structures depicted in (b) and (c). The grey-shaded area, depicting the hysteresis, represents the energy dissipated during an opening-closing cycle.

7.3 Nanohooks based on carbon nanotubes

As illustrated in Figure 7.1(a), a set of six pentagon–heptagon pairs causes a permanent deformation of a $(7,0)$ single-wall nanotube to a nanohook [137]. Euler's theorem suggests that a hook deformation due to pentagon-heptagon insertion does not depend on the chiral index of the tube. This is illustrated by comparing the relaxed structures of the $(7,0)$ and the wider $(12,0)$ nanotube in the right panel of Figure 7.1(a). Even though substitution of hexagons by pentagon-heptagon pairs in a nanotube is energetically unfavorable, the system is sufficiently flexible to redistribute the strain in the vicinity of the pentagons and heptagons.

To visualize this strain redistribution in the structure, I grey-shaded the spheres representing individual atoms according to their binding energy in Figure 7.1(d). I found all the atomic binding energies to be lower than the 7.4 eV value of graphite. The least stable atoms, indicated by the darkest shading in Figure 7.1(d), are located in the caps. The atomic arrangement at the hemisphere terminating the $(7,0)$ nanotube is similar to the strained C_{24} fullerene, with atomic binding energies of only $\approx$6.4 eV. The cap structure at the end of the $(12,0)$ nanotube resembles that of the more stable C_{84} fullerene, with atomic binding energies close to 7.1 eV. In general, I expect the occurrence of pentagon-heptagon defects, causing permanently bent structures shown in Figures 7.1(b) and (c), primarily at lower synthesis temperatures, where such defects cannot be annealed easily [137, 138].

A pair of mating nanohooks is illustrated schematically in Figure 7.2(a), together with the direction of the opening force F_o and the closing force F_c. The nanohooks are to be considered permanently anchored in the surfaces to be connected. The anchor regions are emphasized by the dark color and separated by the distance x. The forces are given by the gradients for the total energy of the nanohook structure with the exception of the rigid edge regions, emphasized by the dark color in Figures 7.1(a) and 7.2(a)-(c). Snap shots of the $(7,0)$ nanohook engagement process are shown in

Figure 7.2(b). In spite of significant structural deformations during this transition, I found no signs of irreversibility associated with a possible local $sp^2 \rightarrow sp^3$ transition or a permanent structural change, reflecting the resilience of the nanohooks to mechanical deformations.

7.4 Dynamics of opening and closing the nanohook assembly

In my molecular dynamics simulation, I subject the anchor region of the hooks, to a constant velocity $v_c = 25$ m/s, and monitored the force F_c during the closure process. Comparing results for different velocities, I found the force $F_c(x, v_c)$ to depend only on the relative distance x between the anchor regions at low displacement velocities. My results indicate that the value of $F_c(x)$, based on molecular dynamics simulations, agrees with static results based on static structure optimization with constrained anchor regions. At velocities $v_c \geq 75$ m/s I observed an increase in $F_c(x, v_c)$ due to the inertia of the nanostructure. For the sake of convenience, I defined $x = x_0 + \Delta x$, where x_0 is the shortest distance between the anchor regions, at which the substructures started interacting. Numerical results for $F_c(\Delta x)$, displayed by the dashed line in Figure 7.2(d), indicate that closure of the $(7, 0)$ nanohook assembly requires an average force of $< F_c > \approx 0.9$ nN.

The dynamics of the opening process is illustrated by snap shots in Figure 7.2(c). As during the closing process, I subjected the anchor regions of the hooks to a low constant velocity $v_o = 25$ m/s and monitored the force F_o during the opening process. The results, given by the solid line in Figure 7.2(d), indicate an average opening force of $< F_o > \approx 1.7$ nN, about twice the value of the closing force. The opening force increases as the hook becomes stiffer while stretched, and reaches the maximum value of $F_o \approx 3.0$ nN. In spite of this considerable force, I have not observed any irreversible

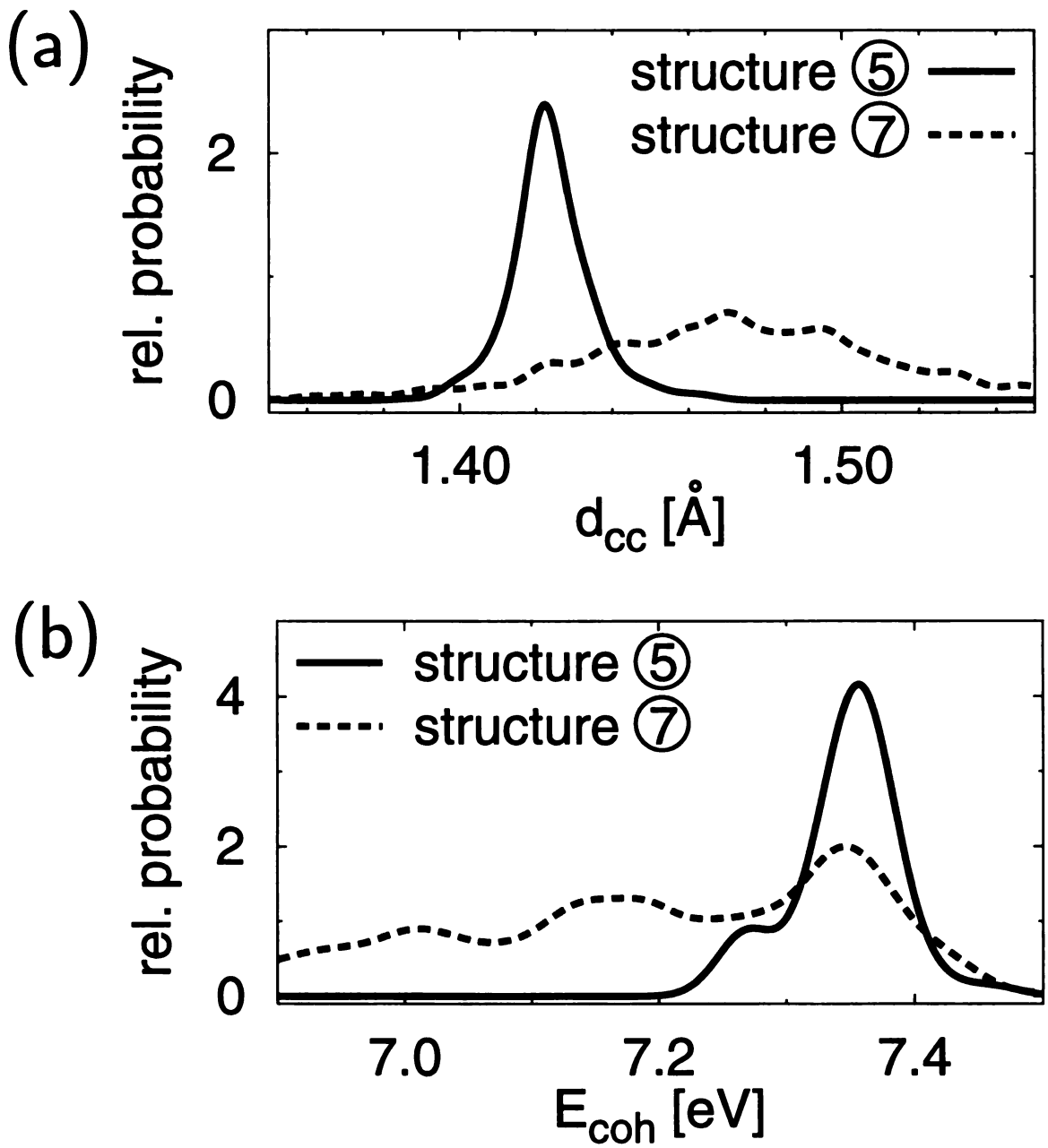

Figure 7.3: Distribution of (a) bond lengths and (b) atomic binding energies in the $(7,0)$ nanohook assembly at different stages of the disengagement process. Results for the unstrained structure ⑤ of Figure 7.2(c), given by the solid line, are compared to those for the strained structure ⑦, given by the dotted line.

structural changes in the nanohook assembly, including the least stable terminating cap. Even in the most strained structure ⑦ in Figure 7.2(c), the closest inter-wall distance between the hook substructures was in excess of 2.1 Å, thus preventing a local $sp^2 \rightarrow sp^3$ rebonding [142].

When exploring the suitability of nanohooks for bonding, I assume that the nanohooks are permanently anchored in the substrate by covalent bonds. These bonds are particularly strong for nanohooks grown on diamond, metals and carbides. Uprooting the hook would require a very high force, possibly comparable to the average force of $\approx$50 nN associated with cleaving the tube axially. The forces needed to open and close the nanovelcro bond are much smaller and will not detach the hook assembly from the anchor points.

To determine which parts of the nanohook assembly are most prone to damage, I plotted the distribution of bond lengths and atomic binding energies during the opening process in Figure 7.3. As seen in Figure 7.3(a), most bond lengths are close to the graphite value $d_{CC} = 1.42$ Å in the initial structure ⑤. The corresponding binding energy distribution in Figure 7.3(b) shows a large peak near 7.3 eV, reflecting the small strain in the nanotube as compared to a graphene monolayer. Only the cap atoms show a much lower binding energy $E_{coh} \approx 6.4$ eV, depicted in Figure 7.1(d). In the strained hook structure ⑦, the distortion is accommodated by a large portion of the system, reflecting the ductility of the bond. In the vicinity of the hook, the average bond length increases by $\approx$0.05 Å and the distribution broadens significantly. This behavior is reflected in the binding energy distribution, which shifts to smaller binding energy values and also broadens considerably. I do not observe new peaks at significantly larger bond lengths or smaller binding energies, which would indicate the onset of a crack. These findings, together with the structural snap shots shown in Figures 7.2(b) and (c), confirm that nanovelcro maintains its structural integrity during repeated opening and closing.

7.4.1 Mechanical characteristics of the nanovelcro bond

My results in Figure 7.2(d) also provide quantitative information about the toughness of the $(7,0)$ nanovelcro bond, defined as the energy needed to open the nanohook assembly. The calculated toughness of $\approx$30 eV is very high, almost twice the energy investment of 15.4 eV to cleave a perfect $(7,0)$ nanotube. The simple reason for this unexpected result is that an average opening force $< F_o > \approx$1.7 nN, acting over a large distance of 30 Å, performs more work than the much higher force of $\approx$50 nN, which cleaves axial bonds across a distance of 0.5 Å. Upon opening, the energy stored in the strained hook structure is deposited into the internal degrees of freedom, heating up the nanostructure locally up to near $1,000$ K. This energy is efficiently carried away due to the excellent thermal conductivity of carbon nanotubes [143], thus preventing irreversible structural changes.

Next, I define the stability of the nanovelcro bond as the energy to close and reopen the nanohook assembly, given by $\Delta E_b = \int_{-\infty}^{\infty} (F_o(x) - F_c(x))\, dx$. I find a large value of $\Delta E_b \approx$24 eV for the stability of the $(7,0)$ nanohook system, corresponding to the shaded area in Figure 7.2(d). The relatively small difference between the toughness and the stability of the bond is due to the low amount of energy required to close the hook, given by the area under the dotted line.

The usefulness of nanovelcro for permanent bonding becomes obvious especially when considering two flat solid surfaces covered by an array of nanohooks. In view of the small nanohook cross-section, We may find up to one nanohook per nm^2, corresponding to an ideal coverage of 10^{18} nanohooks per m^2. Thus, detachment of nanovelcro bonded areas should require an energy investment of $\leq$5 J/m^2. This is significantly more than the energy to cleave most crystals, which is twice their surface energy, and is responsible for the unusual toughness of the nanovelcro bond. In view of the large force required to open a nanohook assembly, the ultimate strength of nanovelcro should approach 3 GPa, more than in most solids. Under tensile load, I

expect the solids to break first, while the nanovelcro bonds remain engaged.

I found that the bonding ability deteriorates with increasing nanotube diameter. In the wider nanohook based on the $(12, 0)$ nanotube, I found that the resilience of the system is reduced by its tendency to collapse upon bending. This particular deficit can be compensated by using multi-wall nanotubes or peapods [57] instead of single-wall systems.

As I did not observe any $sp^2 \rightarrow sp^3$ rebonding during my simulation, I compared my total energies to calculations based on the Tersoff potential [141]. Since this bond-order potential considers nearest-neighbor bonds only, the optimized hook structures were slightly wider and the work associated with their opening and closing turned out to be about 10% lower than in the results presented above.

It is essential to notice that the crucial feature of the nanovelcro bond is not the shape of the deformed nanotubes, but rather the area under the force-displacement hysteresis curve in Figure 7.2(d). Other structures, including coils [144], can be combined with hooks and other deformed tubes for efficient bonding. I expect the bonded area to show good electrical and thermal conductivity, reflecting the intrinsic properties of nanotubes. Conductivity measurements can also be used to monitor the local bonding in real time. A uniform surface coverage by nanohooks can be achieved using Chemical Vapor Deposition of hydrocarbons on catalyst-covered surfaces [145], as seen in Figure 7.1(c). The requirement of a low growth temperature for the formation of hook structures also extends the range of substrates, on which nanovelcro can be grown. The ability of hooks to open and close reversibly results in a unique self-repairing capability. This is of particular interest when bonding solids with different thermal expansion, such as applying a diamond coating to metals, since self-repair should prevent delamination in case of large temperature fluctuations.

7.5 Summary

In conclusion, I combined total energy and molecular dynamics calculations to explore the suitability of nanotube-based hooks for bonding. Hooks, coils, and similar structures form upon inserting pentagon-heptagon pairs in the honeycomb structure of straight carbon nanotubes. I postulated that surfaces covered with an array of hooks, which are covalently anchored in the substrate, can be pressed together and form permanent bonds as a nanoscale counterpart of velcro fasteners. My results indicate that a large force of 3.0 nN is required to disengage two hooks based on a $(7,0)$ carbon nanotube. Performing simulations for $(7,0)$ and $(12,0)$ systems, I found nanohooks to be generally resilient and to keep their structural integrity during the opening and closing process. In view of the high tensile strength of individual nanotubes and the stability of nanotube-substrate bonds, arrays of hooks may connect solids ranging from metals to carbides and diamond with a tough, heat resistant bond. This bonding scheme shows a capability for self-repair that may prevent delamination caused by differential thermal expansion. Nanovelcro bears promise as a micro-fastening system for the next generation of nano-robots and nanometer-scale mechanical and electronic components.

Chapter 8

Crystalline Solids Based on Polymerized C_{60} Molecules

The following discussion of physical properties, in particular rigidity of self-assembled fullerene crystals, follows that presented in Reference [146].

8.1 Introduction

Owing to the fact that the binding energy of carbon atoms in diamond and in graphite is roughly the same, whereas the atomic coordination number in graphite is lower than in diamond, the interatomic sp^2 bonds in graphite are intrinsically stronger than the sp^3 bonds in diamond. Still, diamond is known as the solid with the highest bulk modulus[147] of 443 GPa. Obviously, substantial effort has been invested to harness the toughness of the sp^2 bond in a 3D atomic arrangement with a bulk modulus superior to that of diamond. Only on the nanometer scale, non-planar sp^2 bonded carbon structures including fullerenes[94] and nanotubes[11, 22] show an extraordinary stability and stiffness[148, 130, 131, 132, 133, 134]. The bulk modulus of a single C_{60} molecule is predicted to reach the value of[148] 717 GPa. Nevertheless, this superior stiffness of individual fullerenes is not reflected in the elastic properties

of molecular crystals formed of fullerenes[85], which are soft due to the weak inter-fullerene interaction.

Recent observations suggest that C_{60} fullerenes, which have polymerized into 3D crystals under high pressure and high temperature conditions, surpass diamond in hardness[81, 149, 150]. Some of the polymerized C_{60} crystals have been studied theoretically[151, 152, 153]. Optimized packing within selected finite-size C_{60} aggregates, but not infinite structures, has been suggested based on the comparison between simulated X-ray patterns and experimental data[154, 155]. Theoretical calculations so far have failed to identify any structure with a bulk modulus comparable to the reported experimental data, which would exceed the value of bulk diamond. It has also been pointed out that the experimental methods used to identify the structure of polymerized fullerenes may not be conclusive[156]. The uncertainty regarding the atomic arrangement within super-hard polymerized C_{60} structures requires extensive additional studies.

Previous computational attempts to explore candidate systems for hard polymerized fullerenes were limited to few structures[151, 152, 153], since the rehybridization occurring in fullerene polymers can not be described reliably by analytical bond order potentials, and thus requires more sophisticated, computationally demanding total energy functionals. Due to the large number of degrees of freedom, unconstrained optimization of the atomic coordinates as a function of volume, and thus a reliable determination of the total energy and the bulk modulus is computationally prohibitive with *ab initio* total energy functionals.

Here I calculate the total energy of 12 stable polymerized fullerene phases using an electronic Hamiltonian that had been applied successfully to describe the formation of peapods [56], multi-wall nanotubes [49], the dynamics of the "bucky-shuttle" [17], and the melting of fullerenes [48]. The underlying parameterized total energy functional [42, 8] is efficient enough to explore many structures, providing an adequate

description of total energy changes associated with different bonding geometries. My approach reproduces correctly the observed bulk modulus of cubic diamond. Also, as I discuss below, my results compare favorably with *ab initio* results[151, 152, 153], which have been reported for a limited number of candidate systems. Besides the optimized geometry, I also determine the physical properties of candidate structures for super-hard crystalline materials.

8.1.1 Polymerized fullerenes

Fullerenes such as C_{60} are known to form stable 1D and 2D polymers by the 'cycloaddition' reaction, with 'double bonds' facing each other in adjacent fullerenes [157, 80, 158, 159]. Selected 1D and 2D polymer structures are shown in Fig. 8.1(a), with the nature of the bond depicted in Fig. 8.1(b). The interaction between such low-dimensional polymers in 3D assemblies is generally weak, similar to the inter-layer interaction in graphite. The prerequisite for making bulk structures incompressible is the formation of strong, covalent bonds between these low-dimensional polymers. Such a rehybridization is indeed expected to occur spontaneously under high temperatures and pressures, similar to the conversion of rhombohedral graphite to hexagonal diamond[142].

Due to structural constraints, maximizing the inter-fullerene bonding is not as easy in 3D crystals as it is in one and two dimensions. Polymerization by cycloaddition, shown in Fig. 8.1(b), occurs at moderate temperatures and pressures. Under less favorable conditions, other covalent inter-fullerene bonds may be established, which would increase the number of favorable local bonding geometries and thus improve the degree of covalent bonding in bulk structures. Fullerene polymerization by reactions other than cycloaddition may require high temperature and pressure conditions, similar to those reported in Ref. [81, 149, 150]. In my studies of bulk fullerene polymers I considered alternative inter-fullerene bonds, depicted by the different bonding

schemes in Figs. 8.1(c)-(i), which have been suggested previously[160, 161, 162]. Such strong inter-fullerene bonds have been recently observed to connect fullerenes during their fusion inside carbon nanotubes[57, 60, 68], while subjected to effective high pressure conditions[69].

The bonding schemes between C_{60} molecules, which I consider in the following, are depicted in Figs. 8.1(b)-(i). The most common polymerization involves the 66/66 (2+2) cycloaddition, depicted in Fig. 8.1(b), involving 'double bonds' at common hexagon-hexagon edges in adjacent fullerenes, which face each other. This bonding scheme connects fullerenes to form chain polymers, labeled by C in Fig. 8.1(a), by converting pairs of 'double bonds', facing each other in adjacent fullerenes, to single bonds, and leads to the formation of two new 'single bonds' connecting the fullerenes. Due to their partial sp^3 nature, the new bonds cause a corresponding structural relaxation within the fullerenes. Structures depicted in Figs. 8.1(c)-(e) may be derived from the structure in Fig. 8.1(b) by subsequent bond breaking and bond rotation. Disrupting the two intra-fullerene bonds, involved in the (2+2) cycloaddition, stabilizes the inter-fullerene bonds and partly relieves structural strain, as depicted in Fig. 8.1(c). Due to the smaller number of structural constraints in this double chain (DC) configuration, this structure is less rigid than that in Fig. 8.1(b). In this system, all atoms have 3 neighbors, and all interatomic bonds are sp^2-like. Rotating the inter-fullerene bonds by 90° yields an open hinge (OH) structure with sp^2 bonded bridges, depicted in Fig. 8.1(d). I also note that these structures occur during the stepwise conversion of two C_{60} fullerenes to a C_{120} capsule by generalized Stone-Wales transformations[69, 86].

The open-hinge structure in Fig. 8.1(d) bears promise as a building block in materials with a high bulk modulus, since even its narrowest structural elements are graphene strips with an unusually high tensile strength. Among all the possible lattice geometries based on this bonding type, only one turned out to remain stable

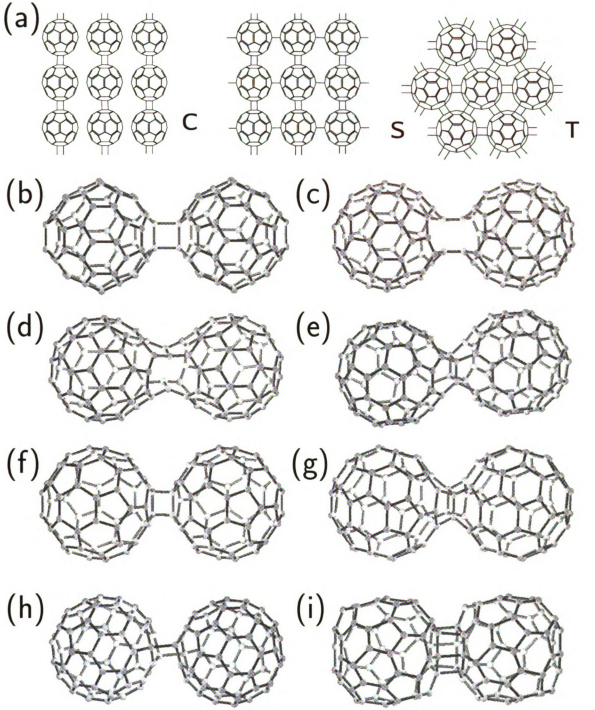

Figure 8.1: Types of covalent bonding between C_{60} molecules. (a) Arrangement of polymerized C_{60} chains (C), a square (S) and a triangular (T) 2D lattice of polymerized C_{60} molecules. Polymerization in these low-dimensional structures occurs

by the 'cycloaddition' reaction, depicted in (b). The different inter-fullerene bonding schemes considered here are shown in (b)-(i). (b) C_{60} dimerization by the 66/66 (2+2) cycloaddition reaction, which converts pairs of 'double bonds', facing each other in adjacent fullerenes, to single bonds, and leads to the formation of two new 'single bonds' connecting the fullerenes. (c) Starting with the structure (b), disruption of the two intra-fullerene bonds, affected by the cycloaddition, strengthens the inter-fullerene bonds and partly relieves structural strain. (d) Starting with the structure (c), rotation of the inter-fullerene bonds normal to the plane of the figure leads to the 'open hinge' structure. (e) Compressing structure (d), the hinges may approach each other to form a four membered common ring. (f) 56/65 (2+2) cycloaddition, related to structure (b), but involving a pair of 'single bonds' at the common pentagon-hexagon edge, rather than 'double bonds' at the common hexagon-hexagon edge. (g) Starting with the structure (c), rotation of the inter-fullerene bonds normal to the plane of the figure leads to a new bonding scheme, which I call the 56/65 four membered common ring. (h) Occurring mainly in body-centered orthorhombic fullerene lattices, the (3+3) cycloaddition establishes a covalent bond along the cell diagonal between the closest atoms in adjacent fullerenes. (i) Occurring mainly in body-centered cubic fullerene lattices, (6+6) cycloaddition connects two facing hexagons in adjacent fullerenes along the cell diagonal.

under compression. Compressing the open-hinge structure in Fig. 8.1(d) leads to a spontaneous formation of a bond connecting the bridges and the formation of a four membered common ring (FCR) between fullerene pairs. This compact covalent bonding arrangement results in a more stable and rigid bonding scheme, as depicted in Fig. 8.1(e), and appears to be another promising candidate for an ultra-hard fullerene based material. It is conceivable that the rigidity of the bulk material will scale with the number of four membered common rings it could accommodate.

With the particular symmetry of fullerene molecules and the geometrical constraints imposed by a lattice structure, it is impossible to simultaneously connect adjacent fullerenes by a particular type of bond. Design of an ultimately hard crystal may involve inter-fullerene bonding structures not considered before. One of the bonding schemes, which has not been considered before when constructing candidate super-hard C_{60} structures polymerized in 3D, is the 56/65 (2+2) cycloaddition, very similar to 66/66 (2+2) cycloaddition. The structure obtained by the 56/65 (2+2) cycloaddition, shown in Fig. 8.1(f), is closely related to the structure shown

in Fig. 8.1(b), but involves a pair of 'single bonds' at the common pentagon-hexagon edge, rather than 'double bonds' at the common hexagon-hexagon edge. The equilibrium structure and electronic properties of 2D polymerized C_{60} using this bonding type have been reported recently [159]. A similar bond rotation, which led to the FCR bonded structure in Fig. 8.1(e), could be carried out in the structure shown in Fig. 8.1(f), to yield a different bonding scheme, depicted in Fig. 8.1(g).

8.2 Inter-fullerene bonding schemes

The bonding schemes described so far can form strongly connected 2D lattices, including those in Fig. 8.1(a), which can be stacked to form a 3D lattice. In close packed 3D structures, not all bonds between adjacent planes of polymerized fullerenes are normal to these planes. The bonding scheme is dictated by the size of the fullerene and the lattice type. There are two straightforward ways to connect C_{60} molecules along a diagonal in a unit cell, namely the (3+3) cycloaddition and the (6+6) cycloaddition, depicted in Figs. 8.1(h) and (i), respectively. In some lattices the inter-fullerene nearest neighbor distance along a particular direction may be too large for a covalent bond to form.

Using the different bonding schemes mentioned above, I have arranged C_{60} molecules in 16 different crystalline lattices, such as the simple cubic (SC), body-centered orthorhombic (BCO), face-centered cubic (FCC), and body-centered cubic (BCC) lattice. For the sake of convenience, I consider all these lattices as orthorhombic lattices with a basis, spanned by the orthogonal lattice vectors **a**, **b**, and **c**. I oriented the fullerenes in a way to form one of the bonds depicted in Figs. 8.1(b)-(g) along the lattice vector directions. Among these structures, the BCC phase formed by (2+2) cycloaddition, and some of the BCO phases have been discussed in the literature previously. My results agree very well with those of *ab initio* calculations

for structural parameters and bulk modulus of the the published BCC and BCO phases [151, 152, 153], and also with other structure optimization calculations for BCO phases [154, 155]. Due to the constraints imposed by the unit cell geometry, the bond along the space diagonal in the BCO lattice is formed by the (3+3) cycloaddition. The corresponding bond between the closest carbon atoms on neighboring fullerenes is shown in Fig. 8.1(h). In the SC lattice, all bonds occur along **a**, **b**, and **c**. In the BCC lattice, new bonds along the space diagonal are formed by the (6+6) cycloaddition. In the FCC lattice, all inter-fullerene bonds, regardless of the direction, are formed by the 56/65 (2+2) cycloaddition, as depicted in Fig. 8.1(f), or bonds involving a 56/65 four membered common ring, depicted in Fig. 8.1(g).

8.3 Super-hard phases of C_{60} crystals

To determine the physical properties of these systems, I first optimized the unit cell size for each structure using a conjugate gradient energy minimization, starting from the initial structures discussed above. I have used conventional orthorhombic unit cells in my total energy and electronic structure calculations. To determine the bulk modulus, I have calculated the total energy of the system as a function of unit cell size. All the atoms have been fully relaxed for each volume, and total energies have been determined for the relaxed structures. In Fig. 8.2 I show the energy per atom versus the relative volume change for the stiffest BCC and BCO structures. Unlike the BCC structure, the BCO phase maintains its stiffness under both tensile and compressive stress. I determine the bulk modulus, which is related to the second derivative of the energy around the equilibrium, from the fitted polynomial functions.

I summarize the calculated structural, mechanical and electronic properties of the stable systems considered here in Table 8.1. I denote the structures according to the lattice and bonding type. Since the type of diagonal inter-fullerene bonds is

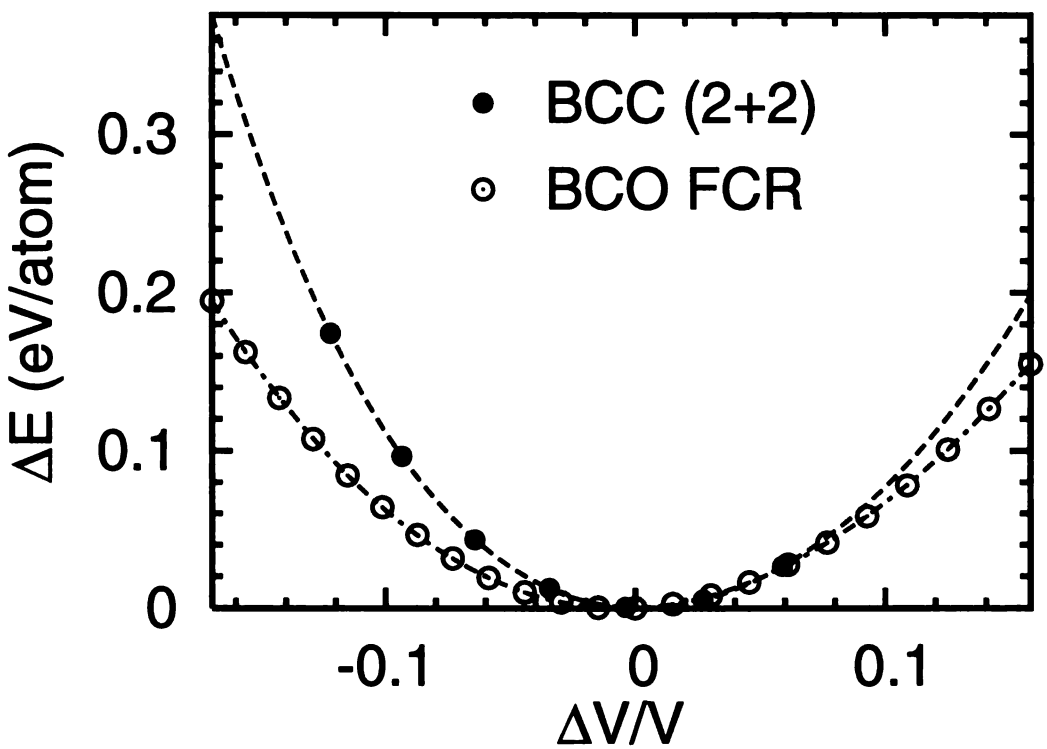

Figure 8.2: Energy change per atom ΔE versus the relative volume change $\Delta V/V$ for the stiffest BCC and BCO structures. Solid circles are data points for BCC crystals, with bonds along the sides of the conventional unit cell formed by (2+2) cycloaddition. A polynomial fit to the BCC data points, representing relaxed structures, is given by the dashed line. Open circles are the data points for the BCO lattice, containing four membered common ring (FCR) bonds between fullerenes. A polynomial fit to the BCO data points is given by the dash-dotted line.

Structure	E_{coh}(eV)	B(GPa)	ρ(g/cm^3)	E_g(eV)	$N(E_F)$	N_c	a(Å)	b(Å)	c(Å)
BCO (2+2)	−7.253	166.7	2.43	0.00	5.5	120	8.80	8.80	12.7
BCO SFCR-I	−7.283	215.5	2.43	0.00	16.5	120	8.50	8.70	13.3
BCO SFCR-II	−7.298	160.2	2.38	0.00	4.4	120	8.50	8.75	13.3
BCO FCR	−7.284	254.1	2.45	0.00	11.2	120	8.60	8.60	13.2
BCC (2+2)	−6.825	369.7	2.61	2.03	0.0	120	9.71	9.71	9.71
BCC DC	−6.818	286.3	2.57	2.16	0.0	120	9.77	9.77	9.77
BCC FCR	−6.533	352.1	2.70	0.96	0.0	120	9.58	9.58	9,58
SC (2+2)	−7.267	54.1	1.65	1.41	0.0	60	8.98	8.98	8.98
SC FCR	−7.327	184.7	1.84	1.99	0.0	60	8.65	8.65	8.65
SC OH	−7.356	166.1	1.81	0.96	0.0	60	8.71	8.71	8.71
FCC (2+2)	−7.213	179.0	2.29	0.00	2.1	240	12.78	12.78	12.78
FCC FCR	−7.213	177.9	2.29	0.00	2.4	240	12.78	12.78	12.78
diamond	−7.408	477[1]	3.51	5.4	0.0	8	3.57	3.57	3.57

Table 8.1: Calculated physical properties of polymerized C_{60} crystal structures, as compared to cubic diamond. For each stable structure considered, I list the average cohesive energy E_{coh} per atom with respect to isolated atoms, the bulk modulus B, the gravimetric density ρ, the band gap energy E_g, and the density of states at the Fermi level $N(E_F)$ in electrons per eV. I also give the number of carbon atoms in the orthorhombic conventional unit cell, N_c, and the size of the conventional unit cell along the $x-$, $y-$, and $z-$direction, given by a, b, c, respectively.

[1] Calculated value. Experimental value is $B = 443$ GPa (see Ref. [147]).

determined by the lattice type, I do not include this information in the structure notation. For each structure I list the cohesive energy E_{coh}, the bulk modulus B, the gravimetric density ρ, the fundamental band gap energy E_g, the density of states at the Fermi level $N(E_F)$, the number of atoms in the orthorhombic conventional unit cell N_c, and the dimensions a, b, c of the conventional unit cell. Four of the BCC structures, which I initially considered and which turned out to be unstable, are not listed in the table. Table 8.1 contains only one stable open hinge (OH) structure, since the OH bond in other structures is metastable and transforms into an FCR bond under compression.

8.3.1 Body-centered orthorhombic phases

My results include physical properties of 4 different BCO phases. All BCO phases are rather close-packed and have a gravimetric density around 2.4 g/cm^3, similar to the density reported in the experiment[81, 149, 150], and show a metallic character. In the BCO (2+2) structure, all inter-fullerene bonds along **a** and **b** are formed by (2+2) cycloaddition, and no covalent bonds occur along the **c** direction. The bulk modulus $B\approx$166.7 GPa of this structure is comparable to or higher than that of any elemental metal, yet its binding energy is still comparable to that of isolated C_{60} molecules. The rigidity of this BCO crystal increases, as inter-fullerene bonds along the **a**-axis are converted into four membered common rings, resulting in the BCO SFCR-I structure. Since the FCR bonding scheme is stiffer than that resulting from the (2+2) cycloaddition, the bulk modulus in this system increases by 30%. I also find that the unit cell shrinks in the **a** and **b** directions, but expands along **c** direction. The energy gained by bringing the fullerenes closer to each other in the $a-b$ plane outweighs the energy loss, associated with elongating the bonds along the cell diagonal.

The energetically more stable BCO SFCR-II structure with a single FCR is ob-

tained by breaking the bonds along the **b** axis, formed by (2+2) cycloaddition, which relieves some of the strain along the diagonal (3+3) bonds, increasing the cell depth b, as listed in Table 8.1. This phase is formed of arrays of 1D fullerene chains, polymerized with FCR bonds, inter-connected by (3+3) bonds to a 3D structure. Due to the lower number of covalent inter-fullerene bonds, the bulk modulus is lower in this system, close to the value of the BCO (2+2) phase. I find that for the same number of covalent inter-fullerene bonds, increasing the fraction of FCR bonds leads to higher bulk modulus values. Indeed, according to Table 8.1, the stiffest BCO structure is the BCO FCR phase, with all inter-fullerene bonds along **a** and **b** formed by four membered common rings. The bulk modulus of this structure, $B = 254.1$ GPa, compares favorably with the value found in cubic diamond[147], $B_{\text{dia}} = 443$ GPa, while the gravimetric density of the fullerene structure is lower than that of diamond. All the BCO phases I have investigated are very stable, with cohesive energies comparable to that of diamond. Also, based on comparing simulated x-ray patterns[154, 155] with observed x-ray data[81, 149, 150], BCO structures appear as the most likely components of the reported super-hard carbon phases. Since the highest bulk modulus of any BCO phase amounts to barely more than half the diamond value, these structures cannot account for the reported high bulk modulus values[81, 149, 150] of $\approx 500 - 900$ GPa.

8.3.2 Body-centered cubic phases

Since even a strong covalent connection between fullerenes along the **a** and **b** direction is not sufficient to yield a very high bulk modulus, I considered alternative bonding schemes with strong bonds also along the **c** direction. One realization of such a bonding scheme is the BCC lattice, with fullerenes in adjacent $a - b$ planes close enough to form covalent bonds along the **c** direction. According to Table 8.1, all BCC phases have higher bulk modulus values than BCO or any other lattice types. As a

matter of fact, the bulk modulus of the stiffest BCC phase is only 20% lower than that of cubic diamond, while the gravimetric density of this new phase is still 25% smaller than in diamond. In view of the optimized cell dimensions, which contain relatively large inter-fullerene distances that are incompatible with strong covalent bonds, I would expect the the BCC phase to be barely stable. Under compressions, however, the high stiffness of this phase benefits from the rather incompressible (6+6) bonds along the cell diagonal, resulting in the highest bulk modulus value identified in this study.

The anticipated low stability of the elongated inter-fullerene bonds in the BCC phase is reflected in its lower stability with respect to the BCO phase according to Table 8.1. As a matter of fact, in absence of steric constraints protecting the cubic symmetry, I should expect a spontaneous symmetry breaking, leading to a transformation of the BCC to the more stable BCO phase. This indeed occurs in the metastable BCC phase of C_{60} molecules, polymerized with four membered common rings in the $a-b$ plane, with no covalent bonds along the **c** axis, and (6+6) connections along the unit cell diagonal.

As suggested above, the stiffness of the BCC structures under compression is in stark contrast to their much lower strength under tension. This is seen from the asymmetry of the elastic response of the BCC (2+2) lattice, shown in Fig. 8.2, which is very different from the almost symmetric elastic response of the BCO lattice subject to relative volume changes. Moreover, beyond a critical tensile strain, all BCC phases undergo structural changes, reflected in the lack of data points for the BCC (2+2) phase at large positive relative volume changes $\Delta V/V$ in Fig. 8.2.

All stable BCC phases listed in Table 8.1 exhibit identical bonding along the **a**, **b**, and **c** axes. I found all these structures to be insulators with a $1-2$ eV fundamental band gap, and a gravimetric density close to 2.6 g/cm^3. The stiffest BCC crystal is BCC $(2+2)$ with the bulk modulus $B\approx$370 GPa. Since the double chain (DC)

inter-fullerene connection is weaker, the BCC DC structure has a lower bulk modulus than BCC (2 + 2), but is still stiffer than other lattice types due to the presence of the incompressible (6 + 6) inter-fullerene connections along the cell diagonal. The dominant role of (6 + 6) bonding in achieving a high stiffness is reflected in the similar bulk moduli of the BCC FCR and the BCC (2 + 2) structures. Apparently, the intrinsic higher stiffness of FCR connections, which lead to high bulk modulus values in BCO lattices, is of secondary importance in this case.

8.3.3 Simple cubic phases

As mentioned above, the marginal stability of the BCC lattice was caused by the large size of the C_{60} molecule in the center of the cubic unit cell. I may expect that removal of the central fullerene will stabilize the cubic lattice by reducing the strain along the **a**, **b**, and **c** directions. Even though the resulting simple cubic phase should be energetically more favorable, the lower packing fraction of fullerenes may lower the bulk modulus. I have studied 4 different SC phases. Out of these, SC with a double chain bond transforms into the SC (2+2) structure even under small pressure, thus eliminating it as a candidate for a super hard structure. Since the compressibility of the SC lattice directly reflects the rigidity of the inter-fullerene connections along the cube edges, I can easily rationalize that the bulk modulus of SC FCR is the highest among the SC lattices, followed SC OH and finally SC (2+2), the softest SC lattice. As seen in Table 8.1, the gravimetric densities of all SC phases are approximately half the value of diamond. All SC fullerene crystals are insulators with a $\approx 1-2$ eV band gap. The SC OH phase with open hinge connections is unique in containing only 3-fold coordinated carbon atoms, implying sp^2 inter-atomic bonding throughout the structure. This results in a high bulk modulus $B \approx 166$ GPa at a relatively low density of 1.81 g/cm^3. As a logical consequence, schwarzite or Mackay structures consisting of a simple cubic lattice formed by nanotubes with perfect sp^2 interconnects, should

be extremely rigid. Due to the constraints associated with the cubic symmetry of such a structure, I find the number of atoms in C_{60} to be insufficient to form such perfect sp^2 interconnects at the vertices.

8.3.4 Face-centered cubic phases

The last lattice type I have investigated is FCC, where all inter-fullerene bonds are identical. I have considered 56/65 connections, displayed in Fig. 8.1(f), and 56/65 four membered common rings, shown in Fig. 8.1(g). In spite of the different bonding, the two structures share similar values of the bulk modulus, unit cell size and gravimetric density. The unexpected insensitivity of the bulk modulus $B \approx 180$ GPa to the bonding scheme is associated with extreme structural deformations of the fullerenes, which degrade substantially their initial structural rigidity. Consequently, the presence of strong covalent inter-fullerene bonds is only beneficial for an overall high structural stiffness, if fullerene deformations do not reduce the intrinsic rigidity of the molecule. I find both FCC phases to be metallic with a similar density of states at the Fermi level. As seen in Table 8.1, the metallic behavior of FCC structures is unique among the cubic lattices.

8.4 Conclusions

A major advantage of fullerene based super-hard materials is their formation mechanism by self-assembly from sub-nanometer sized fullerenes. This is particularly beneficial, when micrometer-sized voids are to be filled with a rigid structure to enhance the overall stiffness. The high structural rigidity of polymerized fullerenes is coupled with a low gravimetric density, which lies below the diamond value in all the compounds studied here, mainly due to the empty space inside the fullerenes. Nevertheless, I must notice that the stiffest phases tend to have the highest mass

densities. As a matter of fact, among all crystalline materials, the system with the highest bulk modulus, diamond, distinguishes itself also by the largest number of atoms per unit volume.

In conclusion, I combined total energy and structure optimization calculations to explore the physical properties of new hard phases consisting of fullerenes polymerized in 3D. I have identified 12 different stable crystal structures that are very stiff. The bulk moduli I have found in 3D fullerenes crystals are as high as 80% of the diamond value, in contradiction to experiments reporting materials stiffer than diamond[81, 149, 150]. The BCC lattice structure, which shows the highest bulk modulus value among those addressed here, turned out to be the least stable among the structures investigated. The bulk modulus of other structures, which should form more readily under moderate conditions, lies below half the diamond value, but still exceeds that of most metals. The possibility of self-assembling these rigid structures from sub-nanometer C_{60} fullerenes, which may be filled easily into nano-cavities in bulk structures, may lead to new materials with a superior stiffness and stability at high temperatures. The electronic properties of 3D structures formed of polymerized fullerenes depend on the lattice type, with BCO systems exhibiting metallic behavior, whereas the majority of cubic systems are insulators with a $\approx 1 - 2$ eV fundamental band gap.

Chapter 9

Thermal Contraction of Carbon Fullerenes and Nanotubes

The following discussion of thermal expansion properties of fullerenes and nanotubes follows that presented in Reference [163].

9.1 Materials exhibiting negative thermal expansion

There has been increasing demand for high performance composites with near-zero thermal expansion [164, 165]. In such composites, thermal expansion of one component may be compensated by a thermal contraction of other components [166]. Since most materials expand thermally, there has been extensive search for materials with a negative thermal expansion coefficient. Thermal contraction has been observed in quasi one-dimensional polymers such as rubber, polyethylene, polyacetylene, polydiacetylenes, and selenium [167, 168, 169, 170, 171], layered systems such as graphite and boron nitride [172, 173, 174], and three-dimensional covalent networks found in oxides [175, 176] such as $NaTi_2P_3O_{12}$ and ZrW_2O_8. Since carbon fullerenes

and nanotubes consist of sp^2 bonded carbon networks related to graphite, I expect them to also contract at low temperatures.

Thermally induced contraction and expansion result from a competition between internal energy and entropy. In the harmonic regime at low temperatures, low-dimensional systems gain structural and vibrational entropy by exploring the voids in configurational space at relatively little energy cost. The dominating effect of entropy in this regime results in a contraction. Only at higher temperatures do the anharmonicities in the interatomic interaction play a significant role, causing an overall expansion. I expect the transition from contraction at low temperatures to expansion at high temperatures to be a universal phenomenon in low-dimensional materials, and only the crossover temperature to change from system to system. As I will discuss in the following, the interplay between energy and entropy has a particularly interesting effect on the thermal behavior of nanostructures.

Following the discovery of fullerenes [94] such as C_{60}, carbon nanotubes [11, 22], perfect cylinders formed of rolled graphite monolayers, are now being considered as important building blocks for nanotechnology [177, 115]. Thermal expansion properties of carbon nanotubes are of great importance, since the electrical characteristic of complex nanotube-based circuitry will change significantly due to differential contraction imposing internal stress [178]. Another important aspect of the thermal expansion of nanotubes is the effect on the mechanical properties of nanotube-based high-performance composites [179]. Even though the same sp^2 bonding is shared by 2D graphite, 1D nanotubes and 0D fullerenes, I find it important to determine the effect of dimensionality on the thermal contraction at low temperatures and the crossover point to thermal expansion.

9.2 Computational approach

In this Chapter, I use Nosé-Hoover molecular dynamics simulations [54, 55] to determine how temperature affects the volume of C_{60} molecules and carbon nanotubes, and also to determine how their length changes with increasing temperature. I show that at low temperatures, both fullerene molecules and carbon nanotubes contract in length and volume. Only at temperatures beyond several hundred degrees Kelvin, the initial contraction changes to an overall expansion, driven by exciting anharmonic phonon modes. I determine temperature-induced structural changes by investigating the coupling between vibrational modes and the shape of fullerenes and nanotubes. I identify those vibration modes that play a dominant role in how the volume and length of fullerenes and nanotubes change with temperature.

To correctly reproduce the change in length and volume of nanostructures in response to temperature, I need to describe precisely those energy changes associated with shape deformations in the anharmonic regime. I found that the popular Tersoff potential [141] introduces a spurious soft "harmonica twist" mode that modifies the length of a straight tube. To avoid this problem, I use a parameterized linear combination of atomic orbitals formalism based on a universal parametrization of *ab initio* density functional results for structures as different as C_2, carbon chains, graphite, and diamond [42]. This energy functional is particularly suited for my purpose, as it is based on an electronic Hamiltonian that goes well beyond the nearest neighbor approximation, thus also describing anharmonic effects due to the $sp^2 \rightarrow sp^3$ rehybridization during deformation. I make use of the computationally efficient approach [8] that has been previously used with success to describe the formation of multiwall nanotubes [49], nanopeapods [56], the dynamics of the "bucky-shuttle" [17], and the disintegration of fullerenes [48].

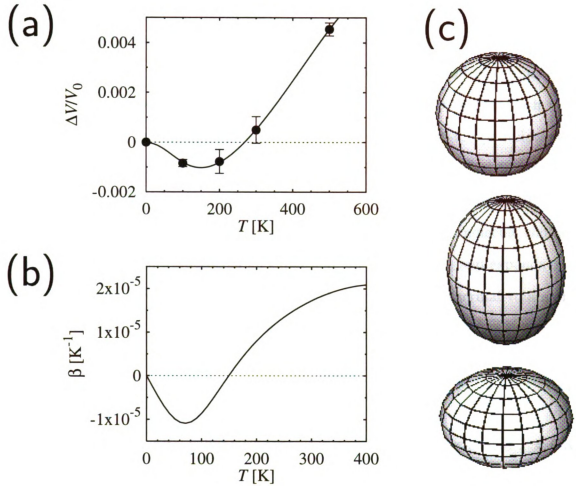

Figure 9.1: (a) Relative volume change $\Delta V/V_0$ in a C_{60} molecule as a function of temperature T. (b) Temperature dependence of the thermal volumetric expansion coefficient β. (c) Schematic snap shots of the ellipsoidal deformation mode, responsible for volumetric contraction at low temperatures.

9.3 Thermal contraction in fullerenes as zero dimensional model systems

As suggested earlier, the most pronounced deviation from the thermal expansion, which is typically associated with three-dimensional objects, can be expected in the zero-dimensional C_{60} molecule. To study volumetric changes with temperature, I coupled the C_{60} molecule to a thermal heat bath at temperatures ranging from $T = 0$ K to $1,000$ K. My molecular dynamics simulations indicate that the C_{60} molecule shows

an ellipsoidal deformation, one of the softest vibration modes that is depicted in Figure 9.1(c), even at low temperatures. In view of this fact, I diagonalized the gyration tensor of a deformed C_{60} molecule to obtain the principal axes and to estimate the volume at any moment in time. In my simulations, I changed the heat bath temperature stepwise, and discarded data obtained during the first 0.2 ps following a temperature change to allow for equilibration with the heat bath. My data for the volume change $\Delta V(T)$, shown in Figure 9.1(a), represent the average over $10^4 - 10^5$ time steps of $\Delta t = 5\times10^{-16}$ s. These results suggest that a C_{60} molecule shows a volumetric contraction, rather than an expansion, up to $T\approx260$ K, and expands only at higher temperatures. Figure 9.1(b) depicts the corresponding thermal volumetric expansion coefficient, which is defined by

$$\beta = \frac{1}{V}\frac{dV}{dT} . \tag{9.1}$$

I find that the thermal volumetric expansion coefficient starts at zero at $T = 0$ K, and initially decreases linearly to $\beta\approx-1\times10^{-5}$ K^{-1}. The minimum in the $\beta(T)$ curve, corresponding to the maximum thermal volumetric contraction, occurs at $T\approx70$ K. Above this temperature, the volumetric contraction of C_{60} slows down. At $T\approx150$ K, C_{60} achieves its smallest volume, and its volumetric contraction turns to an expansion. Further analysis of the changes in the principal axes with temperature showed that among the soft vibration modes, it is the quadrupolar deformation, which keeps the surface area constant, that dominates the thermal contraction at low temperatures. Thermal expansion at higher temperatures results from a bond expansion, which is reflected in a radial breathing mode that changes the surface area of the fullerene.

9.4 Thermal contraction in nanotubes as one dimensional model systems

Next, I investigate the effect of temperature on the volume and length of carbon nanotubes as model one-dimensional objects. Due to their natural abundance among single-wall carbon nanotubes grown by pulsed-laser vaporization [180], I focus on (10, 10) nanotubes in my simulations. Also, nanotubes with a similar diameter are the most likely constituents of "bucky paper", for which initial experimental measurements of thermal expansion have been performed [181]. I considered $50-1,500$ Å long open-ended segments of an isolated (10, 10) nanotube in order to calculate the effect of temperature on its volume and total length. As in the C_{60} simulations, the nanotube was coupled to a Nosé-Hoover thermostat in my canonical molecular dynamics simulations. Considering an open-ended segment rather than an infinite nanotube with periodic boundary conditions, I avoided introduction of spurious phonon modes and problems due to a fluctuating unit cell size. Since the vibrations of an open-ended segment are altered by the presence of under-coordinated carbon atoms, I ignored the five terminating layers[1] when evaluating the total length and volume of the tube segment.

The estimation of the volume of a deformed nanotube is less trivial than for the C_{60} molecule due to the large number of relevant phonon modes, illustrated in Figure 9.2(e)−(h). I determine the volume of a deformed nanotube as a sum of partial volumes associated with each deformed layer, given by a product of its cross section area and the distance between adjacent layers. In a deformed nanotube segment, I first determine the center of mass of the relevant layers and use the distance between them as the length. I approximate the cross-section area of each layer by that of a

[1] In achiral nanotubes aligned with the z axis, I define the ensemble of atoms with the same z coordinate as a 'layer'. In the (10, 10) nanotube, a layer consists of a 20 atom ring along the tube circumference.

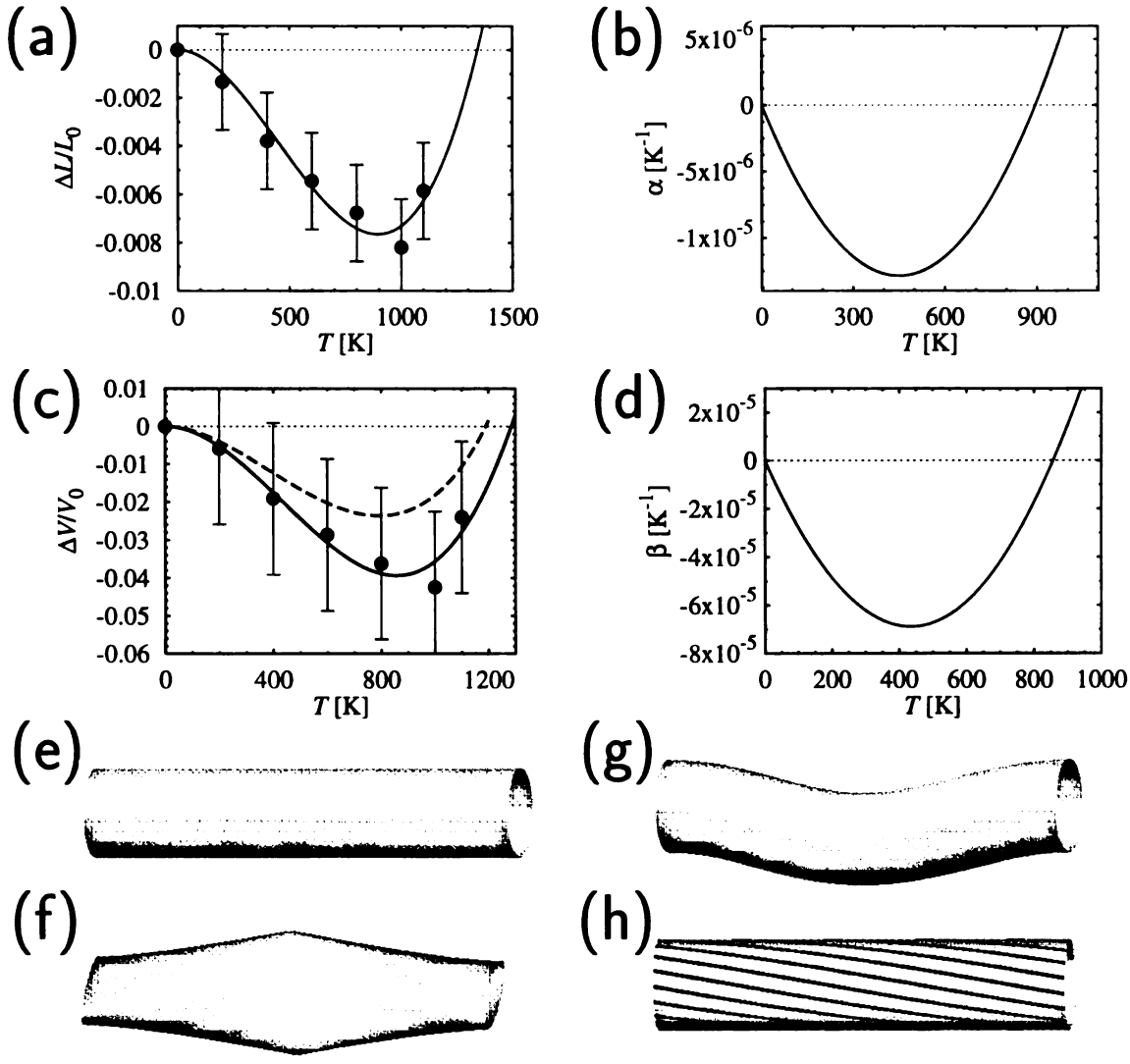

Figure 9.2: (a) Relative length change $\Delta L/L_0$ in a $(10, 10)$ carbon nanotube as a function of temperature T. (b) Temperature dependence of the thermal linear expansion coefficient β. (c) Relative volume change $\Delta V/V_0$ and (d) thermal volumetric expansion coefficient β of the $(10, 10)$ nanotube as a function of temperature. Schematic snap shots of selected soft phonon modes that couple strongly to the length and volume of the nanotube: (e) reference structure of the unperturbed tube, (f) optical pinch mode, (g) transverse acoustic bending mode, (h) twist mode. The relative contribution of the pinch mode to the volume change is shown by the dashed line in (c).

circle with radius r. This radius is given by the average distance of each atom from the center of mass of that layer. Similar to my treatment of the C_{60} molecule, I first determine the three principal axes for each nanotube layer by diagonalizing its gyration tensor. Then, I define the volume as the product of the elliptical cross-section area normal to the tube axis and the distance between adjacent layers.

My results for the response of the nanotube to changing temperature are displayed in Figure 9.2. Similar to my results for the C_{60} molecule, data points representing the volume and length at a particular temperature have been obtained by taking a time average over $10^4 - 10^5$ time steps of $\Delta t = 5\times10^{-16}$ s after equilibration with the heat bath. I have filtered out high-frequency noise using a simplified Fourier analysis of the total volume and length as a function of time at 0 K, 200 K, 400 K, 800 K, 1,000 K, and 1,100 K. The error bars reflect also the additional uncertainty associated with this fitting process.

My results for the temperature dependence of the tube length, shown in Figure 9.2(a), suggest that carbon nanotubes should contract up to very high temperatures close to 1,300 K. These findings are in agreement with the observed contraction in "bucky paper" below room temperature [181]. The solid line is a fit to the same functional form as used in the thermal expansion analysis of graphite [135], which also shows an in-plane contraction at low temperatures. In analogy to Eq. (9.1), the linear thermal expansion coefficient α is defined as

$$\alpha = \frac{1}{L}\frac{dL}{dT} . \tag{9.2}$$

Similar to the volumetric expansion coefficient of C_{60} depicted in Figure 9.1(b), the linear expansion coefficient α of a nanotube decreases from its initial zero value at $T = 0$ K, and becomes negative. The minimum value in the $\alpha(T)$ curve, corresponding to the maximum thermal contraction, is $\alpha \approx -1.2\times10^{-5}$ K^{-1} and occurs at $T\approx$400 K.

Contraction continues up to $T \approx 900$ K, where α vanishes and the tube length is minimum. Above 900 K, α becomes positive, indicating onset of thermal expansion, as the anharmonic part of the inter-atomic potential gains in importance. Above 1,300 K, the tube should exceed its initial length at $T = 0$ K.

My results reveal that not only do nanotubes contract axially, but they also show volumetric contraction up to very high temperatures, due to radial deformations discussed below. As shown in Figure 9.2(c), the volume decreases gradually, as the temperature increases from 0 K to $T \approx 800$ K. At $T \approx 800$ K, the volume starts expanding again, and exceeds its original value at $T \approx 1200$ K. The larger error bars are a consequence of a combined uncertainty in the average tube radius and length. The volumetric thermal expansion coefficient, presented in Figure 9.2(d), decreases from zero to its minimum value $\beta \approx -7 \times 10^{-5}$ at $T \approx 400$ K, and then increases to reach zero value at $T \approx 800$ K, corresponding to the smallest tube volume.

9.4.1 Physical origin of thermal contraction

In order to understand the origin of thermal contraction, I analyzed my molecular dynamics simulations in terms of normal vibration modes that couple strongly to the length and volume. As for C_{60}, I focused on the soft modes that do not change the surface area of the reference tube, shown in Figure 9.2(e). The significant modes are the pinch mode, the bending mode, and the twist mode, depicted in Figures 9.2(f)–(h), respectively. Whereas short-wavelength modes, such as the pinch mode, can be described in my atomistic molecular dynamics simulations, description of long-wavelength modes requires long tube segments exceeding my computational resources. To describe the long-wavelength bending and twisting phonon modes, I performed molecular dynamics simulations based on a model assumption of rigid atomic layers that interact according to the energy functional described above.

My long-wavelength calculations suggest the transverse acoustic bending mode,

depicted in Figure 9.2(g), to be very soft, as it involves a shear motion that requires a minimum of bond stretching and bending. My simulations indicate that length contraction due to this mode saturates in $(10, 10)$ tube segments with a length close to 100 Å. I find the bending mode to contribute almost one third towards the length contraction of a $(10, 10)$ nanotube. Also the soft twisting mode, depicted in Figure 9.2(h), can be viewed as a shear mode. I found this mode to be active in the orientational melting within a nanotube rope at low temperatures [182], and to contribute up to $\approx 10\%$ towards the tube length contraction. Since none of these modes affects the tube cross-section, their effect on the volumetric contraction is very small.

My calculations suggest that an important contribution towards the longitudinal contraction, and the dominant contribution towards the volumetric contraction, comes from the optical "pinch" mode, shown in Figure 9.2(f). The dashed line in Figure 9.2(c) indicates the analytically calculated contribution of a pure pinch phonon mode to the total volume change. In the pinch mode, each tube layer in the pinch mode is subject to an elliptical deformation. To calculate the volumetric contraction in this mode, I assumed the circumference C of the elliptical cross-section to be constant. In this case, the area S of the ellipse decreases monotonically with increasing eccentricity $t \equiv b/a$, defined as the ratio of its major and minor axes a and b. Making use of the complete elliptic integral of the second kind $E(x)$, the ellipse area is given by $S(t) = (\pi C^2/16)\,(t/[E(1-t^2)]^2)$. Assuming that t changes linearly between t_{min} and 1 along the axial direction, the total volume V of the deformed nanotube segment of length L changes as $V = \int_0^L dlS(t) = L < S >$, where $< S >= \int_{t_{\rm min}}^1 dtS(t)/(1 - t_{\rm min})$. I find that the pinch mode accounts for nearly one half of the volume change, but only one third of the total length change.

The relative contribution of the changing cross-section area S and length L towards the volume change is determined by the decomposition $\Delta V/V_0 = \Delta L/L_0 + \Delta S/S_0 + (\Delta L/L_0)(\Delta S/S_0)$. This expression allows us to extract additional infor-

mation about the thermal behavior of nanotubes, in particular the radial thermal expansion coefficient α_r, from the known length and volume changes, presented in Figures 9.2(a)−(d). I find that in the temperature range of interest, the average tube radius should contract. This result agrees with experimental observations [183], but contradicts simulations based on Tersoff potential [184]. My numerical value for the radial contraction at low temperatures $\alpha_r \approx -2\times10^{-5}$ K^{-1} is about one order of magnitude larger than X-ray results reported for single-wall nanotube ropes [183], where the dominating pinch mode is likely to be suppressed by inter-tube interactions. In agreement with the experimental data [183], I expect a volumetric thermal expansion of nanotube ropes due to an increasing inter-tube distance, in analogy to the volumetric expansion of bulk graphite, which is dominated by the expansion along the c-axis.

9.5 Summary

In summary, I investigated thermal expansion behavior of fullerenes and carbon nanotubes using molecular dynamics simulations. I showed that C_{60} molecule exhibits volumetric thermal contraction up to $T \leq 260$ K, whereas carbon nanotubes contract in length and volume for $T \approx 800$ K. Among the different active vibration modes, I found the ellipsoidal deformation mode to dominate the volumetric contraction of C_{60}. In nanotubes, length contraction is shared by bending, twist and pinch modes, whereas the volumetric contraction is dominated by the pinch mode. Combining thermal contraction of nanotubes with thermal expansion of a host material may yield high performance composites showing negligible thermal expansion up to high temperatures.

Chapter 10

Unusually High Thermal Conductivity of Carbon Nanotubes

The following discussion of thermal conductivity in carbon nanotubes follows that presented in Reference [143].

10.1 Introduction

With the continually decreasing size of electronic and micromechanical devices, there is an increasing interest in materials that conduct heat efficiently, thus preventing structural damage. The stiff sp^3 bonds, resulting in a high speed of sound, make monocrystalline isotopically pure diamond one of the best thermal conductors [185]. An unusually high thermal conductance should also be expected in carbon nanotubes[11, 1], which are held together by even stronger sp^2 bonds. These systems, consisting of seamless and atomically perfect graphitic cylinders few nanometers in diameter, are self-supporting. The rigidity of these systems, combined with virtual absence of atomic defects or coupling to soft phonon modes of the embedding medium, should make isolated nanotubes very good candidates for efficient thermal conductors. This conjecture has been confirmed by experimental data that are consistent

with a very high thermal conductivity for nanotubes [186, 187].

In the following, I will present results of molecular dynamics simulations using the Tersoff potential [141], augmented by Van der Waals interactions in graphite, for the temperature dependence of the thermal conductivity of nanotubes and other carbon allotropes. I will show that isolated nanotubes are at least as good heat conductors as high-purity diamond. My comparison with graphitic carbon shows that inter-layer coupling reduces thermal conductivity of graphite within the basal plane by one order of magnitude with respect to the nanotube value which lies close to that for a hypothetical isolated graphene monolayer.

The thermal conductivity λ of a solid along a particular direction, taken here as the z axis, is related to the heat flowing down a long rod with a temperature gradient dT/dz by

$$\frac{1}{A}\frac{dQ}{dt} = -\lambda\frac{dT}{dz}\,, \tag{10.1}$$

where dQ is the energy transmitted across the area A in the time interval dt. In solids where the phonon contribution to the heat conductance dominates, λ is proportional to Cvl, the product of the heat capacity per unit volume C, the speed of sound v, and the phonon mean free path l. The latter quantity is limited by scattering from sample boundaries (related to grain sizes), point defects, and by umklapp processes. In an experiment, the strong dependence of the thermal conductivity λ on l translates into an unusual sensitivity to isotopic and other atomic defects. This is best illustrated by the reported thermal conductivity values in the basal plane of graphite [188] which scatter by nearly two orders of magnitude. As similar uncertainties may be associated with thermal conductivity measurements in "mats" of nanotubes [186, 187], I decided to determine this quantity using molecular dynamics simulations.

10.2 Limitation of theoretical approaches describing thermal conductivity

The first approach used to calculate λ was based on a direct molecular dynamics simulation. Heat exchange with a periodic array of hot and cold regions along the nanotube has been achieved by velocity rescaling, following a method that had been successfully applied to the thermal conductivity of glasses [189]. Unlike glasses, however, nanotubes exhibit an unusually high degree of long-range order over hundreds of nanometers. The perturbations imposed by the heat transfer reduce the effective phonon mean free path to below the unit cell size. I found it hard to achieve convergence, since the phonon mean free path in nanotubes is significantly larger than unit cell sizes tractable in molecular dynamics simulations. This method requires long nanotubes to converge in order to separate regions coupled to the thermostat from "unperturbed" tube sections. This can not be guaranteed in short nanotubes, resulting in a nonlinear temperature profile, shown in Figure 10.1, in contrary to the expected linear temperature profile at $z \approx 0$.

As an alternate approach to determine the thermal conductivity, I used equilibrium molecular dynamics simulations [190, 191] based on the Green-Kubo expression that relates this quantity to the integral over time t of the heat flux autocorrelation function by [192]

$$\lambda = \frac{1}{3Vk_BT^2}\int_0^\infty < \mathbf{J}(t)\cdot\mathbf{J}(0) > dt\,. \tag{10.2}$$

Here, k_B is the Boltzmann constant, V is the volume, T the temperature of the sample, and the angled brackets denote an ensemble average. The heat flux vector $\mathbf{J}(t)$ is defined by

$$\mathbf{J}(t) = \frac{d}{dt}\sum_i \mathbf{r}_i\Delta e_i = \sum_i \mathbf{v}_i\Delta e_i - \sum_i\sum_{j(\neq i)} \mathbf{r}_{ij}(\mathbf{f}_{ij}\cdot\mathbf{v}_i)\,, \tag{10.3}$$

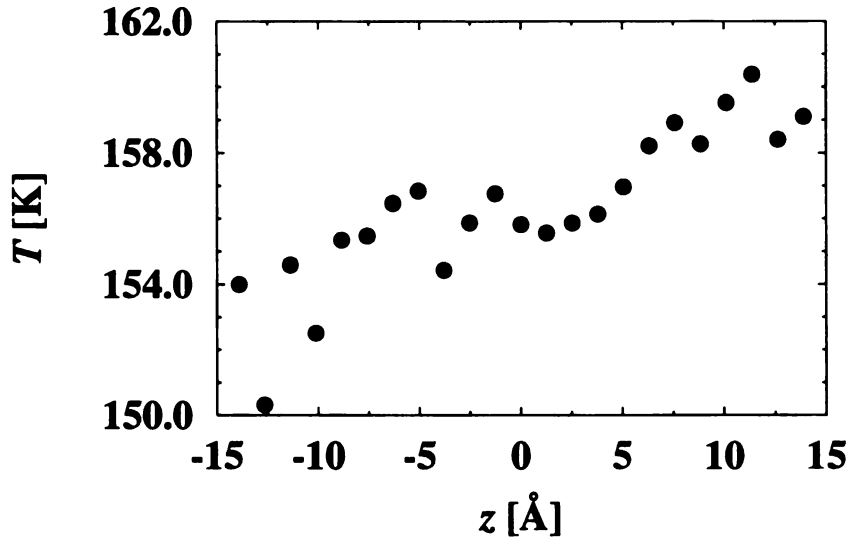

Figure 10.1: Temperature profile in a direct molecular dynamics simulation of heat flow in a $(10, 10)$ nanotube. Temperature is controlled by thermostats located close to $z = -15$Å and $z = 15$Å. Since the nanotube is not long enough, the temperature profile failed to converge, reaching a linear temperature profile near $z = 0$.

where $\Delta e_i = e_i - < e >$ is the excess energy of atom i with respect to the average energy per atom $< e >$. $\mathbf{r}_i$ is the position and $\mathbf{v}_i$ the velocity of atom i, and $\mathbf{r}_{ij} = \mathbf{r}_j - \mathbf{r}_i$. Assuming that the total potential energy $U = \sum_i u_i$ can be expressed as a sum of binding energies u_i of individual atoms, then $\mathbf{f}_{ij} = -\nabla_i u_j$, where ∇_i is the gradient with respect to the position of atom i.

In low-dimensional systems, such as nanotubes or graphene monolayers, I infer the volume from the way that these systems pack in space (nanotubes form bundles and graphite a layered structure, both with an inter-wall separation of $\approx$3.4 Å) in order to convert thermal conductance of a system to thermal conductivity of a material.

Once $\mathbf{J}(t)$ is known, the thermal conductivity can be calculated using Eq. (10.2). I found, however, that these results depend sensitively on the initial conditions of each simulation, thus necessitating a large ensemble of simulations. This high computa-

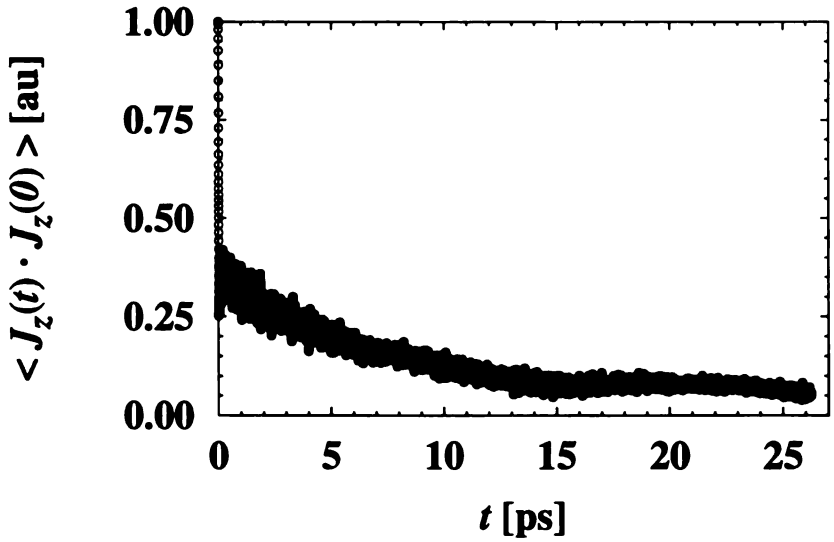

Figure 10.2: Velocity autocorrelation function, averaged over a large number of ensembles. The timescale shown is not long enough to obtain a converged value of the velocity autocorrelation. The sharp drop at $t \approx 0$ corresponds to soft phonon modes, which contribute little to the thermal conductivity.

tional demand was further increased by the slow convergence of the autocorrelation function, requiring long integration time periods. In Figure 10.2 I show the velocity autocorrelation function averaged over a large number of ensembles, obtained by randomizing the initial coordinates and velocities. The fact that the autocorrelation function $< \mathbf{J}(t) \cdot \mathbf{J}(0) >$ does not converge to 0 indicates that time periods much longer than 25 ps are required to correctly describe thermal conduction. This is a clear indication of a long phonon lifetime, and long phonon mean free path.

These disadvantages have been shown to be strongly reduced in an alternate approach [193] that combines the Green-Kubo formula with nonequilibrium thermodynamics [194, 195] in a computationally efficient manner [196]. In this approach, the thermal conductivity along the z axis is given by

$$\lambda = \lim_{\mathbf{F}_e \to 0} \lim_{t \to \infty} \frac{< J_z(\mathbf{F}_e, t) >}{F_e T V} , \tag{10.4}$$

where T is the temperature of the sample, regulated by a Nosé-Hoover thermostat [54, 55], and V is the volume of the sample. $J_z(\mathbf{F}_e, t)$ is the z component of the heat flux vector for a particular time t. $\mathbf{F}_e$ is a small fictitious "thermal force" (with a dimension of inverse length) that is applied to individual atoms. This fictitious force $\mathbf{F}_e$ and the Nosé-Hoover thermostat impose an additional force $\Delta\mathbf{F}_i$ on each atom i. This additional force modifies the gradient of the potential energy and is given by

$$\Delta\mathbf{F}_i = \Delta e_i \mathbf{F}_e - \sum_{j(\neq i)} \mathbf{f}_{ij}(\mathbf{r}_{ij}\cdot\mathbf{F}_e) + \frac{1}{N}\sum_j \sum_{k(\neq j)} \mathbf{f}_{jk}(\mathbf{r}_{jk}\cdot\mathbf{F}_e) - \alpha\mathbf{p}_i \,. \tag{10.5}$$

Here, α is the Nosé-Hoover thermostat multiplier acting on the momentum $\mathbf{p}_i$ of atom i. α is calculated using the time integral of the difference between the instantaneous kinetic temperature T of the system and the heat bath temperature T_{eq}, from $\dot{\alpha} = (T - T_{eq})/Q$, where Q is the thermal inertia. The third term in Eq. (10.5) guarantees that the net force acting on the entire N-atom system vanishes.

10.3 Computational results

In Figure 10.3 I present the results of my nonequilibrium molecular dynamics simulations for the thermal conductance of an isolated $(10, 10)$ nanotube aligned along the z axis. In my calculation, I consider 400 atoms per unit cell, and use periodic boundary conditions. Each molecular dynamics simulation run consists of 50,000 time steps of 5.0×10^{-16} s. My results for the time dependence of the heat current for the particular value $F_e = 0.2$ Å^{-1}, shown in Figure 10.3(a), suggest that $J_z(t)$ converges within the first few picoseconds to its limiting value for $t\to\infty$ in the temperatures range below 400 K. The same is true for the quantity $J_z(t)/T$, shown in Figure 10.3(b), the average of which is proportional to the thermal conductivity λ according to Eq. (10.4). My molecular dynamics simulations have been performed for a total time length of 25 ps to represent well the long-time behavior.

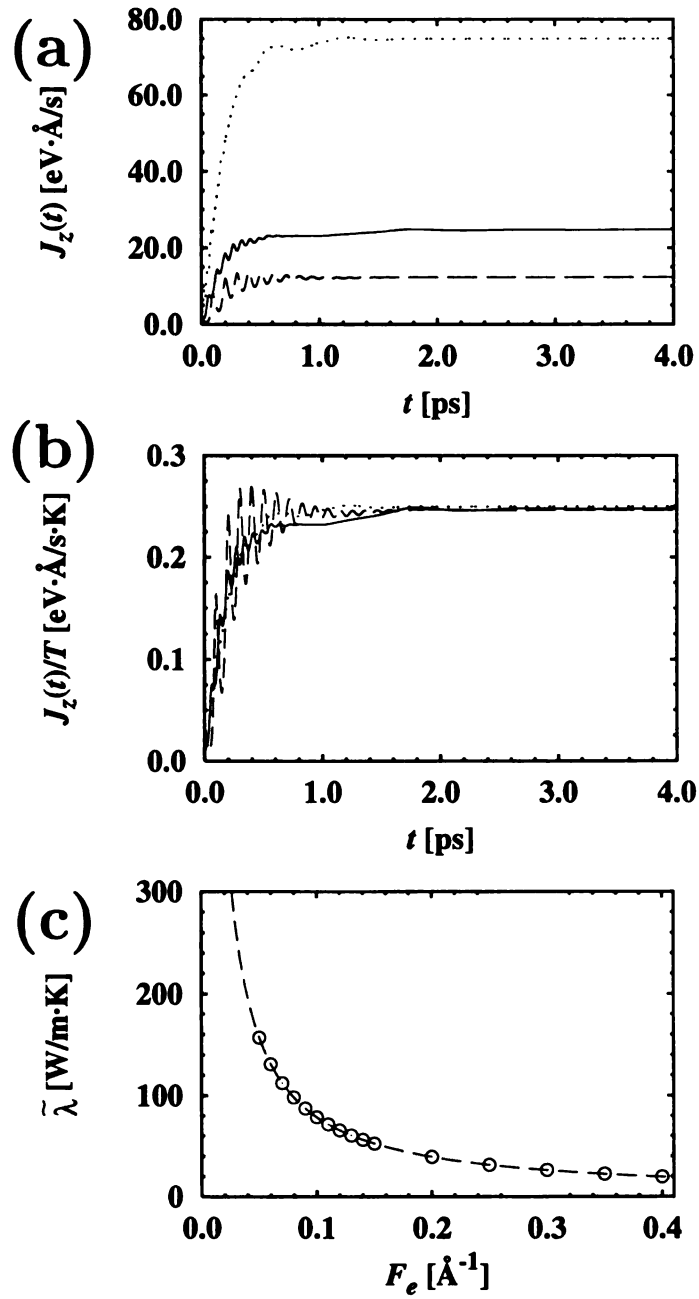

Figure 10.3: (a) Time dependence of the axial heat flux $J_z(t)$ in a $(10, 10)$ carbon nanotube. Results of nonequilibrium molecular dynamics simulation at a fixed applied thermal force $F_e = 0.2$ Å^{-1}, are shown at temperatures $T = 50$ K (dashed line), 100 K (solid line), and 300 K (dotted line). (b) Time dependence of $J_z(t)/T$, a key quantity for the calculation of the thermal conductivity, for $F_e = 0.2$ Å^{-1} and the same temperature values. (c) Dependence of the heat transport on the applied heat force F_e in the simulations for $T = 100$ K. The dashed line represents an analytical expression that is used to determine the thermal conductivity λ by extrapolating the simulation data points $\tilde{\lambda}$ for $F_e \to 0$.

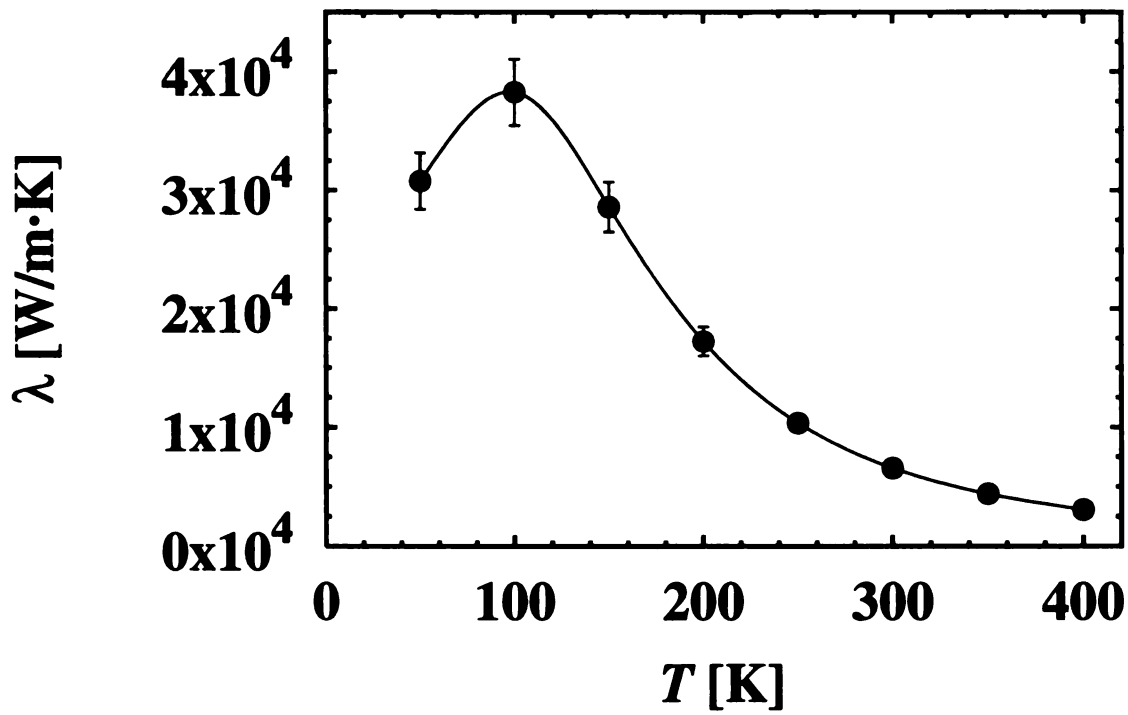

Figure 10.4: Temperature dependence of the thermal conductivity λ for a $(10, 10)$ carbon nanotube for temperatures below 400 K.

In Figure 10.3(c) I show the dependence of the quantity

$$\tilde{\lambda} \equiv \lim_{t \to \infty} \frac{< J_z(\mathbf{F}_e, t) >}{F_e T V} \tag{10.6}$$

on F_e. I have found that direct calculations of $\tilde{\lambda}$ for very small thermal forces carry a substantial error, as they require a division of two very small numbers in Eq. (10.6). I base my calculations of the thermal conductivity at each temperature on 16 simulation runs, with F_e values ranging from $0.4 - 0.05$ Å^{-1}. As shown in Figure 10.3(c), data for $\tilde{\lambda}$ can be extrapolated analytically for $\mathbf{F}_e \to 0$ to yield the thermal conductivity λ, shown in Figure 10.4.

My results for the temperature dependence of the thermal conductivity of an isolated $(10, 10)$ carbon nanotube, shown in Figure 10.4, reflect the fact that λ is proportional to the heat capacity C and the phonon mean free path l. At low tem-

peratures, l is nearly constant, and the temperature dependence of λ follows that of the specific heat. At high temperatures, where the specific heat is constant, λ decreases as the phonon mean free path becomes smaller due to umklapp processes. My calculations suggest that at $T = 100$ K, carbon nanotubes show an unusually high thermal conductivity value of 37,000 W/m·K. This value lies very close to the highest value observed in any solid, $\lambda = 41,000$ W/m·K, that has been reported [185] for a 99.9% pure ^{12}C crystal at 104 K. In spite of the decrease of λ above 100 K, the room temperature value of 6,600 W/m·K is still very high, exceeding the reported thermal conductivity value of 3,320 W/m·K for nearly isotopically pure diamond [197].

I found it useful to compare the thermal conductivity of a (10, 10) nanotube to that of an isolated graphene monolayer as well as bulk graphite. For the graphene monolayer, I unrolled the 400-atom large unit cell of the (10, 10) nanotube into a plane. The periodically repeated unit cell used in the bulk graphite calculation contained 720 atoms, arranged in three layers. The results of my calculations, presented in Figure 10.5, suggest that an isolated nanotube shows a very similar thermal transport behavior as a hypothetical isolated graphene monolayer, in general agreement with available experimental data [198, 199, 200]. Whereas even larger thermal conductivity should be expected for a monolayer than for a nanotube, I must consider that unlike the nanotube, a graphene monolayer is not self-supporting in vacuum. For all carbon allotropes considered here, I also find that the thermal conductivity decreases with increasing temperature in the range depicted in Figure 10.5.

Very interesting is the fact that once graphene layers are stacked in graphite, the inter-layer interactions quench the thermal conductivity of this system by nearly one order of magnitude. For the latter case of crystalline graphite, I also found my calculated thermal conductivity values to be confirmed by corresponding observations in the basal plane of highest-purity synthetic graphite [198, 199, 200] which are also reproduced in the figure. I would like to note that experimental data suggest that

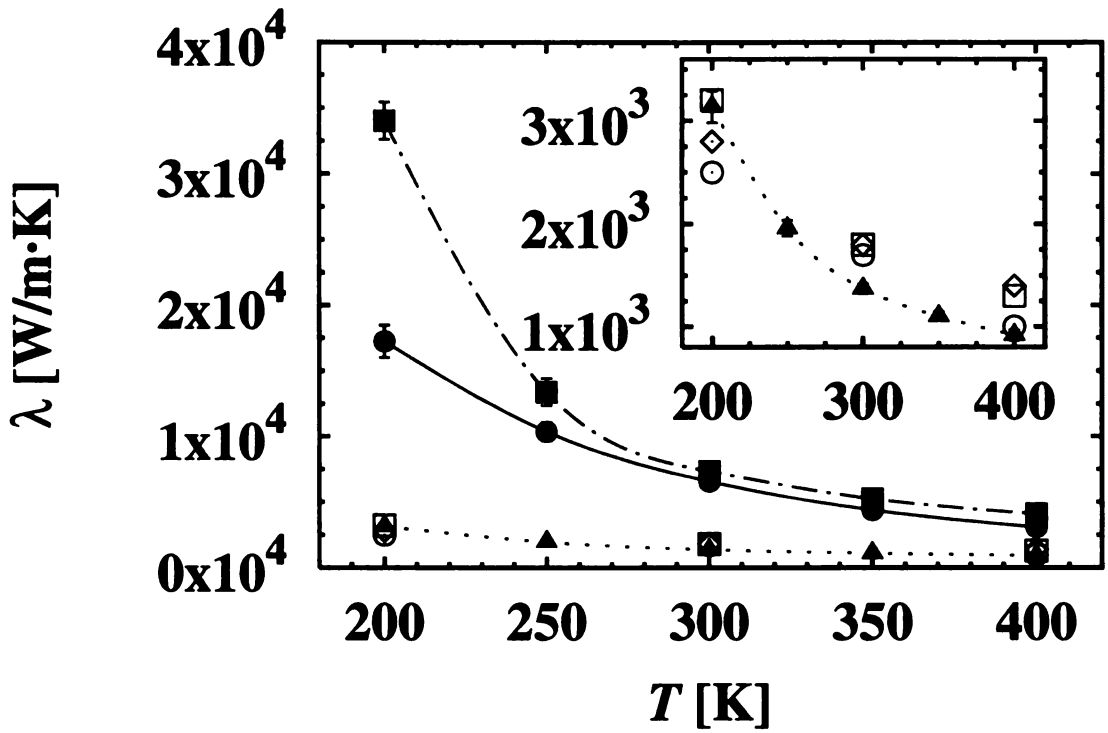

Figure 10.5: Thermal conductivity λ for a $(10, 10)$ carbon nanotube (solid line), in comparison to a constrained graphite monolayer (dash-dotted line), and the basal plane of AA graphite (dotted line) at temperatures between 200 K and 400 K. The inset reproduces the graphite data on an expanded scale. The calculated values (solid triangles) are compared to the experimental data of Refs. [198] (open circles), [199] (open diamonds), and [200] (open squares) for graphite.

the thermal conductivity in the basal plane of graphite peaks near 100 K, similar to my nanotube results.

10.4 Conclusions

Based on the above described difference in the conductivity between a graphene monolayer and graphite, I should expect a similar reduction of the thermal conductivity when a nanotube is brought into contact with other systems. This should occur when nanotubes form a bundle or rope, become nested in multi-wall nanotubes, or interact with other nanotubes in the "nanotube mat" of "bucky-paper" and could be verified experimentally. Consistent with my conjecture is the low value of $\lambda \approx 0.7$ W/m·K reported for the bulk nanotube mat at room temperature [186, 187].

In summary, I combined results of equilibrium and non-equilibrium molecular dynamics simulations with accurate carbon potentials to determine the thermal conductivity λ of carbon nanotubes and its dependence on temperature. My results suggest an unusually high value $\lambda \approx 6,600$ W/m·K for an isolated $(10, 10)$ nanotube at room temperature, comparable to the thermal conductivity of a hypothetical isolated graphene monolayer or graphite. I believe that these high values of λ are associated with the large phonon mean free paths in these systems. My numerical data indicate that in presence of inter-layer coupling in graphite and related systems, the thermal conductivity is reduced significantly to fall into the experimentally observed value range.

Chapter 11

Magnetism in All-Carbon Structures with Negative Gaussian Curvature

The following discussion of magnetism in nanostructured carbon materials follows that presented in Reference [201].

11.1 Magnetism in carbon

The discovery of new nanostructured carbon phases, including fullerenes [94] and nanotubes [11], has opened a new era in materials science. Minute changes in the spatial arrangement of carbon atoms can profoundly alter the electronic properties of these systems from a semiconductor to a metal or superconductor [24, 25, 26, 43]. One could expect that structural rearrangements might also significantly change the magnetic properties of all-carbon allotropes from their known diamagnetic behaviour. Only recently, a weakly magnetic all-carbon structure has been reported, formed under high-pressure and high-temperature conditions, consisting of rhombohedrally polymerized C_{60} molecules [202]. Other experimental observations suggest the occur-

rence of ferromagnetism in a semiconducting nanostructured carbon foam with a low mass density [203]. As I show in the following, the unexpected magnetic behaviour of all-carbon systems can be quantitatively interpreted using spin-polarized *ab initio* calculations. These results suggest that unpaired spins are introduced by sterically protected carbon radicals, which are immobilised in the non-alternant aromatic system of sp^2 bonded carbon with negative Gaussian curvature. This new mechanism to generate unpaired spins in semiconductors may find a useful application in the emerging field of spintronics.

11.2 Computational method

Here I present results for electronic and magnetic properties of an sp^2 bonded all-carbon nanostructure, consisting of a nanotube junction that is structurally related to schwarzite [204, 205, 206, 207]. These results have been obtained in collaboration with theory team members, who are listed as co-authors in Reference [201]. The tetrapod system, depicted in Figure 11.1(a), is a possible building block of the recently synthesized nanostructured carbon foam [208, 209, 203]. Our most striking finding is that of a ground state with a net magnetic moment. We find the origin of magnetism in this system to be different from previous reports [210, 211, 212], which related the spin polarization at a graphite edge to the presence of undercoordinated carbon atoms. Our calculations suggest that unpaired spins may also be introduced by carbon radicals, not only by undercoordinated carbon atoms. In the structure we propose, the radicals are sterically protected in a non-alternant aromatic system of carbons with negative Gaussian curvature.

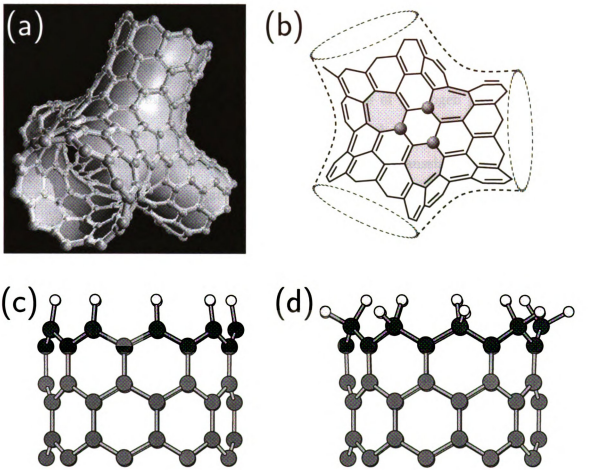

Figure 11.1: (a) The structure of a carbon tetrapod, the building block of schwarzite. The four extremities consist of $(9,0)$ nanotubes with a zigzag edge. (b) Introduction of trivalent carbon radicals, emphasized by the gray spheres, in the aromatic system of the otherwise tetravalent carbon atoms in the tetrapod core. The radicals are associated with heptagons, indicated by gray shading. The structure of an (c) sp^2- and (d) sp^3-terminated $(9,0)$ nanotube, with the smaller spheres indicating the hydrogen atoms.

11.2.1 The tetrapod as a possible building block of carbon nanofoam

Our electronic and magnetic structure calculations are based on the 'tetrapod' geometry shown in Figure 11.1 (a). The core, depicted in Figure 11.1 (b), consists of the warped sp^2 bonded building block of the Plumber's Nightmare structure [205]. It is formed by a network of hexagons and heptagons only, and connected to four $(9,0)$ nanotube extremities. Depending on the degree of hydrogen passivation, the exposed nanotube edges are terminated by sp^2 or sp^3 carbon atoms [213]. In this type of schwarzite-related structures, tubular segments of zero Gaussian curvature coexist with saddle-like regions of negative Gaussian curvature. We expect that a range of schwarzite-like building blocks similar to ours could be cross-linked to form a foam structure with a very low mass density, and carry a magnetic moment.

11.3 Unpaired spins in a carbon tetrapod

We calculate the electronic structure of different tetrapods using the density functional theory within the local spin density approximation (LSDA), employing the Ceperley-Alder exchange-correlation functional for the local spin density [126, 127] and *ab initio* pseudopotentials [128, 214]. To facilitate the numerical treatment of very large aggregates containing hundreds of atoms within LSDA, we make use of our recently developed approach based on an atom-centered numerical basis set [215], proven to describe correctly similar carbon systems [216]. We use Pulay corrections [217] to the Hellman-Feynman forces during structure optimization.

To discriminate between the effect of the sp^2 core region and the edge region in our magnetic structure calculations, we have considered hydrogen terminated C_{264} and C_{336} clusters with the same core structure, but a different length of the nanotube extremities. We assume that the edge of these extremities may be terminated in three

different ways. Besides the bare, unterminated edge, we consider an sp^2 termination by one hydrogen atom per edge atom, shown in Figure 11.1(c). In the sp^3 terminated structure shown in Figure 11.1(d), each carbon edge atom is connected to two hydrogen atoms. The interface between the sp^3 edge atoms and the sp^2 atoms of the nanotube is analogous to that found in diamond-graphite hybrid structures [218]. In the following, we disregard structures with a bare edge, since they are likely to be passivated fast under experimental conditions due to their high reactivity.

The electronic density of states for the sp^2 terminated tetrapod is presented in Figure 11.2(a). The projection of the total density of states onto the 192 carbon atoms in the core region, including twelve heptagon rings, is shown by the solid line, and that of the 72 atoms at the edges by the dashed line. We focus on a 1 eV wide energy window around the Fermi level, which determines the magnetic behavior, since electrons with higher binding energies are all paired. Artificial level broadening was used only in the figure, for the sake of visual clarity; no broadening has been applied during the self-consistent calculations. The density of states indicates the presence of twelve unpaired spins in this sp^2-terminated geometry. The decomposition of the density of states suggests that eight of the twelve spins are strongly localized at the zigzag edges, with two unpaired spins at each edge.

Presence of the remaining four unpaired spin states, which are unrelated to the edge states, is independent of the length of the nanotube extremities. A detailed analysis revealed that the electronic states associated with the majority spin are not localized, but rather spread out across the entire cluster, as shown in Figure 11.3(a). We found that the exchange splitting of the four states decreases with increasing nanotube length. This can be understood in terms of the exchange interaction between two electrons, which occupy the same region. The origin of the exchange splitting is the Coulomb repulsion between these electrons, which decreases as the region grows.

To clarify the nature of the unpaired electrons near the tetrapod edges, we per-

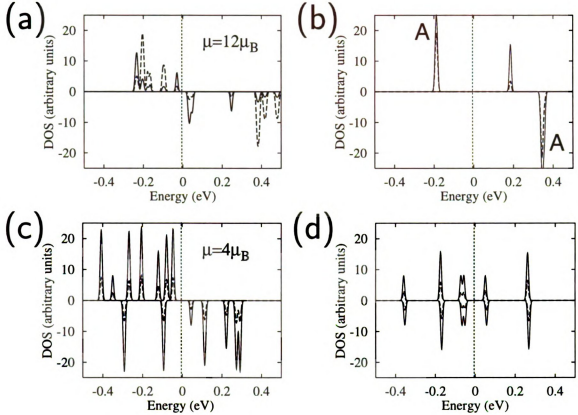

Figure 11.2: Spin-resolved electronic densities of states of carbon nanostructures related to Figure 11.1, with the majority spins represented in the upper panels and the minority spins in the lower panels. (a) Density of states of the C_{264} tetrapod of Figure 11.1(a). The solid line represents the projection of the density of states onto the 192 core carbon atoms. The dashed line represents that of the 72 carbon atoms at the zigzag edges. (b) Electronic density of states of a 126-atom segment of an sp^2 terminated $(9,0)$ nanotube, shown in Figure 11.1(c). The solid line represents the density of states of all the carbon atoms, and the dashed line its projection onto the 36 carbon atoms at the zigzag edge. The states denoted by "A" are doubly degenerate and localized at the edge. The counterparts of (a) and (b) for sp^3 terminated structures are shown in (c) for the C_{264} tetrapod and in (d) for the $(9,0)$ nanotube segment. The discrete level spectrum has been convoluted with a Gaussian with a full width at half maximum of 0.012 eV. The Fermi level lies at $E = 0$.

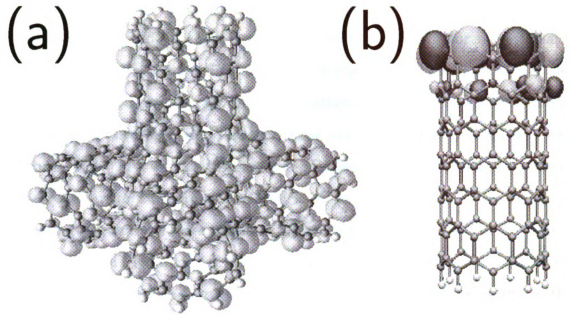

Figure 11.3: (a) Charge density associated with the four unpaired spins, which are unrelated to the edge states in an sp^2 terminated tetrapod. (b) Wave function of a spin-polarized edge state in an sp^2 terminated $(9,0)$ nanotube. We use color shading to represent the phase of the wave function.

formed an independent calculation for the $(9,0)$ nanotube with the same edge geometry. Similar to our results for the tetrapod in Figure 11.2(a), the spin-resolved density of states of the nanotube, shown in Figure 11.2(b), indicates the presence of two unpaired spins per zigzag edge. Character analysis suggests that the states in the narrow energy window used are mainly carbon-based, with only a negligible contribution from hydrogen. We show the total density of states of all carbon atoms by the solid line, and that of the carbon edge atoms by the dashed line in Figure 11.2(b). The spin-polarized electrons occupy doubly degenerate π^* states at each edge, labeled by **A**. We find one of the edge state wave functions, displayed in Figure 11.3(b), to be symmetric and the other one antisymmetric with respect to a mirror plane of the nanotube. The exchange splitting of about 0.5 eV, separating the spin-up from the spin-down edge states, is comparable to that found by *ab initio* plane-wave calculations for doped C-BN composite nanotubes [219].

To study the effect of edge termination on the net magnetic moment of the tetrapod, we compared our above electronic structure calculations for sp^2 terminated structures to those showing sp^3 termination. In Figure 11.2(c) we present the electronic density of states for the sp^3 terminated tetrapod. To model an sp^3 termination, we attached two hydrogen atoms instead of one to each carbon edge atom, as shown in Figure 11.1(d). As we noted earlier, hydrogen-induced states within this bonding geometry occur far away from the Fermi level, in analogy to the σ-states of sp^3-bonded carbon, and do not interfere with carbon-related states within the narrow energy window in Figure 11.2(c). Also, the localized π states, which we found at the edge of the sp^2 terminated structure, vanish in the sp^3 bonding geometry. In this case, we do not expect any unpaired spins associated with the sp^3 edge atoms. The projection of the density of states onto the inner 192 carbon atoms of the tetrapod is represented by the solid line, and that of the 72 edge atoms by the dashed line in Figure 11.2(c). In the sp^3 terminated tetrapod, we find four unpaired spins, similar to the sp^2 terminated tetrapod, where we identified four unpaired spins, which were unrelated to the edge states.

To confirm the absence of spin polarization at the sp^3 terminated edges, we show in Figure 11.2(d) the density of states of an sp^3 terminated $(9,0)$ nanotube, as a counterpart to results shown in Figure 11.2(b). Our spin-resolved density of states confirms that the sp^3 edge should not be spin polarized, in stark contrast to our results for the sp^2 terminated edge. These results agree with those reported for sp^2 and sp^3 terminated graphene strips [213].

Our findings raise several intriguing questions. The first important question is, what distinguishes the magnetic structure, shown in Figure 11.1(a), from other carbon structures, which are nonmagnetic, or systems, where magnetism arises due to undercoordinated edge atoms. Equally important is to find the reason for the occurrence of the spin polarization and its apparent robustness with respect to selected struc-

tural changes. To answer these questions, we calculated the magnetic ground state of numerous other sp^2 bonded carbon structures, including tetrapods terminated by C_{60}-derived caps, fullerenes in the size range from C_{20} to C_{240}, nanotube Y-junctions, and schwarzite-related structures with negative Gaussian curvature, containing octagons.

In our calculations, we found the number of unpaired spins not to be affected by changing size and boundary shape of the tetrapod, but to depend sensitively on the bonding topology. Setting aside the role of unsaturated graphitic edges in magnetism, which has been discussed before [210, 211, 212, 213], we found the presence of higher polygons, introducing a negative Gaussian curvature, to be a necessary condition for a magnetic ground state. To investigate a possible conjecture that negative curvature is also a sufficient condition to establish spin polarization, we calculated the electronic ground state of a tetrapod, where all four extremities were terminated by C_{60}-derived caps. Our finding of an energy gap of 0.34 eV between the highest occupied and the lowest unoccupied state in this structure, which excludes the possibility of a Fermi instability, proved this conjecture incorrect.

11.4 Magnetism due to sterically protected radicals in nanostructured carbon

The only viable explanation for the occurrence of magnetism in an all-carbon structure is the introduction and stabilization of carbon radicals. The occurrence of radicals, which can introduce an unpaired spin, is directly related to the possibility of pairing all valence electrons in covalent bonds. No radicals should be expected to occur if bonds in the system can be assigned in a way that would keep all carbon atoms tetravalent. In a graphitic structure, each tetravalent carbon atom is connected to three neighbors by one double and two single bonds. In such a case, all electrons should be paired and the structure should be diamagnetic. This is the case in C_{60}

and other fullerenes, where all carbon atoms are kept tetravalent by associating single bonds with the edges of pentagons. Also in a planar graphene sheet or an infinite nanotube, all carbon atoms are equivalent and tetravalent.

Failure to find a global bonding scheme, where each carbon atom is associated with one double and two single bonds, leads to the introduction of radicals due to a frustration in the electronic system. As we expand on below, this is the case in the tetrapod structure of Figure 11.1(a), where twelve trivalent carbon radicals are introduced as a consequence of inserting twelve heptagons in the otherwise alternant aromatic system of the graphitic honeycomb lattice. These trivalent carbons, emphasized in Figure 11.1(b) by the gray spheres, are the source of spin polarization. In the structure discussed here, these radicals are sterically protected within the system of 'single' and 'double' bonds imposed by the tetrapod topology, and occur in groups of three.

This conclusion can be reached by analyzing the bonding scheme in the sp^3 terminated tetrapod. The system of single and double bonds, shown in Figure 11.1(b), follows the bonding at the edge of the terminating nanotube. Since two valence electrons of the terminating carbon atoms are paired with those of hydrogen, all bonds along the zigzag edge must be single bonds. To keep carbon atoms at the edge tetravalent, adjacent bonds in the axial direction must be double bonds, as shown in Figure 11.1(b). Following this scheme into the core region of the structure necessarily leads to the above mentioned frustration, which leaves several sites, namely the trivalent carbon radicals with a lone electron, connected to their neighbors by only three single bonds. Following this reasoning, we can thus correlate the occurrence of a magnetic moment in a carbon nanostructure with the bonding topology.

The lone electrons need not be localized at the radical sites, but rather gain energy by delocalizing across the entire structure, as shown in Figure 11.3(a). We find the radicals to form groups of three in the tetrapods. Assuming that two of the

three spins are paired, each group of three radicals should contribute one unpaired spin to the structure. With four groups of radicals per tetrapod, we would expect four unpaired spins in total, in agreement with our spin density functional calculation. With increasing size of the nanostructure, as the unpaired spins delocalize over a larger area, the exchange splitting should gradually decrease to zero, thus eventually eliminating magnetism at nonzero temperatures.

Stabilization of carbon radicals by steric protection has been known since the synthesis of triphenylmethyl in 1900 by Gomberg [220]. Radicals such as perinaphthenyl (or phenalenyl) have even been investigated as potential molecular conductors by Haddon [221]. Whereas sterically unshielded carbon-based radicals has been reported recently in organic systems [222], our study is the first report to our knowledge that identifies carbon radicals in an undoped all-carbon structure with no apparent exposed edges. We should emphasize that the magnetism found in this study is caused by the presence of sterically protected radicals within nanometer-sized conducting segments of sp^2 carbon. It could also occur in other nanostructured solids, which may be different from the tetrapod structure discussed here. We believe this to be a general phenomenon, the discovery of which may strongly influence the emerging field of spintronics.

11.5 Summary

In summary, we studied several sp^2-bonded carbon nanostructures and identified a system of unpaired electrons that is distinct from the spin polarized states at the zigzag edge or dangling-bond states. Our spin density functional calculations for the tetrapod motif, which contains negatively curved graphitic surfaces, indicate the presence of four unpaired spins in the electronic ground state. This magnetic behavior originates in the presence of trivalent carbon radicals, which are introduced and

sterically stabilized within the aromatic system of the otherwise tetravalent carbon atoms in the core of the tetrapod structure. We expect a similar type of magnetism to occur in other graphitic structures with a negative Gaussian curvature.

BIBLIOGRAPHY

[1] M. Dresselhaus, G. Dresselhaus, and P. Eklund, *Science of Fullerenes and Carbon Nanotubes*, Academic Press, San Diego, 1996.

[2] R. Saito, G. Dresselhaus, and M. Dresselhaus, *Physical Properties of Carbon Nanotubes*, Imperial College Press, 1998.

[3] P. R. von Schleyer, *A simple preparation of adamantane*, J. Am. Chem. Soc. **79**, 3292 (1957).

[4] W. H. Bragg and W. L. Bragg, Nature **91**, 554 (1913).

[5] C. Cupas, P. R. von Schleyer, and D. J. Trecker, *Congressane*, J. Am. Chem. Soc. **87**, 917 (1965).

[6] V. Z. W. Jr., P. R. von Schleyer, G. J. Gleicher, and L. B. Rodewald, *Triamantane*, J. Am. Chem. Soc. **88**, 3862 (1966).

[7] D. Farcasiu, H. Bohm, and P. R. von Schleyer, *Stepwise Elaboration of Diamondoid Hydrocarbons - Synthesis of Diamantane From Adamantane*, J. Organic Chem. **42**, 96 (1977).

[8] W. Zhong, D. Tománek, and G. Bertsch, *Total Energy Calculations for Extremely Large Clusters: The Recursive Approach.*, Solid State Communications **86**, 607 (1993).

[9] Y.-K. Kwon, *Equilibrium Geometry and Electronic Properties of Nanostructures*, PhD thesis, Michigan State University, 1999.

[10] S. Berber, Y.-K. Kwon, and D. Tománek, *Electronic and Structural Propeties of Carbon Nanohorns*, Physical Review B **62**, R2291 (2000).

[11] S. Iijima, *Helical microtubules of graphitic carbon.*, Nature **354**, 56 (1991).

[12] T. Ebbesen, *Carbon Nanotubes - Review of nanotubes*, Physics Today **49**, 26 (1996).

[13] B. Yakobson and R. Smalley, *Fullerene nanotubes: $C_{1,000,000}$ and beyond*, American Scientific **85**, 324 (1997).

[14] S. Tans, M. H. Devoret, H. Dai, A. Thess, R. E. Smalley, L. Geerligs, and C. Dekker, *Individual single-wall carbon nanotubes as quantum wires*, Nature **386**, 474 (1997).

[15] M. Bockrath, D. H. Cobden, P. L. McEuen, N. G. Chopra, A. Zettl, A. Thess, and R. Smalley, *Single-electron transport in ropes of carbon nanotubes*, Science **275**, 1922 (1997).

[16] S. Tans, A. Verschueren, and C. Dekker, *Room temperature transistor based on a single carbon nanotube*, Nature **393**, 49 (1998).

[17] Y.-K. Kwon, D. Tománek, and S. Iijima, *"Bucky Shuttle" Memory Device: Synthetic Approach and Molecular Dynamics Simulations*, Physical Review Letters **82**, 1470 (1999).

[18] A. Rinzler, J. Hafner, P. Nikolaev, L. Lou, S. Kim, D. Tománek, P. Nordlander, D. Colbert, and R. Smalley, *Unraveling nanotubes - field-emission from an atomic wire*, Science **269**, 1550 (1995).

[19] W. de Heer, A. Châtelain, and D. Ugarte, *A carbon nanotube field-emission electron source*, Science **270**, 1179 (1995).

[20] L. Chernozatonskii, Y. Gulyaev, Z. Kosakovskaja, N. Sinitsyn, G. Torgashov, Y. Zakharchenko, E. Fedorov, and V. Valchuk, *Electron field-emission from nano-filament carbon-films*, Chemical Physics Letters **233**, 63 (1995).

[21] W. Choi, D. Chung, J. Kang, H. Kim, Y. Jin, I. Han, Y. Lee, J. Jung, N. Lee, G. Park, and J. Kim, *Fully sealed, high-brightness carbon-nanotube field-emission display*, Applied Physics Letters **75**, 3129 (1999).

[22] S. Iijima and T. Ichihashi, *Single-shell carbon nanotubes of 1-nm diameter SWnT growth, catalytic (Fe-Co)*, Nature **363**, 603 (1993).

[23] D. Bethune, C. Kiang, M. de Vries, G. Gorman, R. Savoy, J. Vazquez, and R. Beyers, *Cobalt-catalysed growth of carbon nanotubes with single-atomic-layer walls*, Nature **363**, 605 (1993).

[24] J. Mintmire, B. Dunlap, and C. White, *Are Fullerene tubulues metallic*, Physical Review Letters **68**, 631 (1992).

[25] R. Saito, M. Fujita, G. Dresselhaus, and M. Dresselhaus, *Electronic-structure of chiral graphene tubulues*, Applied Physics Letters **60**, 2204 (1992).

[26] N. Hamada, S. Sawada, and A. Oshiyama, *New one-dimensional conductor - graphitic microtubules*, Physical Review Letters **68**, 1579 (1992).

[27] J. Wildöer, L. Venema, A. Rinzler, R. Smalley, and C. Dekker, *Electronic structure of atomically resolved carbon nanotubes*, Nature **391**, 59 (1998).

[28] T. Odom, J.-L. Huang, P. Kim, and C. Lieber, *Atomic structure and electronic properties of single-walled carbon nanotubes*, Nature **391**, 62 (1998).

[29] W. Clauss, D. Bergeron, and A. Johnson, *Atomic resolution STM imaging of a twisted single-wall carbon nanotube*, Physical Review B **58**, R4266 (1998).

[30] D. Tománek, S. G. Louie, H. J. Mamin, D. W. Abraham, R. E. Thomson, E. Ganz, and J. Clarke, *Theory and observation of highly asymmetric atomic structure in scanning-tunneling-microscopy images of graphite*, Physical Review B **35**, 7790 (1987).

[31] D. Tománek and S. G. Louie, *First-principles calculation of highly asymmetric structure in scanning-tunneling-microscopy images of graphite. Uses orbital wave functions of carbon atoms in real space*, Physical Review B **37**, 8327 (1988).

[32] V. Meunier and P. Lambin, *Tight-Binding Computation of the STM Image of Bent Carbon Nanotubes*, Physical Review Letters **81**, 5588 (1998).

[33] A. Rubio, *Spectroscopic properties and STM images of carbon nanotubes*, Applied Physics A **68**, 275 (1999).

[34] V. Meunier, P. Senet, and P. Lambin, *Scanning tunneling spectroscopy signature of finite-size and connected nanotubes: A tight-binding study*, Physical Review B **60**, 7792 (1999).

[35] C. Kane and E. Mele, *Broken symmetries in scanning tunneling images of carbon nanotubes*, Physical Review B **59**, R12759 (1999).

[36] D. Carroll, P. Redlich, P. Ajayan, J. Charlier, X. Blase, A. DeVita, and R. Car, *Electronic structure and localized states at carbon nanotubes*, Physical Review Letters **78**, 2811 (1997).

[37] P. Kim, T. W. Odom, J.-L. Huang, and C. M. Lieber, *Electronic Density of States of Atomically Resolved Single-Walled Carbon Nanotubes: Van Hove Singularities and End States*, Physical Review Letters **82**, 1225 (1999).

[38] M. Ge and K. Sattler, *Observation of fullerene cones*, Chemical Physics Letters **220**, 192 (1994).

[39] A. Krishnan, E. Dujardin, M. Treacy, J. Hugdahl, S. Lynum, and T. Ebbesen, *Graphitic cones and the nucleation of curved carbon surfaces*, Nature **388**, 451 (1997).

[40] S. Iijima, T. Ichihashi, and Y. Ando, *Pentagons, heptagons and negative curvature in graphite microtubule growth - multi-wall cones terminating CNTs*, Nature **356**, 776 (1992).

[41] S. Iijima, M. Yudasaka, R. Yamada, S. Bandow, K. Suenaga, F. Kokai, and K. Takahashi, *Nano-aggregates of single-walled graphitic carbon nano-horns*, Chemical Physics Letters **309**, 165 (1999).

[42] D. Tománek and M. A. Schluter, *Growth regimes of carbon clusters*, Physical Review Letters **67**, 2331 (1991).

[43] M. Schluter, M. Lannoo, M. Needels, G. Baraff, and D. Tománek, *Electro-Phonon Coupling and Superconductivity in Alkali-Intercalated C_{60} Solid*, Physical Review Letters **68**, 526 (1992).

[44] Y.-K. Kwon, S. Saito, and D. Tománek, *Effect of inter-tube coupling on the electronic structure of carbon nanotube ropes*, Physical Review B **58**, R13314 (1998).

[45] Y.-K. Kwon, D. Tománek, Y. H. Lee, K. H. Lee, and S. Saito, *Do carbon nanotubes spin when bundled?*, J. Mater. Res. **13**, 2363 (1998).

[46] Y.-K. Kwon and D. Tománek, *Electronic and structural properties of multiwall carbon nanotubes*, Physical Review B **58**, R16001 (1998).

[47] S. Sanvito, Y.-K. Kwon, D. Tománek, and C. J. Lambert, *Fractional quantum conductance in carbon nanotubes*, Physical Review Letters **84**, 1974 (2000).

[48] S. Kim and D. Tománek, *Melting the fullerenes: A molecular dynamics study*, Physical Review Letters **72**, 2418 (1994).

[49] Y.-K. Kwon, Y. H. Lee, S. G. Kim, P. Jund, D. Tománek, and R. E. Smalley, *Morphology and Stability of Growing Multi-Wall Carbon Nanotubes*, Physical Review Letters **79**, 2065 (1997).

[50] P. Lambin, A. Fonseca, J. Vigneron, J. Nagy, and A. Lucas, *Structural and electronic properties of bent nanotubes*, Chemical Physics Letters **245**, 85 (1995).

[51] G. Treboux, P. Lapstun, and K. Silverbrook, *An intrinsic carbon nanotube heterojunction diode*, Journal of Physical Chemistry B **103**, 1871 (1999).

[52] V. Meunier, L. Henrard, and P. Lambin, *Energetics of bent carbon nanotubes*, Physical Review B **57**, 2586 (1998).

[53] M. Allen and D. Tildesley, *Computer Simulation of Liquids*, Clarendon Press, Oxford, 1987.

[54] S. Nosé, *A Molecular-Dynamics method for simulations in The Canonical Ensemble*, Molecular Physics **52**, 255 (1984).

[55] W. Hoover, *Canonical Dynamics - Equilibrium Phase-Space Distributions*, Physical Review A **31**, 1695 (1985).

[56] S. Berber, Y.-K. Kwon, and D. Tománek, *Microscopic Formation Mechanism of Nanotube Peapods*, Physical Review Letters **88**, 185502 (2002).

[57] B. Smith, M. Monthioux, and D. Luzzi, *Encapsulated C_{60} in carbon nanotubes*, Nature **396**, 323 (1998).

[58] B. Burteaux, A. Claye, B. Smith, M. Monthioux, D. Luzzi, and J. Fischer, *Abundance of encapsulated C_{60} in single-wall carbon nanotubes.*, Chemical Physics Letters **310**, 21 (1999).

[59] B. Smith, M. Monthioux, and D. Luzzi, *Carbon nanotube encapsulated fullerenes: a unique class of hybrid materials*, Chemical Physics Letters **315**, 31 (1999).

[60] B. W. Smith and D. E. Luzzi, *Formation mechanism of fullerene peapods and coaxial tubes: a path to large scale synthesis*, Chemical Physics Letters **321**, 169 (2000).

[61] K. Hirahara, K. Suenaga, S. Bandow, H. Kato, T. Okazaki, H. Shinohara, and S. Iijima, *One-Dimensional Metallofullerene Crystal Generated Inside Single-Walled Carbon Nanotubes*, Physical Review Letters **85**, 5384 (2000).

[62] R. Dunin-Borkowski, J. Hutchinson, K. Coleman, V. Williams, J. Claridge, A. York, C. Xu, S. Bailey, G. Brown, S. Friedrichs, and M. Green, *The size distribution, imaging and obstructing properties of C-60 and higher fullerenes formed within arc-grown single walled carbon nanotubes*, Chemical Physics Letters **316**, 191 (2000).

[63] R. F. Service, *Nanotube 'Peapods' Show Electrifying Promise*, Science **292**, 45 (2001).

[64] L. A. Girifalco, M. Hodak, and R. S. Lee, *Carbon nanotubes, buckyballs, ropes, and a universal graphitic potential*, Physical Review B **62**, 13104 (2000).

[65] M. Hodak and L. A. Girifalco, *Quasi-one-dimensional system of molecules inside carbon nanotubes. Exact solution for the lattice gas model and its application to fullerene-filled nanotube*, Physical Review B **64**, 35407 (2001).

[66] M. Monthioux, B. W. Smith, B. Burteaux, A. Claye, J. E. Fischer, and D. E. Luzzi, *Sensitivity of single-wall carbon nanotubes to chemical processing: an electron microscopy investigation*, Carbon **39**, 1251 (2001).

[67] S. Okada, S. Saito, and A. Oshiyama, *Energetics and Electronic Structures of Encapsulated C60 in a Carbon Nanotube*, Physical Review Letters **86**, 3835 (2001).

[68] S. Bandow, M. Takizawa, K. Hirahara, M. Yudasaka, and S. Iijima, *Raman scattering study of double-wall carbon nanotubes derived from the chains of fullerenes in single-wall carbon nanotubes*, Chemical Physics Letters **337**, 48 (2001).

[69] S. Han, M. Yoon, S. Berber, N. Park, E. Osawa, J. Ihm, and D. Tománek, *Microscopic Mechanism of Fullerene Fusion*, Physical Review Letters .

[70] M. Yoon, S. Berber, and D. Tománek, *Energetics and Packing of Fullerenes in Nanotube Peapods*, Submitted to Physical Review Letters .

[71] G. C. McIntosh, M. Yoon, S. Berber, and D. Tománek, *Diamondoids as Building Blocks of Functional Nanostructures*, Physical Review B (2004).

[72] B. Smith, D. Luzzi, and Y. Achiba, *Tumbling atoms and evidence for charge transfer in* $La^{-2}@C_{80}@SWNT$, Chemical Physics Letters **331**, 137 (2000).

[73] D. L. Dorset and J. R. Fryer, *Electron Crystallographic Analysis of Sublimed* C_{70} *Buckminsterfullerene*, Journal of Physical Chemistry B **101**, 3968 (1997).

[74] H. Kawada, Y. Fujii, H. Nakao, Y. Murakami, T. Watanuki, H. Suematsu, K. Kikuchi, Y. Achiba, and I. Ikemoto, *Structural aspects of* C_{82} *and* C_{76} *crystals studied by x-ray diffraction*, Physical Review B **51**, 8723 (1995).

[75] Y. Saito, T. Yoshikawa, N. Fujimoto, and H. Shinohara, C_{84} *thin films grown epitaxially on mica*, Physical Review B **48**, 9182 (1993).

[76] R. Beyers, C. H. Kiang, R. D. Johnson, J. R. Salem, M. S. Devries, C. S. Yannoni, D. S. Bethune, H. C. Dorn, P. Burbank, K. Harich, and S. Stevenson, *Preparation and structure of crystals of the metallofullerenes* $SC_2@C_{84}$, Nature **370**, 196 (1994).

[77] K. Hirahara, S. Bandow, K. Suenaga, H. Kato, T. Okazaki, H. Shinohara, and S. Ijima, *Electron diffraction study of one-dimensional crystals of fullerenes*, Physical Review B **64**, 115420 (2001).

[78] B. Smith, R. M. Russo, S. B. Chikkannanavar, and D. E. Luzzi, *High-yield synthesis and one-dimensional structure of C60 encapsulated in single-wall carbon nanotubes*, Journal of Applied Physics **91**, 9333 (2002).

[79] H. Kuzmany, R. Pfeiffer, C. Kramberger, T. Pichler, X. Liu, M. Knupfer, J. Fink, H. Kataura, Y. Achiba, B. Smith, and D. Luzzi, *Analysis of the concentration of C60 fullerenes in single wall carbon nanotubes*, Applied Physics A **76**, 449 (2003).

[80] K. P. Meletov, S. Assimopoulos, I. Tsilija, G. A. Kourouklis, J. Arvanitidis, S. Ves, B. Sundqvist, and T. Wagberg, *High-pressure-induced metastable phase in tetragonal 2D polymeric* C_{60}, Chemical Physics Letters **341**, 435 (2001).

[81] V. D. Blank, S. G. Buga, N. R. Serebryanaya, V. N. Denisov, G. A. Dubitsky, A. N. Ivlev, B. N. Mavrin, and M. Y. Popov, *Ultrahard and superhard carbon phases produced from* C_{60} *by heating at high-pressure-structural and Raman studies*, Physical Letters A **205**, 208 (1995).

[82] M. Hodak and L. Girifalco, *Cohesive properties of fullerene-filled nanotube ropes*, Chemical Physics Letters **363**, 93 (2002).

[83] M. Hodak and L. Girifalco, *Ordered phases of fullerene molecules formed inside carbon nanotubes*, Physical Review B **67**, 075419 (2003).

[84] H. Ulbricht, G. Moos, and T. Hertel, *Interaction of C60 with carbon nanotubes and graphite*, Physical Review Letters **90**, 095501 (2003).

[85] Y. Wang, D. Tománek, and G. F. Bertsch, *Stiffness of a solid composed of C60 clusters*, Physical Review B **44**, R6562 (1991).

[86] A. J. Stone and D. J. Wales, *Theoretical studies of icosahedral C_{60} and some related species*, Chemical Physics Letters **128**, 501 (1986).

[87] B. R. Eggen, M. I. Heggie, G. Jungnickel, C. D. Latham, R. Jones, and P. R. Briddon, *Autocatalysis during fullerene growth*, Science **272**, 87 (1996).

[88] Z. Slanina, X. Zhao, F. Uhlik, M. Ozawa, and E. Osawa, *Computational Modelling of the Elemental Catalysis in the Stone-Wales Fullerene Rearrangements*, Journal of Organometal. Chemistry **599**, 57 (2000).

[89] F. Banhart, *Irradiation effects in carbon nanostructures*, Rep. Prog. Phys. **62**, 1181 (1999).

[90] J. G. Lavin, S. Subramoney, S. B. R. S. Ruoff, and D. Tomanek, *Scrolls and nested tubes in multiwall carbon nanotubes*, Carbon **40**, 1123 (2002).

[91] K. Umemoto, S. Saito, S. Berber, and D. Tománek, *Carbon foam: Spanning the phase space between graphite and diamond*, Physical Review B **64**, 193409 (2001).

[92] D. Tománek, K. Umemoto, S. Saito, and S. Berber, *Hierarchical Assembly of Nanostructured Carbon Foam*, Molecular Crystals and Liquid Crystals **386**, 189 (2002).

[93] S. Berber and D. Tománek, *Stability differences and conversion mechanism between nanotubes and scrolls*, Physical Review B , BR (2004).

[94] H. W. Kroto, J. R. Heath, S. C. O'Brien, R. F. Curl, and R. E. Smalley, *C60: Buckminsterfullerene*, Nature **318**, 162 (1985).

[95] D. Ugarte, *Curling and closure of graphitic networks under electron-beam irradiation*, Nature **359**, 707 (1992).

[96] X. F. Zhang, X. B. Zhang, G. V. Tendeloo, S. Amelinckx, M. O. de Beeck, and J. V. Landuyt, *Carbon nanotubes - their formation process and observation by electron-microscopy*, Journal of Crystal Growth **130**, 368 (1993).

[97] O. Zhou, R. M. Fleming, D. W. Murphy, C. H. Chen, R. C. Haddon, A. P. Ramirez, and S. H. Glarum, *Defects in Carbon Nanostructures*, Science **263**, 1744 (1994).

[98] S. Bandow, *Radial thermal expansion of purified multiwall carbon nanotubes measured by X-ray diffraction*, Japanese Journal of Applied Physics: Part 2-Letters **36**, L1403 (1997).

[99] V. Z. Mordkovich, M. Baxendale, S. Yoshimura, and R. P. H. Chang, *Intercalation into carbon nanotubes*, Carbon **34**, 1301 (1996).

[100] F. Leroux, K. Metenier, S. Gautier, E. Frackowiak, S. Bonnamy, and F. Beguin, *Electrochemical insertion of lithium in catalytic multi-walled carbon nanotubes*, Journal of Power Sources **82**, 317 (1999).

[101] E. Frackowiak, K. Metenier, V. Bertagna, and F. Beguin, *Supercapacitor electrodes from multiwalled carbon nanotubes*, Applied Physics Letters **77**, 2421 (2000).

[102] F. Krumeich, H. J. Muhr, M. Niederberger, F. Bieri, and R. Nesper, *The cross-sectional structure of vanadium oxide nanotubes studied by transmission electron microscopy and electron spectroscopic imaging*, Zeitschrift Fur Anorganische und Allgemeine Chemie **626**, 2208 (2000).

[103] S. Amelinckx, D. Bernearts, X. B. Zhang, G. V. Tendeloo, and J. V. Landuyt, *A structure model and growth-mechanism for multishell carbon nanotubes*, Science **267**, 1334 (1995).

[104] D. Bernaerts, A. A. Lucas, and S. Amelinckx, *On a peculiar contrast effect associated with carbon nanotubes*, Philosophical Magazine A **76**, 267 (1997).

[105] D. Bernaerts, S. Amelinckx, G. V. Tendeloo, and J. V. Landuyt, *Microstructure and formation mechanism of cylindrical and conical scrolls of the misfit layer compounds* $PbNb_nS_{2n+1}$, Journal of Crystal Growth **172**, 433 (1997).

[106] Y. Maniwa, R. Fujiwara, H. Kira, E. N. H. Tou, M. Takata, M. Sakata, A. Fujiwara, X. L. Z. S. Iijima, and Y. Ando, *Multiwalled carbon nanotubes grown in hydrogen atmosphere: An x-ray diffraction study*, Physical Review B **64**, 073105 (2001).

[107] A. Love, *A Treatise on the Mathematical Theory of Elasticity*, Dover Publications, New York, 1944.

[108] D. Tománek, W. Zhong, and E. Krastev, *Stability of multishell fullerenes*, Physical Review B **48**, 15461 (1993).

[109] D. Robertson, D. Brenner, and J. Mintmire, *Energetics of nanoscale graphitic tubules*, Physical Review B **45**, 12592 (1992).

[110] V. P. Dravid, X. Lin, Y. Wang, X. K. Wang, A. Yee, J. B. Ketterson, and R. H. P. Chang, *Buckytubes and derivatives - their growth and implications for buckyball formation*, Science **259**, 1601 (1993).

[111] Y. Miyamoto, S. Berber, M. Yoon, A. Rubio, and D. Tománek, *Onset of nanotube decay under extreme thermal and electronic excitations*, Physica B **323**, 78 (2002).

[112] Y. Miyamoto, S. Berber, M. Yoon, A. Rubio, and D. Tománek, *Reconstruction of Defective Carbon Nanotubes Induced by Electronic Excitations*, Submitted to Physical Review B (2004).

[113] P. Ball, *Designing the molecular world*, Princeton University Press, Princeton, 1994.

[114] P. C. Collins, M. S. Arnold, and P. Avouris, *Engineering carbon nanotubes and nanotube circuits using electrical breakdown*, Science **292**, 706 (2001).

[115] J. Appenzeller, R. Martel, V. Derycke, M. Radosavjevic, S. Wind, D. Neumayer, and P. Avouris, *Carbon nanotubes as potential building blocks for future nanoelectronics*, Microelectronic Engineering **64**, 391 (2002).

[116] R. Martel, V. Derycke, C. Lavoie, J. Appenzeller, K. K. Chan, J. Tersoff, and P. Avouris, *Ambipolar electrical transport in semiconducting single-wall carbon nanotubes*, Physical Review Letters **87**, 256805 (2001).

[117] M. Igami, T. Nakanishi, and T. Ando, *Conductance of carbon nanotubes with a vacancy*, Journal of Physical Society of Japan **68**, 716 (1999).

[118] H. J. Choi, J. Ihm, S. G. Louie, and M. L. Cohen, *Defects, quasibound states, and quantum conductance in metallic carbon nanotubes*, Physical Review Letters **84**, 2917 (2000).

[119] P. E. Blöchl and J. H. Stathis, *Hydrogen Electrochemistry and Stress-Induced Leakage Current in Silica*, Physical Review Letters **83**, 372 (1999).

[120] A. Yokozawa and Y. Miyamoto, *Hydrogen dynamics in SiO_2 triggered by electronic excitations*, Journal of Applied Physics **88**, 4542 (2000).

[121] O. Sugino and Y. Miyamoto, *Density functional approach to electron dynamics: Stable simulation under a self-consistent field*, Physical Review B **59**, 2579 (1999).

[122] O. Sugino and Y. Miyamoto, *Density-functional approach to electron dynamics: Stable simulation under a self-consistent field (vol 59, pg 2579, 1999)*, Physical Review B **66**, 89901 (2002).

[123] L. C. Qin, X. L. Zhao, K. Hirahara, Y. Miyamoto, Y. Ando, and S. Iijima, *Materials science - The smallest carbon nanotube*, Nature **408**, 50 (2000).

[124] N. Wang, Z. K. Tang, G. D. Li, and J. S. Chen, *Materials science - Single-walled 4 angstrom carbon nanotube arrays*, Nature **408**, 50 (2000).

[125] C. Ronchi, R. Beukers, H. Heinz, J. P. Hiernaut, and R. Selfslag, *Graphite Melting under Laser-Pulse Heating*, International Journal of Thermophysics **13**, 107 (1992).

[126] D. M. Ceperley and B. J. Alder, *Ground-state of the electron-gas by a stochastic method*, Physical Review Letters **45**, 566 (1980).

[127] J. P. Perdew and A. Zunger, *Self-interaction correction to density-functional approximations for many-electron systems*, Physical Review B **23**, 5048 (1981).

[128] N. Troullier and J. L. Martins, *Efficient pseudopotentials for plane-wave calculations*, Physical Review B **43**, 1993 (1991).

[129] S. Berber, Y.-K. Kwon, and D. Tománek, *Bonding and Energy Dissipation in a Nanohook Assembly*, Physical Review Letters **91**, 165503 (2003).

[130] G. Overney, W. Zhong, and D. Tománek, *Structural rigidity and low frequency vibrational modes of long carbon tubules*, Z. Phys. D **27**, 93 (1993).

[131] M. Treacy, T. Ebbesen, and J. Gibson, *Exceptionally high Young's modulus observed for individual carbon nanotubes*, Nature **381**, 678 (1996).

[132] M. R. Falvo, G. J. Clary, R. M. T. II, V. Chi, F. P. B. Jr, S. Washburn, and R. Superfine, *Bending and buckling of carbon nanotubes under large strain*, Nature **389**, 582 (1997).

[133] B. I. Yakobson, C. Brabec, and J. Bernholc, *Nanomechanics of Carbon Tubes: Instabilities beyond Linear Response*, Physical Review Letters **76**, 2511 (1996).

[134] J. P. Lu, *Elastic properties of carbon nanotubes and nanoropes*, Physical Review Letters **79**, 1297 (1997).

[135] W. N. Reynolds, *Physical Poperties of Graphite*, Elsevier, Amsterdam, 1968.

[136] R. Saito, G. Dresselhaus, and M. S. Dresselhaus, *Tunneling conductance of connected carbon nanotubes*, Physical Review B **53**, 2044 (1996).

[137] S. Iijima, *Carbon Nanotubes*, MRS Bulletin **19**, 43 (1994).

[138] J.-C. Gabriel, (private communication).

[139] B. Dunlap, *Connecting carbon tubules*, Physical Review B **46**, 1933 (1992).

[140] J. C. Charlier, T. W. Ebbesen, and P. Lambin, *Structural and electronic properties of pentagon-heptagon pair defects in carbon nanotubes*, Physical Review B **53**, 11108 (1996).

[141] J. Tersoff, *Empirical interatomic potential for carbon, with applications to amorphous-carbon*, Physical Review Letters **61**, 2879 (1988).

[142] S. Fahy, S. Louie, and M. Cohen, *Pseudopotential total-energy study of the transition from rhombohedral graphite to diamond*, Physical Review B **34**, 1191 (1986).

[143] S. Berber, Y.-K. Kwon, and D. Tománek, *Unusually High Thermal Conductivity of Carbon Nanotubes*, Physical Review Letters **84**, 4613 (2000).

[144] P. Simonis, A. Volodin, E. Seynaeve, P. Lambin, and C. V. Haesendonck, *Comparative study of a coiled carbon nanotube by atomic force misroscopy and scanning electron misroscopy*, in *Science and Application of Nanotubes*, edited by D. Tománek and R. J. Enbody (Kluwer Academic, New York, 2000), p. 83 .

[145] Z. F. Ren, Z. P. Huang, J. W. Xu, J. H. Wang, P. Bush, M. P. Siegal, and P. N. Provencio, *Synthesis of large arrays of well-aligned carbon nanotubes on glass*, Science **282**, 1105 (1999).

[146] S. Berber, E. Osawa, and D. Tománek, *Rigid Crystalline Phases of Polymerized Fullerenes*, Submitted to Physcial Review B (2004).

[147] C. Kittel, *Introduction to Solid State Physics*, Wiley, New York, 1996.

[148] S. J. Woo, E. Kim, S. H. Lee, Y. H. Lee, I. C. Jeon, and S. Y. Hwang, *Bulk modulus of C_{60} molecule via tight-binding method*, Phys. Lett. A **162**, 501 (1992).

[149] N. R. Serebryanaya, V. D. Blank, V. A. Ivdenko, and L. A. Chernozatonskii, *Pressure-induced superhard phase of C_{60}*, Solid State Commun. **118**, 183 (2001).

[150] A. V. Talyzin, L. S. Dubrovinsky, M. Oden, T. L. Bihan, and U. Jansson, *In situ x-ray diffraction study of C_{60} polymerization at high pressure and temperature*, Phys. Rev. B **66**, 165409 (2002).

[151] S. Okada, S. Saito, and A. Oshiyama, *New Metallic Crystalline Carbon: Three Dimensionally Polymerized C_{60} Fulllerite*, Phys. Rev. Lett. **83**, 1986 (1999).

[152] E. Burgos, E. Halac, R. Weht, H. Bonadeo, E. Artacho, and P. Ordejon, *New superhard phases for three-dimensional C-60-based fullerites*, Phys. Rev. Lett. **85**, 2328 (2000).

[153] C. A. Perottoni and J. A. H. da Jornada, *First-principles calculation of the structure and elastic properties of a 3D-polymerized fullerite*, Phys. Rev. B **65**, 224208 (2002).

[154] N. R. Serebryanaya and L. A. Chernozatonskii, *Modelling and interpretation of the experimental data on the 3D polymerized C60 fullerites*, Solid State Commun. **114**, 537 (2000).

[155] L. Chernozatonskii, N. Serebryanaya, and B. Mavrin, *The superhard crystalline three-dimensional polymerized C-60 phase*, Chem. Phys. Lett. **316**, 199 (2000).

[156] S. Okada, S. Saito, and A. Oshiyama, *Comment on "New metallic crystalline carbon: Three dimensionally polymerized C-60 fullerite" - Okada, Saito, and Oshiyama reply*, Phys. Rev. Lett. **85**, 5672 (2000).

[157] A. M. Rao, P. C. Eklund, U. D. Venkateswaran, J. Tucker, M. A. Duncan, G. M. Bendele, P. W. Stephens, J.-L. Hodeau, L. Marques, M. Nunez-Regueiro, I. O. Bashkin, E. G. Ponyatovsky, and A. P. Morovsky, *Properties of C60 polymerized under high pressure and temperature*, Applied Physics A **44**, R6562 (1991).

[158] K. P. Meletov, J. Arvanitidis, S. Assimopoulos, G. A. Kourouklis, and B. Sundqvist, *Pressure-induced transformations and optical properties of the two-dimensional tetragonal polymer of C60 at pressures up to 30 GPa*, J. Exp. Theor. Phys. **95**, 736 (2002).

[159] A. V. Okotrub, V. V. Belavin, L. G. Bulusheva, V. A. Davydov, T. L. Makarova, and D. Tománek, *Electronic structure and properties of rhombohedrally polymerized C60*, J. Chem. Phys. **115**, 5637 (2001).

[160] K. Honda, E. Osawa, Z. Slanina, and T. Matsumoto, *Thermal transformation of ring-opened [2+2]C_{60} dimer into a wide-bridged C_{120} isomer. A computational evaluation of fulvalene-naphthalene rearrangements*, Fullerene Science and Technology **4**, 819 (1996).

[161] S. Osawa, M. Sakai, and E. Osawa, *Nature of Cyclobutane Bonds in the Neutral [2+2] Dimer of C_{60}*, Journal of Physical Chemistry A **101**, 1378 (1997).

[162] H. Ueno, S. Osawa, E. Osawa, and K. Takeuchi, *Stone-Wales rearrangement pathways from the hinge-opened [2+2] C_{60} dimer to IPR C_{120} fullerenes: vibrational analysis of intermediates*, Fullerene Science and Technology **6**, 319 (1998).

[163] Y.-K. Kwon, S. Berber, and D. Tománek, *Thermal Contraction of Carbon Fullerenes and Nanotubes*, Physical Review Letters **92**, 015901 (2004).

[164] H. Mavoori and S. Jin, *Low thermal-expansion copper composites via negative CTE metallic elements*, JOM-Journal of The Minerals Metals & Materials Society **50**, 70 (1998).

[165] X. C. Li, J. Stampfl, and F. B. Prinz, *Mechanical and Thermal Expansion Behavior of Laser Deposited Metal Matrix Composites of Invar and TiC*, Materials Science and Engineering A **282**, 86 (2000).

[166] T. Ito, T. Suganuma, and K. Wakashima, *A micromechanics-based analysis for tailoring glass-fiber-reinforced thermoplastic laminates with near-zero coefficients of thermal expansion*, Composites Science and Technology **60**, 1851 (2000).

[167] R. Kubo, *Rubber Elasticity*, Kawade Shobo Shinsha, Tokyo, 1946.

[168] D. Lacks and G. Rutledge, *Mechanisms for axial thermal contraction in polymer crystals - Polyethylene vs isotactic Polypropylene*, Chemical Engineering Science **49**, 2881 (1994).

[169] P. Papanek and J. Fischer, *Molecular-Dynamics simulation of crystalline Trans-polyacetylene*, Physical Review B **48**, 12566 (1993).

[170] R. Baughman and E. Turi, *Negative thermal-expansion of a Polydiacetylene single-crystal*, Journal of Poylmer Science Part B-Polymer Physics **11**, 2453 (1973).

[171] R. Munn, *Role of elastic-constants in negative thermal-expansion of axial solids*, Journal of Physics C: Solid State Physics **5**, 535 (1972).

[172] D. Riley, *The thermal expansion of graphite: Part II theoretical*, Proceedings of The Physical Society of London **57**, 486 (1945).

[173] W. Morgan, *Thermal-Expansion coefficients of graphite crystals*, Carbon **10**, 73 (1972).

[174] G. Belenkii, E. Salaev, R. Suleimanov, N. Abdullaev, and V. Shteinshraiber, *The nature of negative linear expansion in layer crystals C, BN, GaS, GaSe AND InSe*, Solid State Communications **53**, 967 (1985).

[175] R. Roy and D. Agrawal, *Thermal-expansion materials not so new*, Nature **388**, 433 (1997).

[176] T. Mary, J. Evans, T. Vogt, , and A. Sleight, *Negative thermal expansion from 0.3 to 1050 Kelvin in* ZrW_2O_8, Science **272**, 90 (1996).

[177] G. Tseng and J. Ellenbogen, *Nanotechnology - Toward nanocomputers*, Science **294**, 1293 (2001).

[178] E. Minot, Y. Yaish, V. Sazonova, J.-Y. Park, M. Brink, and P. McEuen, *Tuning Carbon Nanotube Band Gaps with Strain*, Physical Review Letters **90**, 156401 (2003).

[179] M. Cadek, J. Coleman, V. Barron, K. Hedicke, and W. Blau, *Morphological and mechanical properties of carbon-nanotube-reinforced semicrystalline and amorphous polymer composites*, Applied Physics Letters **81**, 5123 (2002).

[180] A. Thess, R. Lee, P. Nikolaev, H. Dai, P. Petit, J. Robert, C. Xu, Y. Lee, S. Kim, D. Colbert, G. Scuseria, D. Tománek, J. Fischer, and R. Smalley, *Crystalline ropes of metallic carbon nanotubes*, Science **273**, 483 (1996).

[181] R. H. Baughman and A. Soldatov, (private communication).

[182] Y.-K. Kwon and D. Tománek, *Orientational melting in carbon nanotube ropes*, Physical Review Letters **84**, 1483 (2000).

[183] Y. Maniwa, R. Fujiwara, H. Kira, H. Tou, H. Kataura, S. Suzuki, Y. Achiba, E. Nishibori, M. Takata, M. Sakata, A. Fujiwara, , and H. Suematsu, *Thermal expansion of single-walled carbon nanotube (SWNT) bundles: X-ray diffraction studies*, Physical Review B **64**, 241402 (2001).

[184] N. Raravikar, P. Keblinski, A. Rao, M. Dresselhaus, L. Schadler, and P. Ajayan, *Temperature dependence of radial breathing mode Raman frequency of single-walled carbon nanotubes*, Physical Review B **66**, 235424 (2002).

[185] L. Wei, P. Kuo, R. Thomas, T. Anthony, and W. Banholzer, *Thermal conductivity of isotopically modified single crystal diamond*, Physical Review Letters **70**, 3764 (1993).

[186] J. Hone, M. Whitney, C. Piskoti, and A. Zettl, *Thermal conductivity of single-walled carbon nanotubes*, Physical Review B **59**, R2514 (1999).

[187] J. Hone, M. Whitney, and A. Zettl, *Thermal conductivity of single-walled carbon nanotubes*, Synthetic Metals **103**, 2498 (1999).

[188] C. Uher, *Thermal conductivity of graphite*, in *Landolt-Börnstein: Numerical Data and Functional Relationships in Science and Technology*, edited by O. Madelung and G.K. White, New Series, Group III, Vol. 15c (Springer-Verlag, Berlin, 1991), pp. 426–448 .

[189] P. Jund and R. Jullien, *Molecular-dynamics calculation of the thermal conductivity of vitreous silica*, Physical Review B **59**, 13707 (1999).

[190] M. Schoen and C. Hoheisel, *The shear viscosity of a Lennard-Jones fluid calculated by equlibrium molecular dynamics*, Molecular Physics **56**, 653 (1985).

[191] D. Levesque and L. Verlet, *Molecular-Dynamics calculations of transport-coeffiecients*, Molecular Physics **61**, 143 (1987).

[192] D. McQuarrie, *Statistical Mechanics*, Harper and Row, London, 1976.

[193] A. Maeda and T. Munakata, *Thermal Conductivity of 1D lattice by NEMD*, Physical Review E **52**, 234 (1995).

[194] D. Evans, *Homogeneous NEMD algorithm for thermal-conductivity - Application of non-canonical linear response theory*, Physics Letters A **91**, 457 (1982).

[195] D. Hansen and D. Evans, *A generalized heat-flow algorithm*, Molecular Physics **81**, 767 (1994).

[196] D. Rapaport, *The Art of Molecular Dynamics Simulation*, Cambridge University Press, Cambridge, 1998.

[197] T. Anthony, W. Banholzer, J.F.Fleischer, L. Wei, P. Kuo, R. Thomas, and R. Pryor, *Thermal diffusivity of isotopically enriched ^{12}C diamond*, Physical Review B **42**, 1104 (1990).

[198] T. Nihira and T. Iwata, *Thermal resistivity changes in electron-irradiated pyrolytic-graphite*, Japanese Journal of Applied Physics **14**, 1099 (1975).

[199] M. Holland, C. Klein, and W. Straub, *The lorenz number of graphite at very low temperatures*, Journal of Physics and Chemistry of Solids **27**, 903 (1966).

[200] A. de Combarieu, *Conductibilité Thermique de Graphite Quais Monocristallin et Effets D'irradiation Aux Neutrons I. Mesures*, Journal de Physique (Paris) **28**, 951 (1967).

[201] N. Park, M. Yoon, S. Berber, J. Ihm, E. Osawa, and D. Tománek, *Magnetism in all-carbon structures with negative Gaussian Curvature*, Physical Review Letters **91**, 237204 (2003).

[202] T. L. Makarova, B. Sundqvist, R. Höhne, P. Esquinazi, Y. Kopelevich, P. Scharff, V. A. Davydov, L. S. Kashevarova, and A. V. Rakhmanina, *Magnetic carbon*, Nature **413**, 716 (2001).

[203] A. Rode, (private communication).

[204] A. L. Mackay and H. Terrones, *Diamond from graphite*, Nature **352**, 762 (1991).

[205] D. Vanderbilt and J. Tersoff, *Negative-curvature fullerene analog of C60*, Physical Review Letters **68**, 511 (1992).

[206] L. A. Bursill and L. Bourgeois, *Image-analysis of a negatively curved graphitic sheet model for amorphous-carbon*, Physics Letters B **9**, 1461 (1995).

[207] S. T. Hyde and M. O'Keeffe, *Elastic warping of graphitic carbon sheets: Relative energies of some fullerenes, schwarzites and buckytubes*, Phil. Trans. Roy. Soc. Lond. A **354**, 1999 (1996).

[208] A. V. Rode, S. T. Hyde, E. G. Gamaly, R. G. Elliman, D. R. McKenzie, and S. Bulcock, *Structural analysis of a carbon foam formed by high pulse-rate laser ablation*, Applied Physics A-Materials Science & Processing **69**, S755 (1999).

[209] A. V. Rode, E. G. Gamaly, and B. Luther-Davies, *Formation of cluster-assembled carbon nano-foam by high-repetition-rate laser ablation*, Applied Physics A-Materials Science & Processing **70**, 135 (2000).

[210] M. Fujita, K. Wakabayashi, K. Nakada, and K. Kusakabe, *Peculiar localized state at zigzag graphite edge*, Journal of The Physical Society of Japan **65**, 1920 (1996).

[211] K. Wakabayashi, M. Sigrist, and M. Fujita, *Spin wave mode of edge-localized magnetic states in nanographite zigzag ribbons*, Journal of The Physical Society of Japan **67**, 2089 (1998).

[212] K. Nakada, M. Fujita, G. Dresselhaus, and M. S. Dresselhaus, *Edge state in graphene ribbons: Nanometer size effect and edge shape dependence*, Physical Review B **54**, 17954 (1996).

[213] K. Kusakabe and M. Maruyama, *Magnetic nanographite*, Physical Review B **67**, 092406 (2003).

[214] L. Kleinman and D. M. Bylander, *Efficacious form for model pseudopotentials*, Physical Review Letters **48**, 1425 (1982).

[215] O. F. Sankey and D. J. Niklewski, *Ab initio multicenter tight-binding model for molecular-dynamics simulations and other applications in covalent system*, Physical Review B **40**, 3979 (1989).

[216] N. Park, K. Lee, S. Han, J. Yu, and J. Ihm, *Energetics of large carbon clusters:Crossover from fullerenes to nanotube*, Physical Review B **65**, 121405 (2002).

[217] M. Scheffler, J. P. Vigneron, and G. B. Bachelet, *Energetics of large carbon clusters: Crossover from fullerenes to nanotubes*, Physical Review B **31**, 6541 (1985).

[218] A. T. Balaban, D. J. Klein, and C. A. Folden, *Diamond-graphite hybrids*, Chemical Physics Letters **217**, 266 (1994).

[219] J. Choi, Y.-H. Kim, K. J. Chang, and D. Tománek, *Itinerant ferromagnetism in heterostructured C/BN nanotubes*, Physical Review B **67**, 125421 (2003).

[220] M. Gomberg, *An Instance of trivalent carbon: Triphenylmethyl*, Journal of American Chemical Society **22**, 757 (1900).

[221] R. C. Haddon, *Design of Organic Metals and Superconductors*, Nature (London) **256**, 394 (1975).

[222] M. E. Itkis, X. Chi, A. W. Cordes, and R. C. Haddon, *Magneto-Opto-Electronic Bistability in a Phenalenyl-Based Neutral Radical*, Science **296**, 1443 (2002).